Dynamics of streamer-to-leader transition at reduced air densities and its implications for propagation of lightning leaders and gigantic jets

Caitano L. da Silva[1] and Victor P. Pasko[1]

[1]   In this paper we present modeling studies of air heating by electrical discharges in a wide range of pressures. The developed model is capable of quantifying the different contributions for heating of air at the particle level and rigorously accounts for the vibration-dissociation-vibration coupling. The model is validated by calculating the breakdown times of short air gaps and comparing to available experimental data. Detailed discussion on the role of electron detachment in the development of the thermal-ionizational instability that triggers the spark development in short air gaps is presented. The dynamics of fast heating by quenching of excited electronic states is discussed and the scaling of its main channels with ambient air density is quantified. The developed model is employed to study the streamer-to-leader transition process and to obtain its scaling with ambient air density. Streamer-to-leader transition is the name given to a sequence of events occurring in a thin plasma channel through which a relatively strong current is forced through, culminating in heating of ambient gas and increase of the electrical conductivity of the channel. This process occurs during the inception of leaders (from sharp metallic structures, from hydrometeors inside the thundercloud, or in virgin air) and during their propagation (at the leader head or during the growth of a space leader). The development of a thermal-ionizational instability that culminates in the leader formation and propagation is characterized by a change in air ionization mechanism from electron impact to associative ionization and by contraction of the plasma channel. The introduced methodology for estimation of leader speeds shows that the propagation of a leader is limited by the air heating of every newly formed leader section. It is demonstrated that the streamer-to-leader transition time has an inverse-squared dependence on the ambient air density at near-ground pressures, in agreement with similarity laws for Joule heating in a streamer channel. Model results indicate that a deviation from this similarity scaling occurs at very low air densities, where the rate of electronic power deposition is balanced by the channel expansion, and air heating from quenching of excited electronic states is very inefficient. These findings place a limit on the maximum altitude at which a hot and highly conducting lightning leader channel can be formed in the Earth's atmosphere, result which is important for understating of the gigantic jet (GJ) discharges between thundercloud tops and the lower ionosphere. Simulations of leader speeds at GJ altitudes demonstrate that initial speeds of GJs are consistent with the leader propagation mechanism. The simulation of a GJ, escaping upward from a thundercloud top, shows that the lengthening of the leader streamer zone, in a medium of exponentially decreasing air density, determines the existence of an altitude at which the streamer zones of GJs become so long that they dynamically extend (jump) all the way to the ionosphere.

[1]CSSL Laboratory, Pennsylvania State University, University Park, Pennsylvania, USA.

Corresponding author: C. L. da Silva, Communications and Space Sciences Laboratory, Department of Electrical Engineering, Pennsylvania State University, 227 EE East, University Park, PA 16802-2706, USA. (caitano.dasilva@psu.edu)

1. Introduction

[2]   This work is dedicated to study the physical processes leading to the formation of a leader discharge [e.g., *Bazelyan and Raizer*, 1998, Chapter 6]. Leaders are a fundamental component in the breakdown of long air gaps in laboratory discharges [e.g., *Gallimberti et al.*, 2002]. They are present in natural and artificial (i.e., triggered) lightning [e.g., *Rakov and Uman*, 2003, Chapters 4–9] and are believed to play
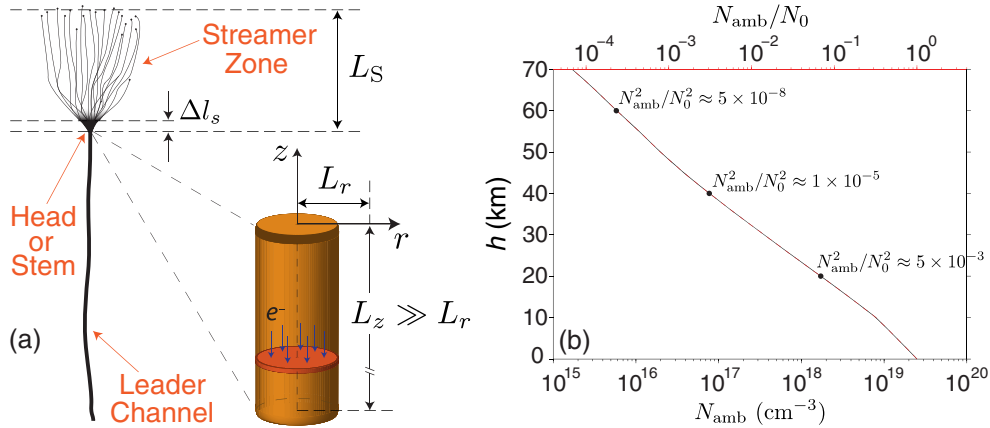
Figure 1. (a) Sketch of a positive leader highlighting the simulated region. (b) Exponential decrease of ambient air density with altitude in the Earth's atmosphere. Bottom axis presents N_{amb} in cm^{-3}, while top axis presents N_{amb}/N_0, where $N_0 = 2.5 \times 10^{19}$ cm^{-3} is the ambient air density at ground level.

a key role in the recently discovered subset of transient luminous events emanating from thundercloud tops, commonly referred as "Jets" [e.g., *Wescott et al.*, 1995, 1996; *Pasko et al.*, 2002; *Su et al.*, 2003; *Lee et al.*, 2012].

[3] Streamer-to-leader transition is the name given to a sequence of processes leading to the conversion of a cold (room temperature) streamer corona discharge to a hot leader channel. The streamer-to-leader transition dictates the onset and propagation of leader discharges. In literature, the physical processes leading to the leader onset were theoretically studied in the context of laboratory discharges [e.g., *Gallimberti*, 1979; *Bondiou and Gallimberti*, 1994; *Aleksandrov et al.*, 2001a; *Vidal et al.*, 2002; *Popov*, 2003, 2009; *Bazelyan et al.*, 2007a], where experimental data are available. Similarly, in the context of lightning discharges, numerical models were employed to simulate the inception and propagation of upward lightning leaders from rocket-triggered lightning and tall structures [e.g., *Aleksandrov et al.*, 2001b; *Lalande et al.*, 2002; *Becerra and Cooray*, 2006; *Becerra et al.*, 2007; *Bazelyan et al.*, 2007b, 2008], where ambient conditions can be somewhat inferred.

[4] The main goal of the present work is to characterize the discharge mechanisms involved in the development of upward jets from thundercloud tops. This investigation is of special importance in the context of Gigantic Jets (GJs) [*Pasko et al.*, 2002; *Su et al.*, 2003], which are large-scale electrical discharges that are observed to emanate from thundercloud tops (at ∼20 km altitude) and propagate up to the lower ionosphere (at ∼90 km) [*Pasko et al.*, 2002; *Su et al.*, 2003; *van der Velde et al.*, 2007, 2010; *Chen et al.*, 2008; *Kuo et al.*, 2009; *Cummer et al.*, 2009; *Chou et al.*, 2010, 2011; *Soula et al.*, 2011; *Lu et al.*, 2011]. The current theoretical understanding of the GJ process describes it as an upward directed discharge, analogous to cloud-to-ground lightning [*Krehbiel et al.*, 2008]. In a normal-polarity thunderstorm (i.e., containing a midlevel negative and an upper positive charge centers), GJs are initiated between adjacent charge regions (similarly to intracloud lightning discharges), where the electric field is the highest [*Krehbiel et al.*, 2008]. Lightning is initiated as a bidirectional discharge [*Kasemir*, 1960] that propagates in the form of positive leaders in

the negative charge region and in the form of negative leaders in the positive charge region [e.g., *Mazur*, 2002; *Riousset et al.*, 2007]. *Krehbiel et al.* [2008] demonstrated that when the two charges were not balanced (meaning the upper positive charge center contains less net charge than the midlevel negative charge center), the leader potential could be significantly shifted in the direction defined by the charge with dominant magnitude. In this situation the propagation of the leader becomes essentially independent from the weaker charge center, allowing it to penetrate through the weaker upper charge center and to escape from the thundercloud upward and serve as the initiation of a GJ [*Krehbiel et al.*, 2008; *Riousset et al.*, 2010a]. Thus, understanding of the GJ process and of its interaction with stratosphere, mesosphere, and lower ionosphere requires quantitative characterization of the streamer-to-leader transition process and the physics of lightning leaders at reduced air densities.

1.1. Phenomenology of Positive and Negative Leaders

[5] Leaders are self-propagating discharges, capable of travel kilometer long distances at ground and near-ground pressure. They are the mechanism present in lightning discharges, enabling a cloud-to-ground lightning to form a highly conducting path that "short-circuits the gap" between a thundercloud and the ground, neutralizing (or reducing) the potential difference between cloud and ground. Extensive literature review on the several lightning manifestations is provided by *Rakov and Uman* [2003]. A leader is a complex structure; nevertheless, its description can be made simpler by recognizing the existence of three different regions: (1) the streamer zone, (2) the leader head or stem, and (3) the channel [*Bazelyan and Raizer*, 1998, Section 6.1.1]. The three distinct regions are depicted in Figure 1a for a positive leader (see also Figure 6 by *Bondiou and Gallimberti* [1994]). The streamer zone is composed by a fan of thousands of streamers; the ionization process associated with the formation and propagation of each single streamer is the source of electrical current for heating of the leader channel. The second region is called in literature leader head [e.g., *Bazelyan and Raizer*, 1998]

or leader stem [e.g., *Gallimberti et al.*, 2002]. Regardless of name, this segment is where the transition between cold streamers to a hot channel takes places. The leader head is the common origin point for all streamers in the streamer zone, which individually carry very low current. It is due to the addition of their currents at this point that heating of air is made possible. The leader channel is a hot plasma filament at temperatures of 5000–7000 K in laboratory leaders and even higher in lightning [*Aleksandrov et al.*, 2001a]. This channel is highly conducting and it is capable of transmitting the electrode's potential to the leader head. This is of fundamental importance because an ionizing field ahead of the leader is required for the inception of streamer coronas, in the streamer zone region, to promote the leader propagation. The three parts described above can be clearly optically distinguished in streak photograph of laboratory leaders [e.g., *Bazelyan and Raizer*, 1998, Figure 6.1]. A fourth additional structure that cannot be seen is the leader cover. As the leader propagates, it enters a region containing the space charge previously formed in the streamer zone, which was left behind. This charge region is accumulated around the channel and has the role of stabilizing the channel by reducing the radial electric field component, preventing its ionization expansion [*Bazelyan and Raizer*, 2000, p. 67].

[6] Positive leaders advance in space by creating a heating conversion zone in their tips, i.e., the transition between cold streamers to a hot leader channel occurs in the leader head, as schematically represented in Figure 1a. Negative leaders, on the other hand, present a more complex dynamics and are characterized by a stepped propagation. Within the streamer zone region, a plasma inhomogeneity (referred to as a plasmoid by *Petrov and Petrova* [1999]) grows to form a space stem. The electric field configuration around the space stem is capable of producing two sets of streamer coronas, one in each opposite direction [*Gorin et al.*, 1976]. The negative corona is formed in the direction of the main leader propagation, while the positive corona is launched backward (see schematics by *Petersen et al.* [2008, Figure 7], for example). The current produced by the streamer coronas may be sufficient to promote Joule heating in the space stem, turning it into a space leader [e.g., *Gallimberti et al.*, 2002, Figure 4]. The positive extremity of the space leader connects to the main leader and the system experiences a miniaturized return stroke-like process, which is characterized by a transient increase in the radiation intensity. The negative space leader extremity becomes the new leader head and the process is repeated [*Bazelyan and Raizer*, 1998, p. 255]. The formation of a space leader ahead of the negative leader is a fundamental stage in the leader progression, as evidenced in laboratory [e.g., *Ortega et al.*, 1994; *Reess et al.*, 1995; *Bazelyan and Raizer*, 1998; *Gallimberti et al.*, 2002] and lightning [e.g., *Biagi et al.*, 2009, 2010; *Hill et al.*, 2011] observations. Although positive and negative leaders exhibit different dynamical features, it can be seen, from the above discussion, that the streamer-to-leader transition (or in other words, the air heating) is a fundamental process that defines leader propagation in both cases. For positive leaders, it occurs in the leader head, attached to the main channel, while for negative leader this process occurs during the growth of the space leader ahead of the main leader channel. Detailed discussion on the phenomenology of leader discharges is provided by *Bazelyan and Raizer* [1998, Chapter 6].

1.2. Brief History of Air Heating Modeling in the Context of Electrical Discharges

[7] Throughout the years, an extensive amount of theoretical work has been done to understand the role of air heating by a discharge current as a fundamental stage for electrical breakdown. Most of contemporary efforts to model the leader onset and propagation are built on early work by *Gallimberti* [1979]. As pointed out by *Marode* [1983], still in the early stages of this research topic, models presented in literature follow two different approaches. The channel-controlled approach assumes a constant electric field in the gap and it is employed to describe streamer-to-spark transition after the streamer bridges a short gap [e.g., *Marode et al.*, 1979; *Bastien and Marode*, 1985; *Aleksandrov et al.*, 1998; *Naidis*, 1999, 2005; *Riousset et al.*, 2010b]. The head-controlled approach postulates either a time-dependent or a stationary current, and it is employed to study the streamer-to-leader transition occurring in the leader inception and in leader heads propagating through long air gaps [e.g., *Gallimberti*, 1979; *Aleksandrov et al.*, 2001a; *Gallimberti et al.*, 2002; *Bazelyan et al.*, 2007a; *Popov*, 2003, 2009]. Some key contributions, from the above listed modeling works, are reviewed below.

[8] Studies on spark formation have started with the identification of the thermal mechanism as being a fundamental stage in the gap breakdown [*Marode*, 1983, and references therein]. The thermal mechanism leads to lowering of the gas number density N inside the channel due to the expansion of the heated gas [*Marode et al.*, 1979; *Marode*, 1983; *Bastien and Marode*, 1985]. This process leads to the growth of the mean reduced field E/N and, therefore, to an increase in the air ionization rate (electron-impact ionization of N_2 and O_2 molecules). Later, the importance of kinetic effects in electrical discharges started to be discussed [e.g., *Mnatsakanyan and Naidis*, 1991; *Kossyi et al.*, 1992]. *Aleksandrov et al.* [1997] pointed out the importance of (stepwise) ionization of O atoms and NO molecules for the transition and that associative ionization between N and O atoms is the most important mechanism for plasma maintenance at temperatures higher than 4500 K. In a subsequent work, *Aleksandrov et al.* [1998] developed a model accounting for the fact that the Joule heating, owing to the current flow in the channel, is not solely used to increase the temperature of the background gas. Instead, only a small fraction of the deposited electronic power is used to heat the channel in the so-called "fast heating" process, mainly associated with collisional quenching of electronically excited states of N_2 and O_2 molecules; a significant fraction of the electronic energy is transferred to and stored in the vibrational energy levels of the N_2 molecules. *Naidis* [1999] studied the spark formation in nanosecond time range and showed that accumulation of active particles (mainly O atoms) accelerate the rate of electron detachment contributing to streamer-to-spark transition. In a subsequent work, *Naidis* [2005] demonstrated the existence of two distinct regimes in the spark formation (at ambient ground pressure): the first one, occurring at times shorter than 1 μs, is dominated by the kinetic effects, while the second one, occurring at times longer than 1 μs, is dominated by the thermal mechanism. *Popov* [2001, 2011] and *Flitti and Pancheshnyi* [2009] presented calculations of the electron energy partition and they have demonstrated that the fraction

of electronic power spent on excitation of electronic molecular states that is converted into gas heating is approximately independent of electric field (and is around $\sim30\%$), in agreement with previous assumptions by *Aleksandrov et al.* [1998]. *Popov* [2003] employed a fully one-dimensional model to simulate the streamer-to-leader transition occurring in the head of a positive leader with an electrical current of ~1 A. He discussed the effects of the current contraction and the role of associative ionization processes involving $N_2(A^3\Sigma_u^+)$ and $N_2(a'\,^1\Sigma_u^-)$ excited species. Later, *Popov* [2009] applied his previously developed model [*Popov*, 2001, 2003] to estimate leader speeds, following the approach of *Bazelyan and Raizer* [2000, p. 67] and *Bazelyan et al.* [2007a]. More recently, following the approach of *Naidis* [1999, 2005], *Riousset et al.* [2010b] developed a streamer-to-spark transition model capable of reproducing experimental data of *Černák et al.* [1995] and *Larsson* [1998]. They studied the scaling of the breakdown time with ambient air density, or pressure, in a range corresponding to 0–70 km altitude in the Earth's atmosphere. Between ground and 70 km altitude, the ambient air density N_{amb} varies by approximately 4 orders of magnitude, as shown in Figure 1b. *Riousset et al.* [2010b] have demonstrated that under assumptions of a constant electric field across the gap, the breakdown time scales with air density close to $1/N_{amb}$. This scaling leads to shorter breakdown time than that predicted by similarity laws for Joule heating [e.g., *Pasko*, 2006, p. 267], which is $1/N_{amb}^2$. They have attributed this acceleration to a strong reduction in electron losses due to three-body attachment and electron-ion recombination processes with reduction of air pressure [*Riousset et al.*, 2010b].

1.3. Purpose of This Paper

[9] The main goal of this paper is to study the scaling of the streamer-to-leader transition process with ambient air density. For this purpose, we introduce a model to describe the air heating produced by the electrical current injected in the leader head (Sections 2.1–2.4). We present a simple model for the fast heating of air due to quenching of excited electronic states (Section 2.3), and we discuss its scaling with ambient air density (Section 3.2). We examine the plasma instability driven by constant electric field, such as studied by *Riousset et al.* [2010b], pointing out the role of electron detachment in the breakdown of short air gaps (Section 3.1). We discuss the peculiarities of the plasma instability driven by constant current, culminating in streamer-to-leader transition (Section 4.1) and its scaling with ambient air density (Section 4.2). We demonstrate that leader speed can be more generally written as a function of the initial current density in the leader stem, instead of total current (Section 5.1). Finally, we explore the implications of the scaling of the streamer-to-transition time with air density for the upward propagation of gigantic jet leaders (Section 5.2).

2. Model Formulation

[10] We present a model for streamer-to-leader transition built on three principal assumptions: (1) the axial variations along the channel are negligible in comparison to the radial ones and, therefore, the leader head can be represented by a one-dimensional (1-D) radial system, (2) the electrical current of a propagating leader is produced in the streamer zone and injected in the leader head and, therefore, it is an external parameter for this region, and (3) the streamer-to-leader transition takes place in a time scale τ_h on which a newly formed portion of the leader is heated to a temperature of ~2000 K. Figure 1a presents the schematics of a positive leader, highlighting the simulated region. The physical interpretation of the simulation region is straightforward in the case of a positive leader. In the case of negative leaders, an analogous process can be assumed to take place in the space stem, during the growth of a space leader, ahead of the main leader channel, as mentioned in Section 1.2. The proposed methodology is based on previous theoretical works reviewed in Section 1.2 [e.g., *Naidis*, 1999, 2005; *Popov*, 2003, 2009; *Riousset et al.*, 2010b]. The approximation that the leader head can be treated as a 1-D system (2-D with axial symmetry) is made necessary due to the extensive list of physical/chemical processes, with largely different time scales, involved in the nonequilibrium plasma described here.

[11] The initial conditions for the leader stem describe a solitary plasma channel embedded in a nonperturbed atmosphere consisting of 79% of N_2 and 21% of O_2 at ambient temperature $T_0 = 300$ K. Initially, the plasma channel is set to have a Gaussian radial distribution $n_e(r) = n_{e,a}\exp(-r^2/r_c^2)$, with a peak value of $n_{e,a} = 2\times10^{14}$ cm^{-3} and a $1/e$ radius $r_c = 0.3$ mm, at ground pressure. Charge neutrality is ensured by setting the initial density of O_2^+ ions to be equal to the electronic one and densities of all other ion species to zero [*Popov*, 2003, 2009]. The initial conditions for simulations at different altitudes are obtained by scaling the ground parameters with air density using similarity laws for streamer discharges [*Pasko*, 2006, pp. 265–267]. For example, the initial radius and electron density are written as $r_c = r_{c,0}N_0/N_{amb}$ and $n_e = n_{e,0}N_{amb}^2/N_0^2$, respectively, where N_{amb} is the ambient air density at an altitude of interest and N_0 is the ambient air density at ground level. Figure 1b shows the exponential decrease of N_{amb} with altitude h. Note that N_{amb} represents only the initial conditions for the simulations, i.e., $N(t=0) = N_{amb}$. An important characteristic of the model described below is that it allows for actual value of N to reduce due to gas expansion and to increase due to dissociation. Hence, in this article, we refer to N_{amb} when discussing scaling of properties with altitude in Earth's atmosphere and to N when discussing the effects of dynamic lowering of neutral density in the reduced electric field E/N during the leader formation process. To summarize, quantities with subindex "amb" refer to the ambient values, quantities with subindex "0" refer to ambient values at ground pressure, and quantities with neither "amb" nor "0" subindex refer to actual dynamic values of the variables.

[12] The above described initial conditions are chosen such that the leader stem resembles a single streamer channel at the beginning of the simulation [see, e.g., *Liu and Pasko*, 2004]. These initial conditions are used through the whole paper, unless otherwise indicated, as for example in Section 5.1 where the effects of r_c are discussed. The leader stem is then dynamically followed assuming a given current I, and evolution of all parameters is tracked as a function of time t and radial position r. The current I flowing through the leader head is created by the collective action of all the streamers in the streamer zone, as schematically
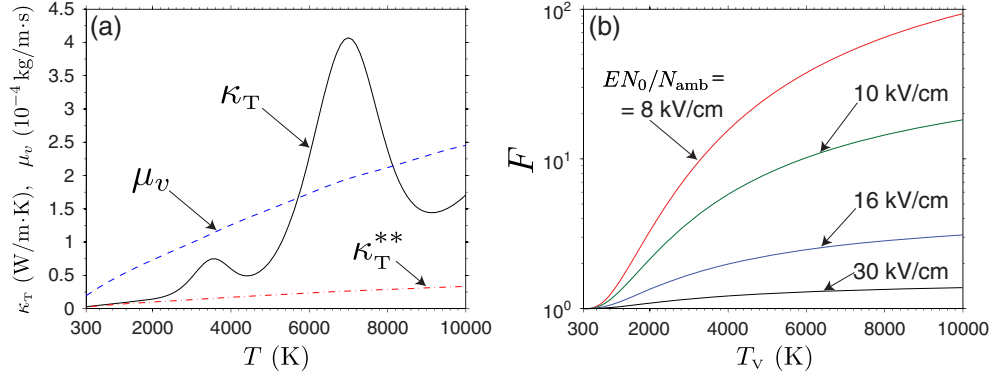
Figure 2. (a) Dependence of viscosity μ_v and heat conduction κ_T coefficients on translational temperature T [*Boulos et al.*, 1994, pp. 413–417]. (b) Dependence of the correction factor F that accounts for electron energy gained in super elastic collisions with vibrationally excited $N_2(v)$, on vibrational temperature T_V [*Benilov and Naidis*, 2003, equation (8)]. Figure 2a also shows a simplified description for the heat conduction coefficient κ_T^{**} described in the text.

represented in Figure 1. The set of physical/chemical processes required to describe the conversion of this cold streamer to a hot leader channel can be divided into four groups: neutral gas dynamics (Section 2.1), a comprising set of chemical reactions (Section 2.2 and Appendix A), energy exchange between charged and neutral particles (Section 2.3), and delayed relaxation of vibrational energy (Section 2.4), as described below.

2.1. Gas Dynamics

[13] The first block of the model contains a set of gas dynamics equations to describe the air heating and expansion due to the passage of the electrical current through the stem's cross section, as follows:

$$\frac{\partial \rho}{\partial t} + \vec{\nabla}\cdot(\rho\vec{v}) = 0 \tag{1}$$

$$\frac{\partial \rho\vec{v}}{\partial t} + \vec{\nabla}\cdot(\rho\vec{v}\vec{v}) = -\vec{\nabla}p + \frac{1}{3}\mu_v\vec{\nabla}(\vec{\nabla}\cdot\vec{v}) + \mu_v\nabla^2\vec{v} \tag{2}$$

$$\frac{\partial \varepsilon}{\partial t} + \vec{\nabla}\cdot[(\varepsilon+p)\vec{v}] = Q_T^{\text{eff}} + \vec{\nabla}\cdot(\kappa_T^*\vec{\nabla}T) \tag{3}$$

$$\frac{\partial \varepsilon_V}{\partial t} + \vec{\nabla}\cdot(\varepsilon_V\vec{v}) = Q_V^{\text{eff}} + \vec{\nabla}\cdot(D_V\vec{\nabla}\varepsilon_V). \tag{4}$$

[14] The equation (1) accounts for mass transport, where the mass density is defined as the sum over all neutral species $\rho = \sum_j m_j n_j$ (where n_j and m_j are the number density and mass of the jth neutral specie described in Section 2.2) and $\vec{v}$ is the bulk velocity of the neutral gas. The equation (2) describes the transport of momentum, with $\rho\vec{v}$ accounting for the momentum per unit volume of the neutral gas. The forcing term is the pressure (p) gradient. Dissipation due to viscous forces [e.g., *Sparrow and Raspet*, 1991, equation (2)] is also accounted for in equation (2), with μ_v being the viscosity coefficient in units of kg/m·s or Pa·s [*Boulos et al.*, 1994, pp. 413–417]. Figure 2a shows the dependence of μ_v on temperature. Equations (3) and (4) describe the energy transport, where ε and ε_V are the translational and vibrational energy densities (expressed in units of J/m^3), respectively, and T and T_V the associated temperatures. The energies are related to the temperatures as

$$\varepsilon = \frac{5}{2}Nk_BT + \frac{1}{2}\rho\,\vec{v}\cdot\vec{v} \tag{5}$$

and

$$\varepsilon_V = \frac{n_{N_2}\hbar\omega}{\exp(\hbar\omega/k_BT_V)-1}, \tag{6}$$

where $\hbar\omega = 0.29$ eV is the vibrational quantum of the N_2 molecule [e.g., *Naidis*, 2005, 2007], n_{N_2} is the N_2 number density, and k_B is the Boltzmann constant. Note that ε describes the overall translational energy of the neutral gas, while ε_V the vibrational energy of solely N_2 molecules. Describing the spatiotemporal evolution of the mean energy distribution by a set of two equations is necessary because, while the equilibrium between translational and rotational degrees of freedom can be assumed to be instantaneously reached, the relaxation of vibrational energy of N_2 molecules occurs on a significantly longer time scale τ_{VT} (defined in Section 2.4) that can be comparable to (or longer than) the channel heating time itself [e.g., *Naidis*, 1999; *Benilov and Naidis*, 2003]. The vibrational temperatures of other diatomic molecules are close to the translational temperature T [*Benilov and Naidis*, 2003]. Equation (3) accounts for heat conduction, where κ_T^* (expressed in units of W/m·K) is the thermal conductivity without the contribution of vibrationally excited nitrogen molecules [*Naidis*, 2007, equation (11)]:

$$\kappa_T^* = \kappa_T - n_{N_2}D_Vk_B\left(\frac{\hbar\omega}{k_BT}\right)^2\frac{\exp(\hbar\omega/k_BT)}{[\exp(\hbar\omega/k_BT)-1]^2} \tag{7}$$

where κ_T is the total thermal conductivity in equilibrium conditions ($T = T_V$) [*Boulos et al.*, 1994, pp. 413–417]. Figure 2a shows the dependence of κ_T on temperature. This correction is made necessary because equation (4) already accounts for energy loss due to diffusion of vibrationally excited nitrogen molecules. The diffusion coefficient is given by $D_V = 1.7\times10^{-5}(T/T_0)^{1.5}N_0/N$ m^2/s [e.g., *Shneider et al.*, 2012], where $T_0 = 300$ K is the ambient value of temperature, N is the neutral gas density defined as the sum over all neutral species $N = \sum_j n_j$, and $N_0 = 2.5\times10^{19}$ cm^{-3} is its ambient value at ground pressure (see Figure 1b). The equation of state $p = Nk_BT$ closes the system of equations (1)–(4). The terms Q_T^{eff} and Q_V^{eff} are the effective rate of energy deposition in translational and vibrational degrees of freedom, respectively, and are defined in Section 2.3. These

two quantities describe the coupling between the electrical current and the neutral gas.

[15] An important contribution for the thermal conductivity comes from the chemical reactions occurring in the plasma [*Boulos et al.*, 1994, pp. 271–273]. For instance, the two peaks in the dependence of $\kappa_T(T)$, shown in Figure 2a, are related to the dissociation of O_2 [e.g., *Raizer*, 1991, Figure 10.20] and N_2 [e.g., *Boulos et al.*, 1994, Figure 7.2] molecules. In this work, we use the thermal conductivity κ_T from *Boulos et al.* [1994, pp. 413–417], which is calculated under the assumption of local thermodynamical and chemical equilibrium, at ground level pressure. In a more general case, the contribution for κ_T, coming from the chemical reactions in the plasma, depends on pressure and gas composition. The general description of all components of the thermal conductivity in the nonequilibrium case [e.g., *Chen and Li*, 2003; *Nemchinsky*, 2005; *D'Angola et al.*, 2008] is beyond the scope of the present work. We also introduce a simplified version of the thermal conductivity $\kappa_T^{**} = 19k_B\mu_v/4m_{air}$, where $m_{air} = \rho_{amb}/N_{amb}$ is the average mass of an air molecule. This definition of κ_T^{**} is obtained from the Eucken relationship between the thermal conductivity and the viscosity coefficient by assuming that the specific heat ratio ($\gamma = 7/5$) is independent of temperature [e.g., *Hirschfelder et al.*, 1964, pp. 499–501; *Boulos et al.*, 1994, pp. 294–295; *Laurendeau*, 2005, p. 312]. Hence, κ_T^{**} only accounts for energy transport associated to translational and rotational degrees of freedom, neglecting the contributions of vibrational degrees of freedom and chemical reactions. The coefficient κ_T^{**} is also shown in Figure 2a. In all calculations in this paper, we use the coefficient κ_T^{*}, defined by equation (7). The coefficient κ_T^{**} is only used to demonstrate (please see Section 4.2) that the results and conclusions of the present work do not have a significant dependence on the choice of thermal conductivity description.

[16] Transport equations (1)–(4) are written in the general form of a hyperbolic equation [e.g., *Potter*, 1973, equation (3.78); *Hoffman*, 2001, p. 651] and solved with finite differences [e.g., *Sparrow and Raspet*, 1991]. The transport equations are solved with second-order midpoint integration in time [e.g., *Potter*, 1973, equations (2.91)–(2.92); *Hoffman*, 2001, p. 365]. Advective (hyperbolic) transport terms are discretized with first-order upwind scheme [e.g., *Hoffman*, 2001, p. 673]. On the other hand, parabolic terms [e.g., *Potter*, 1973, equation (3.111); *Hoffman*, 2001, p. 587], such as heat conduction, viscosity, and diffusion, are discretized with second-order central differences [e.g., *Hoffman*, 2001, p. 598]. Equations are solved on a nonuniform radial grid with finest resolution of $\Delta r_1 = 3 N_0/N_{amb}$ μm at the axis of symmetry, which is $\Delta r_1 = r_c/100$. The grid size Δr_i increases radially following an exponential function. Numerical tests performed with flux-corrected transport schemes [*Boris and Book*, 1973; *Zalesak*, 1979] showed that the upwind scheme performs satisfactorily well near the axis of symmetry for the grid resolution Δr_i used in this work.

2.2. Kinetic Scheme

[17] To describe the plasma composition, a comprehensive kinetic scheme is employed, containing 21 species including: neutrals N_2, O_2, O, N, NO; neutral species with excited electronic states $O_2(a\,^1\Delta_g)$, $N_2(A\,^3\Sigma_u^+)$, $N_2(B\,^3\Pi_g)$,

$N_2(a'^1\Sigma_u^-)$, $N_2(C\,^3\Pi_u)$, $O(^1D)$, $O(^1S)$, $N(^2D)$; electrons e; negative ions O^-, O_2^-, O_3^-; and positive ions NO^+, O_2^+, O_4^+, $O_2^+N_2$. Hereafter, the excited electronic states of diatomic molecules are represented by simplified notation: $O_2(a)$, $N_2(A)$, $N_2(B)$, $N_2(a')$, and $N_2(C)$ [e.g., *Kossyi et al.*, 1992]. In the above nomenclature, $N_2(B)$ is an effective state corresponding to the triplet states $N_2(B\,^3\Pi_g)$, $N_2(W\,^3\Delta_u)$, and $N_2(B'\,^3\Sigma_u^-)$. Hence, the states $N_2(W\,^3\Delta_u)$ and $N_2(B'\,^3\Sigma_u^-)$ are assumed to relax instantaneously to the state $N_2(B\,^3\Pi_g)$, and they are represented by the effective state $N_2(B)$ [*Kossyi et al.*, 1992, equation (2)]. Similarly, $N_2(a')$ describes the singlet states $N_2(a'^1\Sigma_u^-)$, $N_2(a^1\Pi_g)$, and $N_2(w^1\Delta_u)$, and $N_2(C)$ accounts for $N_2(C\,^3\Pi_u)$, $N_2(E\,^3\Sigma_g^+)$, and $N_2(a''\,^1\Sigma_g^+)$ [e.g., *Kossyi et al.*, 1992; *Popov*, 2001; *Flitti and Pancheshnyi*, 2009]. All model species described by a continuity equation with allowance for radial advection and diffusion:

$$\frac{\partial n_j}{\partial t} + \vec{\nabla}\cdot(n_j\vec{v}) = S_j + \vec{\nabla}\cdot(D_j\vec{\nabla}n_j), \tag{8}$$

where all species are assumed to be transported with the bulk velocity of neutral gas $\vec{v}$ [e.g., *Popov*, 2003, equation (4)]. Neutral species are assumed to diffuse with the same coefficient $D_N = D_V$. Its ambient (ground level) value 1.7×10^{-5} m^2/s is of the order of magnitude of the diffusion coefficient for several binary mixtures of atmospheric gasses at ambient temperature and ground pressure, as can be seen in Table 6.2 of *Capitelli et al.* [2000, p. 97]. On the other hand, charged species are assumed to follow ambipolar diffusion dynamics [e.g., *Raizer*, 1991, p. 28] with ambipolar diffusion coefficient $D_a \approx k_B\mu_p T_e/q_e$, where μ_p is the positive ion mobility [*Morrow and Lowke*, 1997, equation (A14)], T_e the electron temperature (equation (A1) in the Appendix A), and q_e the electronic charge. The diffusion coefficients D_N, D_V, and D_a are inversely proportional to the air density, carrying, therefore, the same scaling as electron and ion mobilities.

[18] The 21 species are assumed to participate in a total of 106 reactions presented in Table A1 in the Appendix A. This set contains the 67 reactions previously presented in Table 2 of *Riousset et al.* [2010b] and is further extended to include processes that gain importance at high temperature. The kinetic scheme adopted for the present study explicitly includes the NO^+ specie and its pertinent chemistry. For instance, at ground pressure, associative ionization, producing NO^+ ions, (reaction R5 in Table A1) and electron recombination with NO^+ ions (reaction R11) are the dominant mechanisms for electron density maintenance at temperatures higher than 4500 K [*Aleksandrov et al.*, 1997].

[19] The source term in the electron number density equation, for example, can be written as [*Naidis*, 1999, equation (7)]:

$$S_e = (\nu_{ion} + \nu_{step} + \nu_{assoc} + \nu_{det} - \nu_{a2} - \nu_{a3} - \nu_{rec})n_e, \tag{9}$$

where ν_{ion} corresponds to electron-impact ionization of N_2 and O_2 (reactions R1 and R2), ν_{step} to stepwise ionization of O atoms and NO molecules (reactions R3 and R4), ν_{assoc} to associative ionization in collisions between N and O atoms and in collisions between $N_2(a'^1\Sigma_u^-)$ and $N_2(A\,^3\Sigma_u^+)$ molecules (reactions R5–R7), ν_{det} to electron detachment of negative ions (reactions R15–R24), ν_{a2} to two-body attachment to O_2 molecules (reaction R8), ν_{a3} to three-body attachment (reaction R9), and ν_{rec} to electron-ion recombination (reactions R10–R14).

[20] The rate coefficients in Table A1 effectively depend on four quantities: E, N, T, and T_V. The axial electric field E can be calculated from the current I through Ohm's law, which in cylindrical coordinates can be expressed as [*Popov*, 2003, equation (3)]:

$$E = \frac{I}{\int_0^\infty \sigma(r)\,2\pi r\,dr}, \tag{10}$$

where r is the radial coordinate and $\sigma(r)$ the radially dependent electrical conductivity. Expression (10) has the form $E = \mathcal{R}I$, where $\mathcal{R}$ is the channel's linear resistance with units of Ω/m. The neutral gas density N is mainly governed by gas-dynamic expansion (equation (1)) and dissociation (reaction R58). The translational and vibrational temperatures (T and T_V) are calculated by inverting equations (5) and (6), respectively.

[21] Under conditions of vibrational nonequilibrium, when $T_V > T$, rates of electron-impact processes (R1–R4, R8, R25–R32) are accelerated due to super elastic collisions with vibrationally excited N_2. In the present modeling, such an effect is accounted for through the multiplication factor [*Benilov and Naidis*, 2003, equation (8)]:

$$F = \exp\left[C\frac{\exp(-\hbar\omega/k_B T_V)}{(E/N)^2} \right], \tag{11}$$

where E/N is given in Td (1 Td $= 10^{-17}$ V·cm^2) and $C = 6500$ Td^2. Figure 2b shows the dependence of F on vibrational temperature. Similarly, the conditions of vibrational nonequilibrium facilitate dissociation of N_2. This effect can be accounted for by using a two-temperature rate coefficient in reaction R58 [e.g., *Fridman and Kennedy*, 2004, pp. 151–154]. Such effect is accounted for through the inclusion of the factor [*Krivonosova et al.*, 1991]:

$$Z(T, T_V) = \frac{1 - \exp(-\hbar\omega/k_B T_V)}{1 - \exp(-\hbar\omega/k_B T)} \exp\left[-\frac{\theta_D - \beta T}{T_m} \right], \tag{12}$$

where $\theta_D = 113{,}260$ K is the dissociation temperature of N_2 (note that $\mathcal{E}_{N_2}^D = k_B \theta_D = 9.76$ eV is the dissociation potential of N_2 [*Capitelli et al.*, 2000, p. 87]), $\beta = 3$, and $1/T_m = 1/T_V - 1/T$.

[22] The kinetic scheme includes two- (reactions R84–R101) and three-body (R102–R106) ion-ion recombination reactions [*Kossyi et al.*, 1992]. Note that although *Kossyi et al.* [1992] did not list three-body recombination between O_2^- and O_4^+ ions (reaction R106), we have included this process following approach described by *Pancheshnyi et al.* [2005]. The importance of reaction R106 is also highlighted by *Smirnov* [1982, p. 140] and *Raizer* [1991, p. 63]. However, we emphasize that the dominant ion-ion recombination reactions in our system are the ones that involve O^- ions, which are the dominant negative ion specie. Rates of ion-ion recombination (reactions R84–R106) depend on ion temperature T_i (equation (A2) in the Appendix A), while rates of ion-molecule reactions (reactions R23, R70, R72–R75, R83) depend on the effective temperature of ions colliding with neutrals T_{Rj}^{eff} (equation (A3) in the Appendix A).

[23] The kinetic scheme includes the most important electron detachment reactions (R15–R24) in an air plasma [*Kossyi et al.*, 1992]. Among these reactions, the dominant one is reaction R15 of electron detachment in collisions between O^- and N_2. The dependence of the rate coefficient of reaction R15 on electric field is the same as used by *Luque and Gordillo-Vázquez* [2012], which is a simple analytical fit for the original measurements of *Rayment and Moruzzi* [1978]. The kinetic scheme also accounts for thermal dissociation of N_2, O_2, and NO (reactions R58–R60) and the respective inverse recombination reactions (R61–R63). We use the same coefficients for thermal dissociation and recombination reactions as *Krivonosova et al.* [1991] and *Aleksandrov et al.* [1997]. Following the steps of *Riousset et al.* [2010b], we assume that N_2^+, N_4^+, and O^+ are readily converted into O_2^+ ions and that densities of $N_2(B)$, $N_2(C)$, $O(^1D)$, $O(^1S)$, and $N(^2D)$ states are given by steady state approximations [*Naidis*, 1999, 2005; *Riousset et al.*, 2010b].

[24] We note that in contrast to several models in literature that use zero-dimensional chemistry [e.g., *Gallimberti*, 1979; *Aleksandrov et al.*, 1997; *Naidis*, 1999, 2005; *Aleksandrov et al.*, 2001a; *Gallimberti et al.*, 2002; *Bazelyan et al.*, 2007a; *Riousset et al.*, 2010b] or that use a simplified chemistry [e.g., *Rogoff*, 1972; *Jaeger et al.*, 1976; *Marode et al.*, 1979; *Vidal et al.*, 2002; *Shneider et al.*, 2012], the present model locally updates, using equation (8), the density of every specie considered, including all transport and chemical processes in which the specie is involved, at every point along the radial dimension.

[25] The continuity equations (8) are solved with the same numerical methods as the transport equations for neutral gas (1)–(4). Chemistry source terms are also integrated in time with second-order midpoint (or explicit two-step [e.g., *Potter*, 1973, pp. 34–35]) method under severe restrictions for the time step Δt, in order to capture the evolution of all kinetic and transport processes (e.g., $\Delta t \ll 1/\nu_{\mathrm{ion}}$, $1/\nu_{a2}$, $\Delta r_i/c_s$, $Nk_B\Delta r_i^2/\kappa_T$). Numerical tests performed with the DVODE package, which is a software package for time integration of first-order stiff differential equations, showed that the second-order midpoint method performs well for the very short time steps used in this work. The DVODE package is used in the ZDPlasKin tool for integration of chemistry equations [e.g., *Flitti and Pancheshnyi*, 2009, and references therein].

2.3. Energy Transfer From Charged to Neutral Particles

[26] Energy is transferred from the electrical current produced in the streamer zone to translational and vibrational degrees of freedom at a rate of:

$$Q_T^{\mathrm{eff}} = Q_T + Q_L + Q_i + Q_{VT} + Q_{VV} + Q_D, \tag{13}$$

$$Q_V^{\mathrm{eff}} = Q_V - Q_{VT} - Q_{VV} - 2Q_D, \tag{14}$$

respectively, in units of W/m^3 (see equations (3) and (4)). The rates of energy exchange, in the above equations (13) and (14), are defined as follows: Q_T corresponds to quenching of excited electronic states, Q_L to elastic collisions, Q_i is the Joule heating from the ion current, Q_V to the excitation of vibrations in N_2 molecules, Q_{VT} represents the vibrational-translational relaxation of the first excited vibrational level in N_2, Q_{VV} relaxation from upper levels, and Q_D to dissociation (see further discussion below).

[27] The rate of energy lost (per unit volume) by the plasma species and gained by the neutrals is $Q = \sigma E^2 = (\sigma_e + \sigma_i)E^2$, where σ_e and σ_i are the electron an ion conductivities,
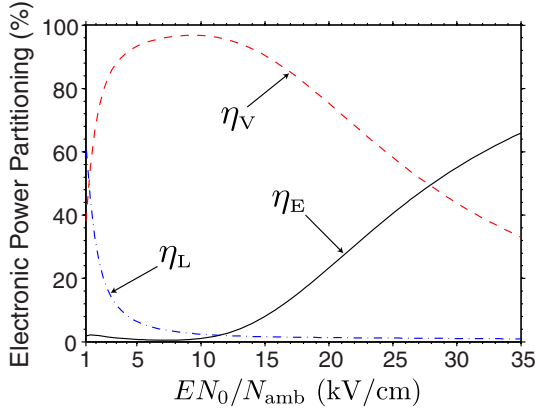
Figure 3. Partition of electronic power in a discharge in air. The fractions are calculated using BOLSIG+ [*Hagelaar and Pitchford*, 2005] for a composition of 79% of N_2 and 21% of O_2 at ambient temperature of 300 K.

respectively. The total electrical conductivity is defined as the sum $\sigma = \sum_j q_j \mu_j n_j$ over all charged species (q_j, μ_j, and n_j are the charge, mobility, and density, respectively, of charged species; mobilities are taken from *Morrow and Lowke* [1997, equations (A8)–(A14)]). Note that in equation (13), all ionic (volumetric) power $Q_i = \sigma_i E^2$ is assumed to be transferred directly into translational degrees of freedom. The electronic power $Q_e = \sigma_e E^2$, on the other hand, requires a special treatment. The deposition of electronic power can be conveniently partitioned into three channels: (1) excitation of vibrations, (2) elastic collisions, and (3) excitation of electronic states. The first one accounts for excitation of the first 8 vibrational levels in N_2 molecules, and it is defined as $Q_V = \eta_V \sigma_e E^2$. The second one is the electronic power spent in elastic collisions with O_2 and N_2 molecules, including excitation of rotations (in both) and vibrations in O_2 (that quickly relax into translational energy), and it is defined as $Q_L = \eta_L \sigma_e E^2$. The third one is represented as $Q_E = \eta_E \sigma_e E^2$ and comprises ionization (R1–R4), excitation of electronic states including metastables (R25–R29), and dissociation (R30–R32). The dependence of the three fractions η_V, η_L, and η_E on EN_0/N, calculated using BOLSIG+ [*Hagelaar and Pitchford*, 2005] (with cross sections from the Phelps database [*Lawton and Phelps*, 1978; *Phelps and Pitchford*, 1985]), is shown in Figure 3. It can be seen from the figure that most of electronic power (in the electric field range displayed) is spent on excitation of vibrations in N_2 molecules. In our calculations, we use the fractions η_V and η_L, shown in Figure 3, to calculate Q_V and Q_L in equations (13) and (14).

[28] The dependence of η_V and η_L on plasma composition is taken into account by simply reducing them proportionally to the number fraction of N_2 and O_2 as these molecules dissociate. The elastic power loss is proportional to the number fraction of the molecules colliding with electrons, for example, $\eta_L \propto n_{O_2}/N$, and we ensure that n_{O_2} and N are the updated values, as function of time and radial position, of the O_2 and total neutral gas densities (see also definitions of energy fractions by BOLSIG+).

[29] The dependence of η_V on T_V is taken into account by subtracting the increase in Q_E due to the nonequilibrium factor F, presented in equation (11), i.e., $\eta_V \propto [k_V^* n_e n_{N_2} - (F-1)Q_E/F]/\sigma_e E^2$, where k_V^* is the rate coefficient for

electron-impact excitation of vibrations in N_2 and $(F-1)Q_E/F$ is the power gained by electrons in superelastic collisions with excited $N_2(v)$ that contributes to the increase of Q_E, since $Q_E \propto F$ (more details on the method for evaluation of Q_E are provided below).

[30] The rate of energy exchange between electrons and neutrals that comes from the collisional quenching of excited atomic and molecular states is typically defined in gas discharge literature as $Q_T = 0.3 Q_E$, where $Q_E = \eta_E \sigma_e E^2$ [*Aleksandrov et al.*, 1998; *Naidis*, 1999, 2005; *Riousset et al.*, 2010b]. The approximation that 30% of η_E contributes to gas heating was introduced by *Aleksandrov et al.* [1998] to explain available experimental data on nitrogen discharges and they assert that this is probably applicable for a discharge in air, as well. To apply this approximation, η_E can be calculated with BOLSIG+, as done by *Riousset et al.* [2010b]. The obtained η_E fraction is shown in Figure 3, to illustrate the discussion. Instead of using the abovementioned approach, we introduce a method to calculate Q_E and Q_T, directly from the chemical reactions, based on the work by *Popov* [2001]. This method is more general than the above described approach and accounts for the scaling of η_E and η_T fractions with air density at different altitudes in the Earth's atmosphere. Thus, η_E calculated with BOLSIG+ is only used in this work to illustrate the discussion in this section and for the sake of comparison. All model results are obtained with Q_E and Q_T as described in the next paragraph.

[31] The rate of energy transfer due to electron-impact excitation of electronic states is defined as $Q_E = \sum_j \mathcal{E}_j^* S_j$, where $\mathcal{E}_j^*$ is the excitation threshold, S_j is the reaction rate, and the summation is performed over all reactions listed in Table 1 (the corresponding energy thresholds and literature reference are listed in the table). Similarly, the rate of energy transferred to translational degrees in chemical reactions is defined as $Q_T = \sum_j \mathcal{E}_j^T S_j$, where $\mathcal{E}_j^T$ is the excess kinetic energy of products, S_j is the reaction rate, and the summation is performed over all reactions listed in Table 2. The amount of energy transferred to translational degrees of

Table 1. Electron-Impact Ionization, Excitation, and Dissociation Reactions

	Reaction	$\mathcal{E}_j^*$ (eV)	Reference
R1	$O_2 + e \rightarrow O_2^+ + e + e$	12.08	*Capitelli et al.* [2000, p. 85]
R2	$N_2 + e \rightarrow N_2^+ + e + e$	15.58	*Capitelli et al.* [2000, p. 85]
R3	$NO + e \rightarrow NO^+ + e + e$	9.26	*Capitelli et al.* [2000, p. 85]
R4	$O + e \rightarrow O^+ + e + e$	13.62	*Capitelli et al.* [2000, p. 85]
R25	$N_2 + e \rightarrow N_2(A) + e$	6.17	*Capitelli et al.* [2000, p. 121]
R26	$N_2 + e \rightarrow N_2(B) + e$	7.35	*Capitelli et al.* [2000, p. 121]
R27	$N_2 + e \rightarrow N_2(a') + e$	8.4	*Capitelli et al.* [2000, p. 121]
R28	$N_2 + e \rightarrow N_2(C) + e$	11.03	*Capitelli et al.* [2000, p. 121]
R29	$O_2 + e \rightarrow O_2(a) + e$	0.98	*Capitelli et al.* [2000, p. 122]
R30[a]	$N_2 + e \rightarrow N + N(^2D) + e$	13	*Popov* [2011]
R31[b]	$O_2 + e \rightarrow O + O + e$	5.9	*Popov* [2011]
R32[c]	$O_2 + e \rightarrow O + O(^1D) + e$	8.34	*Popov* [2011]

[a]Reaction R30 occurs through the excitation of a predissociation state N_2^* with excitation energy $\mathcal{E}_{N_2^*}^* = 13$ eV and dissociation energy $\mathcal{E}_{N_2^*}^D = 12.1$ eV [*Popov*, 2011].
[b]Reaction R31 occurs through the excitation of a predissociation state O_2^* with excitation energy $\mathcal{E}_{O_2^*}^* = 5.9$ eV and dissociation energy $\mathcal{E}_{O_2^*}^D = 5.12$ eV [*Popov*, 2011].
[c]Reaction R32 occurs through the excitation of a predissociation state $O_2(B)$ with excitation energy $\mathcal{E}_{O_2(B)}^* = 8.34$ eV and dissociation energy $\mathcal{E}_{O_2(B)}^D = 7.08$ eV [*Popov*, 2011].

Table 2. Fast Heating Reactions

	Reaction	$\mathcal{E}_j^{\mathrm{T}}$ (eV)	Estimation Method or Reference
R10	$O_2^+ + e \rightarrow O + O(^1D)$	5	*Popov* [2001]
R11	$NO^+ + e \rightarrow O + N(^2D)$	5	$= \mathcal{E}_{\mathrm{R10}}^{\mathrm{T}}$
R12	$O_4^+ + e \rightarrow O_2 + O_2$	5	$= \mathcal{E}_{\mathrm{R10}}^{\mathrm{T}}$
R13	$O_2^+N_2 + e \rightarrow O_2 + N_2$	5	$= \mathcal{E}_{\mathrm{R10}}^{\mathrm{T}}$
R14	$O_2^+ + e + M \rightarrow O_2 + M$	5	$= \mathcal{E}_{\mathrm{R10}}^{\mathrm{T}}$
R30	$N_2 + e \rightarrow N + N(^2D) + e$	0.9	$= \mathcal{E}_{N_2^*}^* - \mathcal{E}_{N_2^*}^{\mathrm{D}} = 13 - 12.1$
R31	$O_2 + e \rightarrow O + O + e$	0.78	$= \mathcal{E}_{O_2^*}^* - \mathcal{E}_{O_2^*}^{\mathrm{D}} = 5.9 - 5.12$
R32	$O_2 + e \rightarrow O + O(^1D) + e$	1.26	$= \mathcal{E}_{O_2(B)}^* - \mathcal{E}_{O_2(B)}^{\mathrm{D}} = 8.34 - 7.08$
R35	$N_2(A) + O_2 \rightarrow N_2 + O + O$	1.05	$= \mathcal{E}_{N_2(A)}^* - \mathcal{E}_{O_2^*}^{\mathrm{D}} = 6.17 - 5.12$
R39	$N_2(A) + N_2(A) \rightarrow N_2(B) + N_2$	4	*Popov* [2001]
R41	$N_2(B) + O_2 \rightarrow N_2 + O + O$	2.23	$= \mathcal{E}_{N_2(B)}^* - \mathcal{E}_{O_2^*}^{\mathrm{D}} = 7.35 - 5.12$
R43	$N_2(a') + O_2 \rightarrow N_2 + O + O(^1D)$	1.32	$= \mathcal{E}_{N_2(a')}^* - \mathcal{E}_{O_2(B)}^{\mathrm{D}} = 8.4 - 7.08$
R45	$N_2(C) + O_2 \rightarrow N_2 + O + O(^1D)$	3.95	$= \mathcal{E}_{N_2(C)}^* - \mathcal{E}_{O_2(B)}^{\mathrm{D}} = 11.03 - 7.08$
R48	$O(^1D) + N_2 \rightarrow O + N_2$	1.96	$= \mathcal{E}_{O(^1D)}^*$
R50	$O(^1D) + O_2 \rightarrow O + O_2$	1.96	$= \mathcal{E}_{O(^1D)}^*$
R53	$N(^2D) + O_2 \rightarrow NO + O$	2.38	$= \mathcal{E}_{N(^2D)}^*$
R57	$O_2(b,v) + O_2 \rightarrow O_2(b) + O_2(v)$	0.37	$= \mathcal{E}_{O_2(v=2)}^*$

freedom per reaction act, shown in Table 2, is calculated following the approach of *Popov* [2001, 2011] and examples follow below.

[32] A major contribution for Q_{T}, and therefore for air heating, comes from quenching of excited N_2 molecules (reactions R35, R41, R43, and R45), as in reaction R41, for example. In this case $\mathcal{E}_{\mathrm{R41}}^{\mathrm{T}} = \mathcal{E}_{N_2(B)}^* - \mathcal{E}_{O_2}^{\mathrm{D}} = 2.23$ eV is given by the difference between the excitation energy of the $N_2(B)$ state, $\mathcal{E}_{N_2(B)}^* = 7.35$ eV, and the amount of energy required to dissociate the O_2 molecule, $\mathcal{E}_{O_2}^{\mathrm{D}} = 5.12$ eV [*Popov*, 2011]. For the sake of simplicity, we assume that molecules produced in all reactions in Table 2 relax instantaneously to the ground vibrational level. Another important contribution for air heating comes from electron-impact dissociation. For example, in reaction R30, $\mathcal{E}_{\mathrm{R30}}^{\mathrm{T}} = \mathcal{E}_{N_2^*}^* - \mathcal{E}_{N_2^*}^{\mathrm{D}} = 0.9$ eV is defined as the difference between the excitation energy of a predissociation state N_2^*, $\mathcal{E}_{N_2^*}^* = 13$ eV, and its dissociation threshold with products $N + N(^2D)$, $\mathcal{E}_{N_2^*}^{\mathrm{D}} = 12.1$ eV [*Popov*, 2011]. Our model also accounts for air heating in electron-ion recombination (reactions R10–R14). An amount $\mathcal{E}_{\mathrm{R10}}^{\mathrm{T}} = 5$ eV is released in the form of kinetic energy of atomic oxygen products in reaction R10 [*Popov*, 2001]. We assume that the same amount is released in electron recombination with other positive ion species, since R10 is dominant during initial stages of air heating. The model also accounts for self-quenching of $N_2(A)$ (reaction R39) and quenching of $O(^1D)$ (reactions R48 and R50) [*Popov*, 2001]. We also assume that the excited state $O_2(b^1\Sigma_g^+, v = 2)$ [*Popov*, 2001, Section 4], referred in short as $O_2(b,v)$, produced in reactions R36 and R49, quickly exchanges its vibration excitation with ground state O_2 molecules (reaction R57) [e.g., *Vallance Jones*, 1974, p. 116]. Heat release finally occurs due to vibrational relaxation of the produced $O_2(v)$ [*Popov*, 2011, Section 2.3].

[33] The method for estimation of the energy released, in the form of kinetic energy of products in every reaction, is listed in the fourth column of Table 2. If we write $Q_{\mathrm{T}} = \eta_{\mathrm{T}}\sigma_e E^2$, one can see that our approach gives effective values of the fractions $\eta_{\mathrm{T}} = \left(\sum_j \mathcal{E}_j^{\mathrm{T}} S_j\right)/\sigma_e E^2$

and $\eta_{\mathrm{E}} = \left(\sum_j \mathcal{E}_j^* S_j\right)/\sigma_e E^2$ as a function of E, N, T, T_{V}, and plasma composition. The air heating due to the energy release in the chemical reactions listed in Table 2 ($\partial T/\partial t \propto Q_{\mathrm{T}}$) is referred in literature as "fast heating mechanism" because this process is essentially instantaneous when compared with air heating due to vibrational-translational relaxation [see, e.g., *Aleksandrov et al.*, 2010]. In Section 3.2 we present the calculated values of these fractions and discuss the commonly used relation $\eta_{\mathrm{T}}/\eta_{\mathrm{E}} \approx 30\%$.

2.4. Vibrational-Translational Energy Relaxation

[34] In this section we describe the rates of energy exchange between vibrational and translational degrees of freedom: Q_{VT}, Q_{VV}, and Q_{D}. An important characteristic of the system under consideration is the strong vibrational nonequilibrium $T_{\mathrm{V}} \gg T$. In this case, high-energy vibrational levels are reasonably populated. In order to correctly capture this regime, we include the effects of the anharmonicity of N_2 molecule potential, accounting for the fact that the vibrational quantum is smaller at higher-energy levels [e.g., *Fridman and Kennedy*, 2004, p. 86]. Figure 4 illustrates the implications on the energy spacing between levels when considering both harmonic and anharmonic potentials for the N_2 molecule. We calculate the vibrational energy with the harmonic oscillator formula (6) [see, e.g., *Fridman and Kennedy*, 2004, p. 163] because it can be demonstrated that (under the excitation regime considered) the first vibrational levels can be fitted by a Boltzmann distribution with temperature T_{V}, leading to the expression for vibrational energy given by equation (6). Nonetheless, we include the effects of anharmonicity in the rates of vibrational-translational (VT) energy relaxation, following discussion by *Capitelli et al.* [2000, Chapter 3].

[35] The energy pumped and stored into vibrational levels of N_2 molecules relaxes from the lowest vibrational level into translational energy on a time scale τ_{VT}, mainly due to quenching by atomic oxygen [e.g., *Popov*, 2001]. The rate of VT energy exchange is given by the following expression [*Capitelli et al.*, 2000, p. 28]:

$$Q_{\mathrm{VT}} = \frac{\varepsilon_{\mathrm{V}}(T_{\mathrm{V}}) - \varepsilon_{\mathrm{V}}(T)}{\tau_{\mathrm{VT}}}, \tag{15}$$
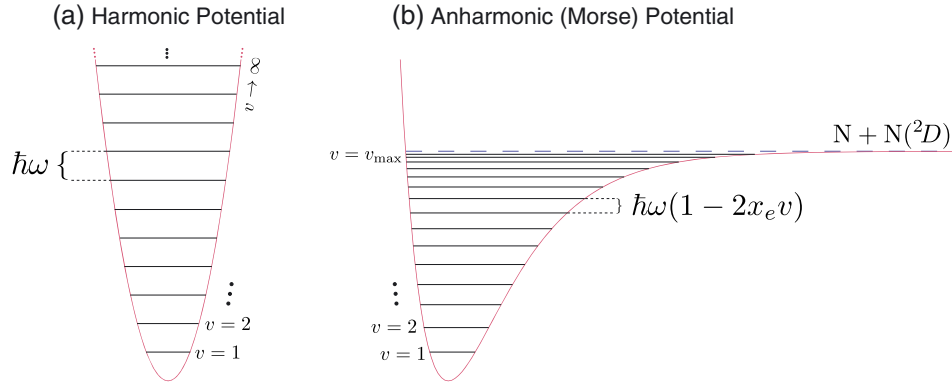
Figure 4. Illustration of (a) harmonic and (b) anharmonic potential models for the N_2 molecule. The harmonic (quadratic) potential imply the existence of an infinite number of vibrational energy levels equally spaced in energy by an amount $\hbar\omega$. The anharmonic (Morse) potential imply the existence of a limited number v_{max} of energy levels and that the energy spacing between levels decrease with increasing energy. The anharmonic potential is more realistic, and it is capable of explaining molecular dissociation.

calculated from the difference between the local value of the vibrational energy, $\varepsilon_V(T_V)$, and its equilibrium value at a temperature $T_V = T$, $\varepsilon_V(T)$. The VT relaxation time scale is defined as [*Chernyi et al.*, 2004, pp. 45, 79]:

$$\frac{1}{\tau_{VT}} = [1 - \exp(\hbar\omega/k_B T)] \sum_j k_j^{VT} n_j \mathcal{L}_j, \qquad (16)$$

with the summation performed over the five ground states: N_2, O_2, NO, N, and O. In the equation above, k_j^{VT} is the rate of deactivation of the first excited vibrational state of N_2 molecules in collisions with jth specie ($N_2(v=1) + M_j \to N_2(v=0) + M_j$) and $\mathcal{L}_j$ is the Losev correction factor [*Capitelli et al.*, 2000, p. 38]:

$$\mathcal{L}_j = \left[\frac{1 - \exp(-\hbar\omega/k_B T_V)}{1 - \exp\left[-(\hbar\omega/k_B T_V) + \delta_j^{VT}\right]} \right]^2, \qquad (17)$$

where $\delta_j^{VT} = 0.427 x_e (\hbar\omega/k_B) \mathcal{l} \sqrt{\mathcal{M}/T}$ is the inverse (dimensionless) radius of the VT exchange in collisions with jth specie, $x_e = 6.13\times10^{-3}$ is the anharmonicity coefficient, $\mathcal{l} \approx 0.2$ Å is the range of the repulsive Born-Mayer potential of the interaction, and $\mathcal{M}$ is the reduced mass of the colliding particles [*Capitelli et al.*, 2000, p. 107]. The VT relaxation term, as described by equations (15)–(17), is said to have a

Losev dependence and it includes effects of the anharmonicity of the N_2 potential in the rate of VT relaxation [*Losev*, 1981, p. 72]. The majority of models in gas discharge literature neglect this effect by setting $\mathcal{L}_j = 1$ (or $\delta_j^{VT} = 0$), in which case the VT relaxation term is said to have a Landau-Teller dependence [e.g., *Fridman and Kennedy*, 2004, p. 273]. The factor $\mathcal{L}_j$ introduces the dependence of Q_{VT} on T_V. Typically, this correction is very small in comparison with the change in Q_{VT} due to increase of neutral gas temperature T. Nonetheless, we have decided to keep $\mathcal{L}_j$ for the sake of completeness. Table 3 lists the rates for VT relaxation k_j^{VT} as well as the inverse radius δ_j^{VT} used in our work.

[36] In the regime of intense vibrational energy pumping $Q_V \gg Q_E$ at which Q_{VT} is inefficient, another mechanism governs the relaxation of vibrational energy. Note that Q_{VT} can only be an efficient mechanism for vibrational energy relaxation if T is high or in collision with atoms (see Table 3). Energy cannot be accumulated indefinitely in the first level, and it is rather transported upward in the "vibrational ladder" (Figure 4) in collisions with other N_2 molecules. The mechanism of vibrational-vibrational (VV) exchange follows the reaction $N_2(v') + N_2(v'') \to N_2(v'-1) + N_2(v''+1)$, where the preferential direction of the reaction is for $v'' > v'$ [e.g., *Fridman and Kennedy*, 2004, p. 175]. It can be seen, from Figure 4b, that the discrete propagation of a quantum in the

Table 3. Vibrational Relaxation Rates of N_2

Specie	δ_j^{VT} or δ_j^{VV}	k_j^{VT} or k_j^{VV} (cm^3/s)	Reference
	Adiabatic Vibrational-Translational Relaxation: $N_2(v=1) + M_j \to N_2(v=0) + M_j$		
Molecule		$k_j^{VT} = 6.4\times10^{-12} \exp(-137/T^{\frac{1}{3}})$	*Mnatsakanyan and Naidis* [1985]
N_2	$\delta_{N_2}^{VT} = 6.8/T^{\frac{1}{2}}$		
O_2	$\delta_{O_2}^{VT} = 7.0/T^{\frac{1}{2}}$		
NO	$\delta_{NO}^{VT} = 6.9/T^{\frac{1}{2}}$		
	Nonadiabatic Vibrational-Translational Relaxation: $N_2(v=1) + M_j \to N_2(v=0) + M_j$		
Atom		$k_j^{VT} = 2.3\times10^{-13} \exp(-1280/T)$ $+ 2.7\times10^{-11} \exp(-10840/T)$	*Capitelli et al.* [2000, p. 110]
N	$\delta_N^{VT} = 5.6/T^{\frac{1}{2}}$		
O	$\delta_O^{VT} = 5.8/T^{\frac{1}{2}}$		
	Vibrational-Vibrational Exchange: $N_2(v') + N_2(v'') \to N_2(v'-1) + N_2(v''+1)$		
N_2	$\delta_{N_2}^{VV} = 6.8/T^{\frac{1}{2}}$	$k_{N_2}^{VV} = 2.5\times10^{-14}(T/300)^{\frac{3}{2}}$	*Raizer et al.* [1995, p. 64]

vibrational energy space results in loss of vibrational energy because the spacing between levels becomes smaller and smaller. Assuming only single-quantum exchanges, at every step up in the vibrational ladder, the excess energy $2x_e\hbar\omega v$ is lost to translational degrees of freedom [e.g., *Fridman and Kennedy*, 2004, p. 275]. Therefore, the rate of VT relaxation because of VV exchange $Q_{VV} = \hbar\omega\Pi$ is proportional to the flux of quanta in the vibrational energy space Π [*Raizer et al.*, 1995, pp. 63–64], which is given by the following expression [*Biberman et al.*, 1987, p. 399]:

$$\Pi = \frac{4x_e k_{N_2}^{VV}}{(\delta_{N_2}^{VV})^3} \left(\frac{\hbar\omega}{k_B T}\right) n_{N_2(v=0)}^2 v_{Tr}^2 \exp\left[-2x_e v_{Tr}^2 \left(\frac{\hbar\omega}{k_B T}\right) - 1\right] \quad (18)$$

where $k_{N_2}^{VV}$ is the rate of the VV exchange (see Table 3) and $v_{Tr} = (T/x_e T_V + 1)/2$ marks the location (in the vibrational energy space) of the minimum of the Treanor distribution [*Capitelli et al.*, 2000, pp. 38–39]. The Treanor distribution describes a one-component system of anharmonic oscillators dominated by VV exchanges and was first derived by *Treanor et al.* [1968]. The inverse radius of the VV exchange is calculated in the same way as in the VT case, in fact, $\delta_{N_2}^{VV} = \delta_{N_2}^{VT}$ (Table 3). The density of unexcited N_2 molecules (with $v = 0$) is $n_{N_2(v=0)} = n_{N_2}[1 - \exp(-\hbar\omega/k_B T_V)]$ [*Raizer et al.*, 1995, p. 64]. The above described model for Q_{VV} is also used by *Shneider et al.* [2012] to study air heating and contraction of the plasma column of a glow discharge in nitrogen.

[37] Another consequence of strong vibrational nonequilibrium is the increase in the rate of N_2 dissociation (reaction R58) by the factor $Z(T, T_V)$. This occurs in the regime of incomplete vibrational relaxation $\tau_D < \tau_{VT}$, where $\tau_D = n_{N_2}/S_D$ is the N_2 dissociation time scale and S_D is the net dissociation rate given by the difference of rates R58 and R61. The rate of vibrational energy loss due to the loss of oscillators in dissociation is $2Q_D$, where $Q_D = \mathcal{E}_{N_2}^D S_D$. A simple inspection of equation (12) of *Treanor and Marrone* [1962] shows that the energy loss per dissociation act is $\sim \mathcal{E}_{N_2}^D = 9.76$ eV, in the limit $T_V \gg T$. Considering anharmonicity effects, this amount doubles. The total loss of energy to translational degrees of freedom in the excitation of the N_2 molecule from the ground state ($v = 0$) to the dissociation level ($v = v_{max}$) can be calculated by adding up the resonance defect $2x_e\hbar\omega v$ of each step up in the vibrational ladder (Figure 4b). This calculation gives an amount $\sim \mathcal{E}_{N_2}^D$ [*Fridman and Kennedy*, 2004, p. 275]. Therefore, in the dissociation of anharmonic oscillators under strong vibrational nonequilibrium $2\mathcal{E}_{N_2}^D$ is removed from the vibrational energy pool per dissociation act ($2Q_D$ in equation (14)), and half of this energy relaxes into kinetic energy (Q_D in equation (13)). The inclusion of $Z(T, T_V)$ and Q_D in our model accounts for all the details of the vibration-dissociation-vibration coupling [*Treanor and Marrone*, 1962; *Marrone and Treanor*, 1963]. In the considered system, this mechanism plays the role of clipping the vibrational temperature, even if excitation (Q_V) is very high. Vibrational temperature cannot increase indefinitely because strong nonequilibrium $T_V \gg T$ leads to increase in $Z(T, T_V)$; an increase in the dissociation rate leads to an increase in Q_D, reducing vibrational energy and, consequently, T_V. Note that Q_D also contributes to raise of T and accelerate other rates of vibrational energy relaxation.

3. Dynamics of Air Heating Driven by an Externally Maintained Electric Field

[38] In laboratory short nonuniform gaps, if the applied potential U_{gap} is such that the average electric field in the gap $E = U_{gap}/d$ (where d is the interelectrode distance) is higher than the critical electric field for stable streamer propagation E_{cr}, then the streamer can bridge the gap. The critical electric field for positive streamer propagation, for example, is $E_{cr} \approx 5$ kV/cm at ground pressure. Therefore, for a centimeter long gap, a streamer can bridge the space between anode and cathode if $U_{gap} > 5$ kV. After the streamer bridges the gap, the average electric field across the streamer body can be approximated as $E = (U_{gap} - U_{cath})/d$, where $U_{cath} \sim 0.2$ kV is the potential drop near the cathode [*Naidis*, 1999]. If the applied potential is such that the average electric field across the gap is lower than the conventional breakdown threshold E_k, the bridging of the gap does not necessarily lead to breakdown. The electric field threshold E_k is defined by the equality between ionization (reactions R1 and R2) and two-body attachment (R8) frequencies $\nu_{ion} = \nu_{a2}$ [*Raizer*, 1991, p. 135], i.e., $k_{R1}n_{O_2} + k_{R2}n_{N_2} = k_{R8}n_{O_2}$, and it has the value $E_k N_0/N = 28.51$ kV/cm for the rate coefficients used in the present work [*Benilov and Naidis*, 2003].

[39] A simplified schematics of the laboratory setup used to study the breakdown of short air gaps is sketched in Figure 5a. The actual electric circuit used in experiments to maintain a constant electric field across the gap is much more complicated [e.g., *Larsson*, 1998, Figure 1]. However, the schematics shown in Figure 5a is useful to illustrate the discussion below.

[40] A streamer can bridge a centimeter long gap on a nanosecond time scale. A simple estimate for average streamer speeds in the range 10^6–10^7 m/s shows that the streamer crosses the gap in 1–10 ns. However, experimental results show that the breakdown, or short-circuiting, of the gap occurs on much longer time scales, e.g., ~ 1 μs for an applied potential of 19 kV [*Černák et al.*, 1995; *Larsson*, 1998]. Figure 5b presents experimentally measured breakdown times by *Černák et al.* [1995] and *Larsson* [1998] (see original references for details). This shows that the breakdown is a consequence of the cumulative effects of a sustained current flowing through the body of the streamer [*Naidis*, 1999]. The breakdown process in this case is referred as streamer-to-spark transition (since the gap is short, there is no leader development). Below, we apply our model to simulate the kinetic and gas-dynamic processes in the streamer body during the development of a spark.

3.1. Breakdown of Short Air Gaps

[41] As pointed out in Section 1.2 [see also *Marode*, 1983], the channel-controlled framework is used in literature to describe the electrical breakdown of short air gaps, where the axial electric field remains approximately constant after streamer has bridged the gap [*Naidis*, 1999]. Although this approximation cannot be applied to describe the formation of a leader channel in open space (because a constant electric field cannot be enforced in the leader head), it is extremely useful for calibration of an air heating model, due to the availability of experimental data. In order to perform a validation of the proposed model, the breakdown times are calculated, following the approach of *Naidis* [2005] and
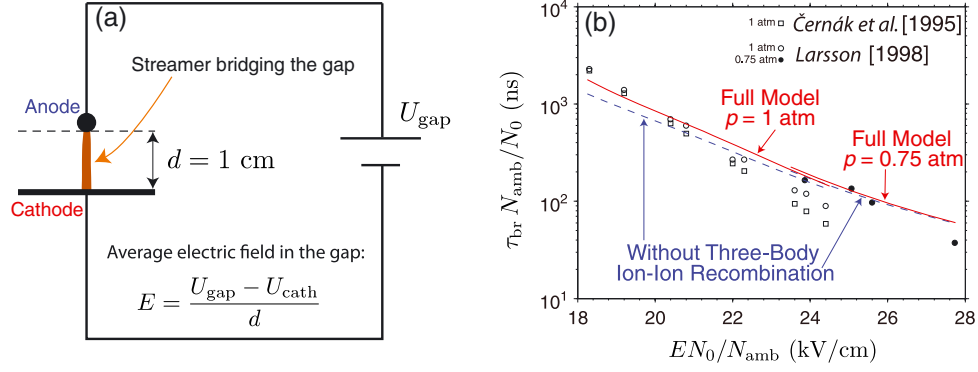
Figure 5. (a) Simplified schematics of laboratory setup to study the breakdown of nonuniform short air gaps. (b) Comparison of calculated values of streamer-to-spark transition time (τ_{br} defined as the time to heat the channel up to 5000 K) with laboratory measurements for two different pressures: 0.75 and 1 atm [*Černák et al.*, 1995; *Larsson*, 1998]. Solid/dashed lines represent simulation with/without the inclusion of three-body ion-ion recombination reactions. Figure 5b is plotted in the same format as Figure 4b of *Riousset et al.* [2010b].

Riousset et al. [2010b]. In this framework, a cross-sectional area of the streamer channel depicted in Figure 5a is simulated, under a constant applied electric field E. Calculations are performed for an initial electron density at the axis of the streamer channel equal to $n_{e,a} = 2\times10^{14}\, N_{amb}^2/N_0^2$ cm^{-3} and for an e-fold scale of its Gaussian radial distribution equal to $r_c = 0.3\, N_0/N_{amb}$ mm, the same values as used in subsequent sections. Experimentally, the breakdown time is the measured time delay between the streamer bridging the gap and the spark formation. Theoretically, the gap breakdown time τ_{br} is defined as the time to heat the streamer channel up to 5000 K [*Naidis*, 1999]. Figure 5b shows that the calculated breakdown times are in good agreement with

the experimental data obtained by *Černák et al.* [1995] and *Larsson* [1998] for two different pressures (1 and 0.75 atm), similarly to what was obtained by *Riousset et al.* [2010b, Figure 4b].

[42] We note that our model explicitly includes three-body ion-ion recombination reactions (R102–R106), which are dominant over two-body recombination (R84–R101) at ground level pressure and room temperature. These reactions play a significant role in determining the breakdown time at $p = 1$ atm and in the lower range of electric fields displayed in Figure 5b. The role of three-body reactions is reduced with the reduction of ambient pressure (or air density), as can also be seen from Figure 5b.
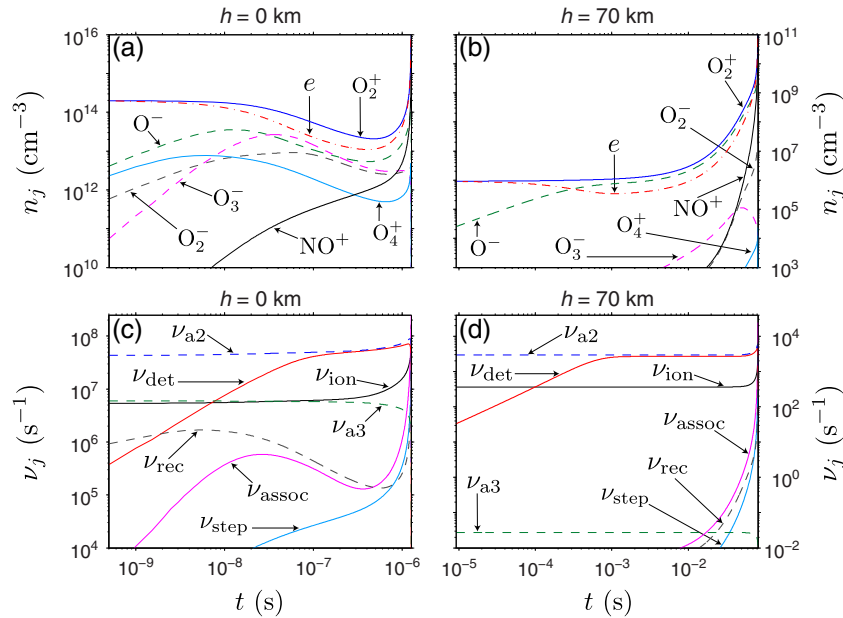

Figure 6. Temporal dynamics of (a,b) main charged species and (c,d) effective frequencies of electron production for (Figures 6a and 6c) ground pressure and (Figures 6b and 6d) 70 km altitude in the Earth's atmosphere. Panels present axial values of simulated quantities for an externally applied constant electric field equivalent to 19 kV/cm at ground pressure. Panels are presented for $t \leq \tau_{br}$.
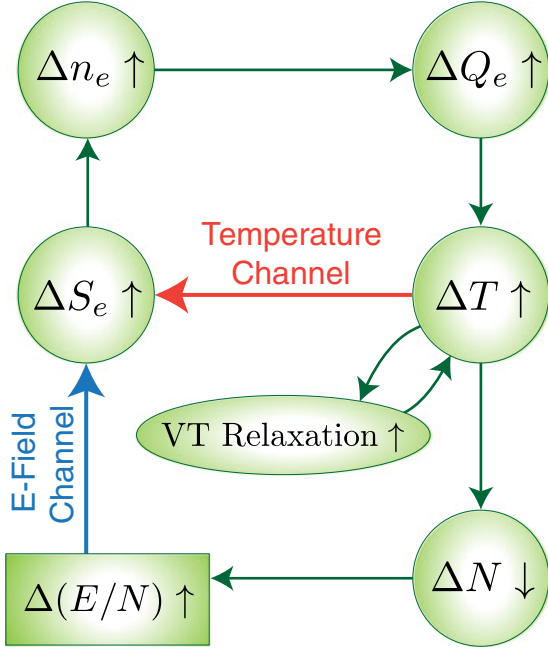
Figure 7. Schematic representation of the chain of processes involved in the thermal-ionizational instability. Upward/downward directed arrows represent an increase/decrease in a quantity (e.g., Δn_e ↑ represents an increase in electron density). Adapted from *Raizer* [1991, p. 222].

[43] The sequence of processes leading to the breakdown of short air gaps is referred as streamer-to-spark transition (there is no leader development in this case). Below, we discuss the physical mechanisms responsible for spark formation in these conditions. The electric field range shown in Figure 5b is a reasonable fraction of the conventional breakdown threshold E_k. For this electric field range, the transition is triggered by the kinetic mechanism alone, i.e., with no gas expansion. In fact, *Naidis* [1999] obtained good agreement with experimental data using a zero-dimensional model with constant gas density $N = N_{amb}$. Figure 6 presents the temporal dynamics of the (a,b) main plasma species and (c,d) effective frequencies of electron production for (a,c) ambient ground pressure and (b,d) 70 km altitude in the Earth's atmosphere. We note that at 70 km altitude, the ambient pressure is 6.9 Pa and $N_{amb} = 1.7 \times 10^{15}$ cm^3. The applied electric field is equivalent to 19 kV/cm at ground pressure. Figure 6 is presented in a format that can be compared to previous modeling works [*Naidis*, 1999, Figure 3; *Riousset et al.*, 2010b, Figures 7 and 9]. It can be seen that the initial response of the system is characterized by electron density decrease because the kinetic source term is negative at subbreakdown fields ($S_e < 0$ because $\nu_{a2} > \nu_{ion}$). Two-body dissociative attachment (reaction R8 in Table A1) results in accumulation of O$^-$ ions, which readily detach, mainly because of reaction R15. An effective detachment frequency ν_{det} can be defined such that $\nu_{det} \propto k_{R15} n_{N_2} n_{O^-}/n_e$ (see also equation (9)). Note that in contrast to ν_{ion} and ν_{a2}, ν_{det} depends on the ratio n_{O^-}/n_e [see, e.g., *Luque and Gordillo-Vázquez*, 2012]. On the time scale of electron detachment from O$^-$, the kinetic rate of electron production changes its sign ($S_e > 0$ because $\nu_{ion} + \nu_{det} > \nu_{a2}$).

This behavior was pointed out by *Naidis* [1999] for ground pressure (Figure 6c), and it is also evident at reduced air densities (Figure 6d), as demonstrated by *Riousset et al.* [2010b, Figure 9d]. Under these conditions, a small perturbation in electron density Δn_e is sufficient to trigger a thermal-ionizational (TI) instability [*Raizer*, 1991, p. 222]. Figure 7 contains a schematic representation of the chain of processes involved in a TI instability.

[44] The TI instability is a plasma instability that leads to unrestricted growth of electron density, and it can be started from any step in Figure 7. In the case of streamer-to-spark transition, electron detachment is the dominant triggering mechanism. The subsequent chain of processes occurs as follows: an increase in Δn_e leads to an increase in Joule heating ΔQ_e, that leads to an increase in temperature ΔT, that leads to a lowering of neutral gas density ΔN due to gas expansion, that leads to an increase in the reduced electric field $\Delta(E/N)$, that leads to an increase in the rate of electron production ΔS_e (e.g., ν_{ion}, ν_{step}), that leads to an increase in electron density, closing the chain. Note from Figure 7 that an increase ΔT leads to an increase in the rates of VT relaxation accelerating the temperature raise itself. Note also from the figure that the increase ΔS_e happens because of both increase in reduced electric field and temperature. For the streamer-to-spark transition, the "electric field channel" (rectangle in Figure 7) is dominant over the "temperature channel" for increase of ΔS_e because the electric field E is kept constant, and a slight reduction of N produces a considerable enhancement of E/N. Therefore, a system with a constant (maintained by an external source) and sufficiently high (to produce O$^-$ ions due to attachment) axial electric field is unstable. This is the case for the results shown in Figure 6. The change in sign of S_e occurs at 0.39 μs and 1.1 ms for ground and 70 km altitude, respectively, and it is clearly associated to the balance between ν_{a2} and ν_{det}. After the change in sign of S_e, breakdown is unavoidable. The breakdown occurs at 1.27 μs and 81.8 ms at ground and 70 km altitude, respectively. The time scale for electron detachment from negative ions increases with altitude inversely proportional to the decrease in ambient neutral gas density (i.e., $\tau_{det} \sim 1/k_{R15} n_{N_2}$). Our further analysis indicates that the breakdown time scales with air density close to $\propto 1/N_{amb}$ because it follows the electron detachment time scale $\tau_{det} \propto 1/N_{amb}$. This scaling is different from the expected air heating time scaling $\propto 1/N_{amb}^2$ (simple analysis of Joule heating process predicts that the air heating time scales with air density $\propto 1/N_{amb}^2$, see, e.g., Section 4.2). The $\propto 1/N_{amb}$ approximate scaling of the streamer-to-spark transition time is only possible because three-body attachment and electron-ion recombination, which play secondary role in the transition at ground pressure (Figure 6c), have even less importance at reduced air pressures (Figure 6d). Although *Riousset et al.* [2010b] did not attribute the $\propto 1/N_{amb}$ approximate scaling to the role of electron detachment in changing the sign of S_e, this effect was already visible in their results [e.g., *Riousset et al.*, 2010b, Figure 9d]. We would like to point out that detachment reactions are known to play a major role in nanosecond time-range spark formation in laboratory discharges [*Naidis*, 1999] and recently have received major attention in the context of transient luminous events [*Luque and Gordillo-Vázquez*, 2012; *Liu*, 2012; *Qin et al.*, 2012; *Neubert and Chanrion*, 2013].
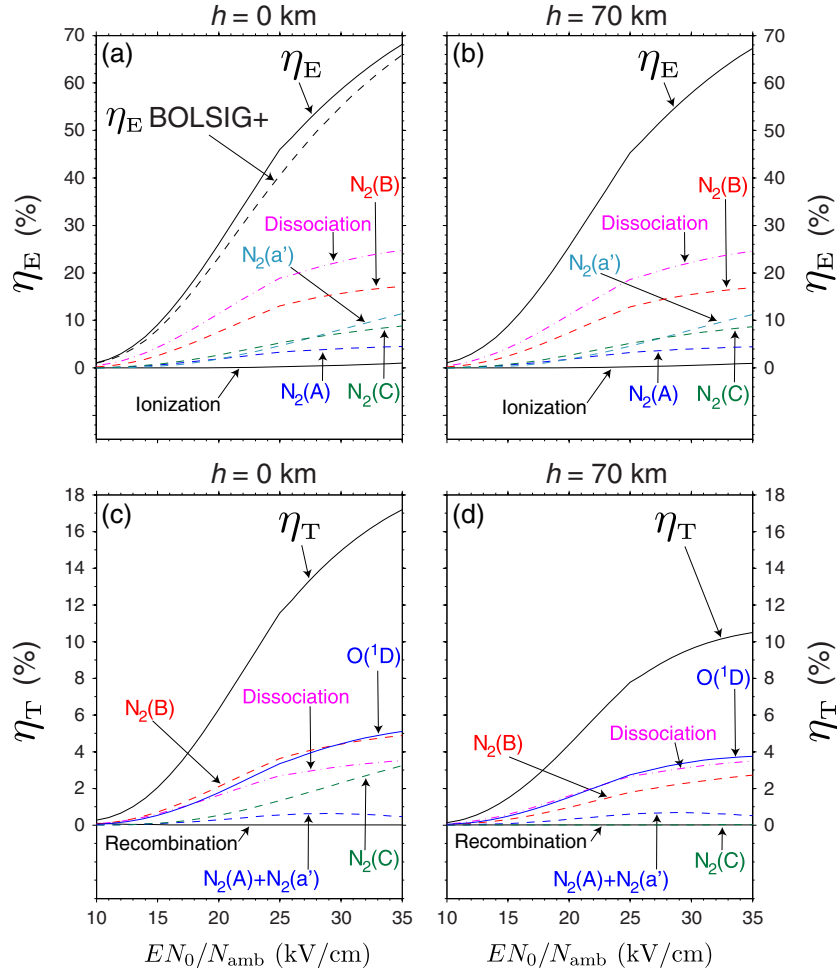
Figure 8. Instantaneous values of the (a,b) η_E and (c,d) η_T fractions at $t = 5\,N_0/N_{amb}$ ns for (Figures 8a and 8c) ground pressure and (Figures 8b and 8d) 70 km altitude. Time instant is arbitrarily chosen to avoid effects of VT relaxation (i.e., $t < \tau_{VT}$). Panels also show partitioning of η_E and η_T as in Tables 1 and 2, respectively.

3.2. Scaling of Fast Heating With Electric Field and Altitude

[45] Constant-field simulations can also be used to demonstrate the dependence of the fast heating mechanism on the axial electric field strength. The fast heating accounts for the energy released to neutrals in chemical reactions (Table 2). The main components of fast heating are quenching of excited electronic states and electron-impact dissociation [*Popov*, 2001]. As demonstrated in Figures 8 and 9, the fast heating represents only a small fraction of the electronic power. Figure 8 presents the electric field dependence of the η_E and η_T fractions. According to their definitions in Section 2.3, η_E and η_T are the fractions of electronic power spent on excitation of electronic states and gas heating, respectively. Figure 8 presents the instantaneous values of the two fractions and their partition in several channels listed in Tables 1 and 2. Comparing the calculated values of η_E at ground pressure (Figure 8a) and 70 km altitude (Figure 8b), we can see that η_E exhibits weak (or insignificant) dependence on pressure. It can also be seen that at moderate electric fields, most electronic power is spent on dissociation (R30+R31+R32) and excitation

of $N_2(B)$ state (R26). On the other hand, η_T is considerably reduced from ground (Figure 8c) to 70 km altitude (Figure 8d). At ground pressure, the main source of air heating is the quenching of $O(^1D)$ (including vibrational energy exchange of $O_2(b,v)$, i.e., R48+R50+R57) and $N_2(B)$ (R41) states. Additional contribution is from the excess kinetic energy of dissociation products (including quenching of $N(^2D)$, i.e., R30+R31+R32+R53) and, at the upper range of electric fields, from quenching of $N_2(C)$ state (R45). Figures 8c and 8d also display the contribution of $N_2(A)$ and $N_2(a')$ states (R35+R39+R43) and recombination (R10+R11+R12+R13+R14) to fast air heating.

[46] At 70 km altitude, the main contributions for air heating come from quenching of $O(^1D)$, dissociation, and quenching of $N_2(B)$ (Figure 8d). There is a reduction of the quenching efficiency of $N_2(B)$ and $N_2(C)$ states in the upper atmosphere. In fact, by equating the collisional and radiative quenching rates of $N_2(B)$ state $k_{R33} = n_{O_2}k_{R41}$, we can estimate the quenching altitude to be 66 km, in terms of standard nomenclature of auroral physics [*Vallance Jones*, 1974, p. 119]. Using the same procedure ($k_{R34} = n_{O_2}k_{R45}$), we can estimate the quenching altitude of the $N_2(C)$ state to
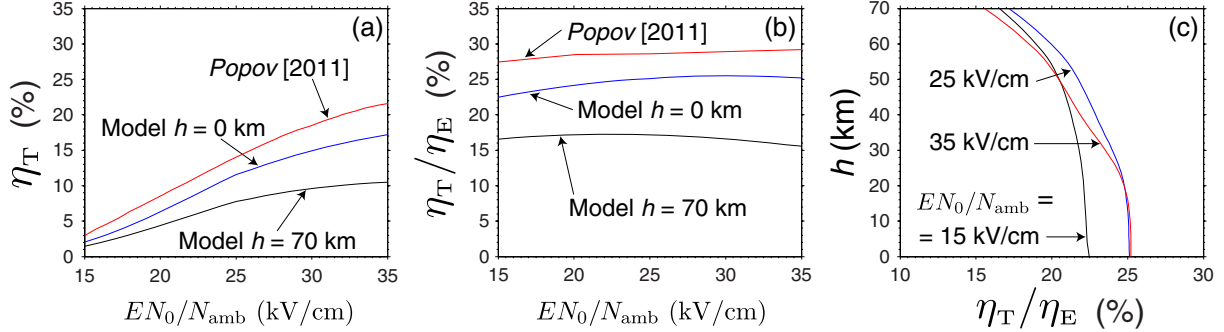
Figure 9. Comparison of instantaneous values of (a) η_T and (b) η_T/η_E, for two different pressures corresponding to ground and 70 km altitude, with calculations by *Popov* [2011, Figure 9], at ground level pressure. (c) Altitude dependence of η_T/η_E for three different values of reduced electric field.

be 30 km. Thus, Figure 8d shows that no air heating comes from quenching of $N_2(C)$ state at 70 km and the contribution of $N_2(B)$ is about half of its value at ground level. We would like to point out that our model specifically accounts for the quenching of $N_2(B)$ state by O_2 molecules (reaction R41). In contrast, previous works in the literature on transient luminous events [*Pasko*, 2007, and references therein] consider the $N_2(B)$ state to be collisionally deactivated by N_2 molecules. We emphasize that the deactivation by N_2 is slower and, therefore, places the corresponding quenching altitude at 53 km. Reaction R41 is broadly accepted in gas discharge literature as the main source of $N_2(B)$ collisional deactivation [e.g., *Kossyi et al.*, 1992; *Aleksandrov et al.*, 1997, 2010; *Popov*, 2001, 2011].

[47] In Figure 8a, the η_E fraction, given by the summation of all electronic excitation processes in BOLSIG+ (same as in Figure 3), is provided for comparison. Our modeled value of η_E overestimates the value calculated with BOLSIG+ by $\lesssim 5\%$. This occurs mainly due to the different electron-impact rate coefficients used in our work (from *Aleksandrov et al.* [1995] and *Benilov and Naidis* [2003]). Furthermore, Figure 9a emphasizes the reduction of η_T with altitude in Earth's atmosphere. As discussed in previous paragraph, this reduction is due to the fact that quenching of N_2 excited electronic states is less effective at upper altitudes. In fact, Figure 9b shows that η_T/η_E is $\sim 24.2\%$ at ground pressure and $\sim 16.4\%$ at 70 km altitude. The ratio η_T/η_E presents very weak dependence on reduced electric field EN_0/N_{amb} within the range 15–35 kV/cm. Figure 9c presents an altitude scan of the ratio η_T/η_E for $EN_0/N_{amb} = 15$, 25, and 35 kV/cm. It can be seen that for 15 kV/cm, the reduction of η_T/η_E is more significant above the quenching altitude of $N_2(B)$, while for 35 kV/cm, it is more significant above the quenching altitude of $N_2(C)$. The main conclusion to be drawn from Figure 9 is that the assumption that the ratio η_T/η_E is independent of electric field is a good first-order approximation at a given pressure, however, this ratio is not the same in such a wide range of pressures encompassing 0–70 km altitude.

[48] For comparison purposes, Figures 9a and 9b show the results from *Popov* [2011]. Although calculations by *Popov* [2011] describe a different discharge setup (at ground pressure), the difference in η_T/η_E is only ~ 4–5%. The slight difference is likely associated with differences in the methodology used to estimate the energy released to gas heating per reaction act ($\mathcal{E}_j^T$ in Table 2). The present modeling does not include details of vibrational excitation of the excited electronic states $N_2(A)$, $N_2(B)$, $N_2(a')$, and $N_2(C)$ (produced in reactions R25–R28), as well as for the N_2 products of quenching reactions R35, R41, R43, and R45. However, this simplification does not introduce significant deviations from the results by *Popov* [2001, 2011], as shown in Figure 9.

4. Dynamics of Streamer-to-Leader Transition and Its Scaling With Ambient Air Density

[49] Below, we describe the internal processes occurring in the leader head during the inception of a leader or the formation of a new section during its propagation, according to schematics presented in Figure 1a. The simulations describe the conversion of cold (room temperature) streamer to a hot (constricted) leader channel under a given constant current flowing through the channel [*Aleksandrov et al.*, 2001a; *Gallimberti et al.*, 2002; *Popov*, 2003]. The condition of an externally maintained (constant) electric field in the leader head is not generally valid. On the other hand, the assumption of continuity of the current, through the streamer zone, leader head, and channel, is more general. In this framework, the leader current is created by the ionization processes responsible for the development of the streamer zone and injected in the leader head [*Bondiou and Gallimberti*, 1994; *Goelian et al.*, 1997]. The parameterization of the results with respect to input electric current is also justifiable because the channel base current is a quantity easily obtainable from laboratory [see, e.g., *Andreev et al.*, 2008, Figure 4] and rocket-triggered lightning [see, e.g., *Lalande et al.*, 2002, Figure 4] experiments. In Section 4.1 a reference case, at ground level pressure, is discussed in detail, allowing to illustrate the details of the streamer-to-leader transition process and to compare our results with existing theoretical works [e.g., *Aleksandrov et al.*, 2001a; *Gallimberti et al.*, 2002; *Popov*, 2003]. In Section 4.2, the scaling of the streamer-to-leader transition time with ambient air density or altitude in the Earth's atmosphere is discussed.

4.1. Streamer-to-Leader Transition at Ground Level Pressure

[50] Figures 10 and 11 illustrate the temporal dynamics of the streamer-to-leader transition process for a constant electric current $I = 1$ A, at ambient ground pressure. The
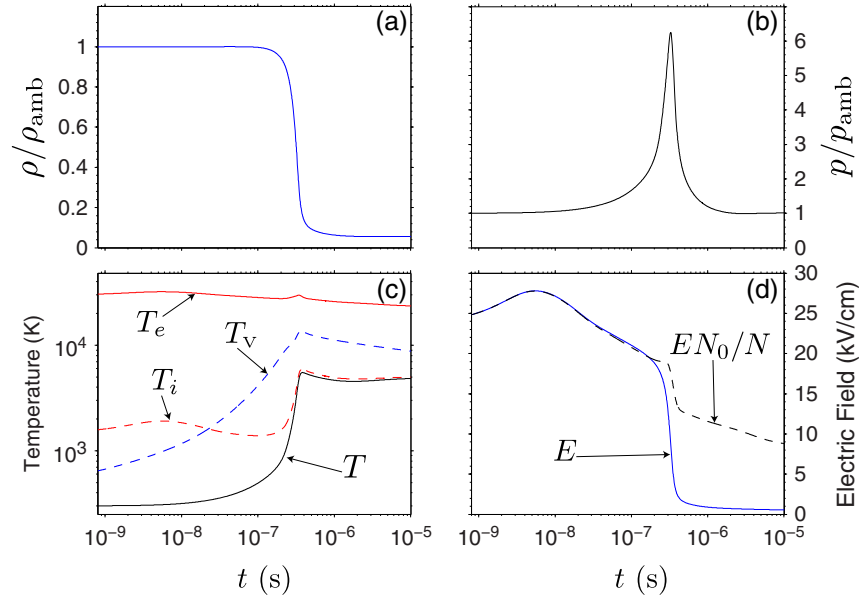
Figure 10. Temporal dynamics, at the discharge axis, of (a) change in air mass density ρ/ρ_{amb}, (b) change in pressure p/p_{amb}, (c) translational T, vibrational T_V, electronic T_e and ionic T_i temperatures, and (d) electric field E calculated from equation (10) and reduced field EN_0/N.

transition starts as a temperature rise (Figure 10c) due to the fast heating mechanism (Q_T in Figure 11c), which has two consequences: (first) an acceleration in the rates of VT relaxation (Q_{VT}, Q_{VV}, and Q_D), and (second) a qualitative change in the air ionization mechanism, from an interplay between electron-impact ionization (ν_{ion} in Figure 11d), dissociative attachment (ν_{a2}), and detachment (ν_{det}) to the associative ionization mechanism (ν_{assoc}). This process culminates in an even stronger rise in temperature and characterizes the TI instability for this system. As a consequence, a hot

leader channel with a stationary temperature of $\sim$5000 K is formed. Inside this highly conducting plasma channel, the axial electric field drops to a stationary value of $\sim$0.5 kV/cm (Figure 10d) and conductivity is mainly maintained by thermal ionization mechanisms (interplay between ν_{assoc} and recombination ν_{rec}). An important characteristic of this system is strong vibrational nonequilibrium (note $T_V \gg T$ in Figure 10c) that results in a predominance of Q_D over Q_{VT} and Q_{VV} (Figure 11c). Note that although Q_{VV} has its peak value below the other two rates of VT relaxation, Q_{VV} is the
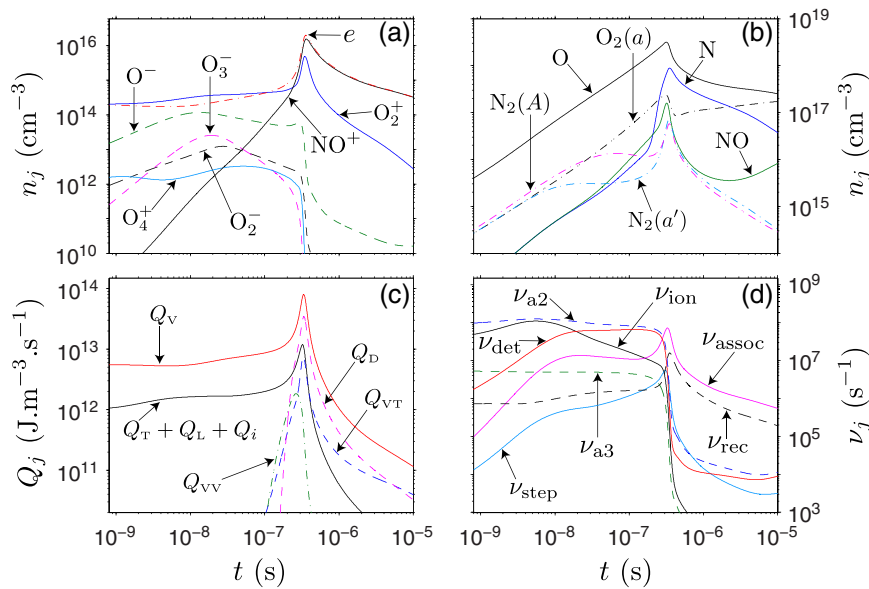

Figure 11. Temporal dynamics, at the discharge axis, of main (a) charged and (b) neutral plasma components, (c) rates of energy exchange from equations (13) and (14), and (d) effective frequencies of electron production and loss from equation (9).
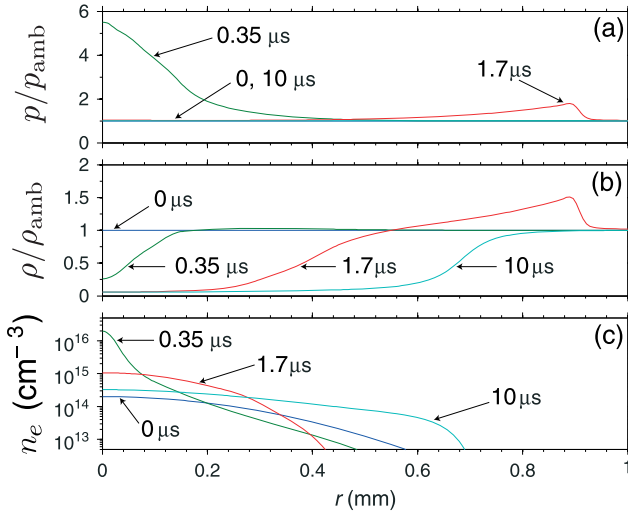
Figure 12. Radial dynamics of (a) change in pressure p/p_{amb}, (b) change in air mass density ρ/ρ_{amb}, and (c) electron density n_e, at four time instants: $t = 0$, 0.35, 1.7, and 10 μs.

first of the three rates to play a significant role. Also note that Q_{VT} is the dominant mechanism for air heating in the formed leader channel ($t \gtrsim 10$ μs). Figure 10c also illustrates the fact that $T_i \gg T$ before the transition, emphasizing the need to use the effective temperature T_{Rj}^{eff} in ion-molecule reactions.

[51] An important quantity to characterize the leader formation is the streamer-to-leader transition time scale τ_h, defined here as the time to heat the channel up to a temperature of 2000 K [*Popov*, 2003]. For $I = 1$ A at ambient ground pressure, we have $\tau_h = 0.29$ μs. At this moment of time, we can see a strong reduction in air density (Figure 10a) and increase in pressure (Figure 10b). The reduction of air density N is sufficient to keep the reduced electric field EN_0/N around 1 order of magnitude higher than the electric field E (note that electron-impact processes, such as ionization ν_{ion}, are function of E/N and not simply of E). Figure 11a shows a strong increase in the density of charged particles around $t \approx \tau_h$, characteristic of the TI instability. Since reaction R5 is the dominant mechanism of electron production at high temperatures, a change in the composition of positive ions occurs. Around $t \approx \tau_h$, NO$^+$ becomes the dominant ion (instead of O$_2^+$) and negative and complex ions disappear. Figure 11b illustrates the high level of dissociation of the neutral gas; practically all O$_2$ dissociates (note also the strong raise in density of N atoms). For this reason, at $t \approx \tau_h$, stepwise ionization (ν_{step} in Figure 11d) overcomes direct ionization (ν_{ion}), and ν_{step} even surpasses ν_{a2} because of the absence of O$_2$ molecules.

[52] A key role in the streamer-to-leader transition is played by the channel's radial dynamics, as illustrated in Figure 12. The energy deposition by Joule heating leads to a reduction of neutral density, which is stronger at the axis than in the periphery (as shown at $t = 0.35$ μs in Figure 12b). Electron production is radially nonuniform, also being stronger at the axis (Figure 12c). Consequently, the discharge channel contracts toward the axis enhancing the nonuniformity of the electronic power deposition Q_e. A strong raise in pressure occurs with a peak of 6.2 atm at $t \approx \tau_h$, and pressure is equalized on a time scale of a few

microseconds (Figure 12a). In fact, the time scale for pressure equalization across the channel is $\tau_c = c_s/r_c$, where c_s is the speed of sound and r_c is the initial radius (i.e., e-fold scale) of the current distribution [e.g., *Naidis*, 1999, 2005]. For $r_c = 0.3$ mm, at ambient ground pressure, $\tau_c = 0.87$ μs. Table 4 contains the ambient value of several time scales involved in the system under investigation. The time scale τ_c is a very useful parameter to characterize the gas-dynamic expansion of the channel. For $t \ll \tau_c$, air heating is isochoric ($\rho =$ const, see Figure 10a), while for $t \gg \tau_c$, heating is isobaric ($p =$ const, see Figure 10b). For a fixed value of the Joule heating rate Q, isochoric heating is faster than isobaric because in the former, the deposited volumetric power ($Q_T + Q_L + Q_i$) can be considered to contribute solely to temperature raise, while in the latter, it contributes to both temperature rise and gas expansion. Around $t \approx \tau_h$, the heating is strongly nonlinear and none of the isolated regimes applies.

[53] Although the rate of channel contraction increases during the development of the TI instability, the channel cannot be infinitely thin [e.g., *Bazelyan and Raizer*, 2000, p. 65]. A nonuniformity in electron density is smoothed because of the ambipolar diffusion. The ambient value for the time scale of ambipolar diffusion is $\tau_{D_a} = r_c^2/4D_a \approx 38$ μs (see Table 4). However, this value reduces significantly as the channel contracts because $\tau_{D_a} \propto r_c^2$ and it becomes comparable to τ_h, placing a bound for the instability development. As for example, when r_c drops to $\sim 1/10$ of its initial value (see Figure 12c), we have $\tau_{D_a} \sim \tau_h$. Air heating is the most significant process that drives the streamer-to-leader transition. Hence, it is important to introduce an additional time scale. The time scale for heat conduction across the channel is $\tau_{\kappa_T} = Nk_B r_c^2/4(\gamma - 1)\kappa_T$ (see Table 4). Its ambient value is ~ 700 μs at $T = 300$ K. Similarly to τ_{D_a}, in the hot and contracted channel, $\tau_{\kappa_T} \sim \tau_h$. Since temperature-dependent ionization processes are the dominant source of electrons at $t \approx \tau_h$, heat conduction also contributes to placing a limit on the growth rate of the TI instability [e.g., *Bazelyan and Raizer*, 2000, p. 65].

[54] The most pronounced differences in the TI instability occurring at constant current, instead of constant electric field, come from the fact that equation (10) introduce an effective relationship $E \propto 1/n_e$. At the beginning of the simulation, the electric field is $E_{amb} = I/\sigma \pi r_c^2 \approx 23$ kV/cm. At this electric field strength, two-body attachment (ν_{a2}) is the dominant (negative) component in the electron production rate $S_e < 0$ (Figure 11d). Similarly, to the streamer-to-spark transition at constant electric field considered in Section 3.1, on the time scale of electron detachment from O$^-$ ions, the sign of S_e becomes positive. However, at constant current, the electric field drops (Figure 10c). Hence, in this case, the change in the air ionization mechanism, from electron-impact to thermal ionization, $S_e(E/N) \rightarrow S_e(T)$, is a necessary condition for streamer-to-leader transition. A simple inspection in the schematic representation of the TI instability (Figure 7) leads to the conclusion that the streamer-to-leader transition cannot efficiently proceed by the "electric field channel" (rectangle in Figure 7) because the lowering of neutral density is not enough to compensate the drop in the electric field (see Figure 10d). This is the key difference between the constant-field and constant-current instabilities. The former proceeds mainly by the

Table 4. Ambient Values of Main Time Scales Involved in the Streamer-to-Leader Transition Process[a]

Process	Definition	Ambient Value[b] (s)
Direct ionization	$\tau_{\text{ion}} = \dfrac{1}{k_{\text{R1}}n_{O_2} + k_{\text{R2}}n_{N_2}}$	$\sim 3.7 \times 10^{-8}\, N_0/N_{\text{amb}}$
Two-body attachment	$\tau_{\text{a2}} = \dfrac{1}{k_{\text{R8}}n_{O_2}}$	$\sim 1.3 \times 10^{-8}\, N_0/N_{\text{amb}}$
Three-body attachment	$\tau_{\text{a3}} = \dfrac{1}{k_{\text{R9}}n_{O_2}N}$	$\sim 1.8 \times 10^{-7}\, N_0^2/N_{\text{amb}}^2$
Detachment[c]	$\tau_{\text{det}} \approx \dfrac{1}{k_{\text{R17}}n_{N_2}} \dfrac{n_e}{n_{O^-}}$	$\sim 5.3 \times 10^{-8}\, N_0/N_{\text{amb}}$
VT relaxation[d]	$\tau_{\text{VT}} \approx \dfrac{1}{k_O^{\text{VT}}n_O + k_{N_2}^{\text{VT}}N}$	$\sim 6 \times 10^{-2}\, N_0/N_{\text{amb}}$
VV relaxation	$\tau_{\text{VV}} = \dfrac{1}{k_{N_2}^{\text{VT}}n_{N_2}}$	$\sim 2 \times 10^{-6}\, N_0/N_{\text{amb}}$
Pressure leveling	$\tau_c \approx \dfrac{r_c}{c_s}$	$\sim 8.7 \times 10^{-7}\, N_0/N_{\text{amb}}$
Ambipolar diffusion	$\tau_{D_a} \approx \dfrac{r_c^2}{4D_a}$	$\sim 3.8 \times 10^{-5}\, N_0/N_{\text{amb}}$
Heat conduction	$\tau_{\kappa_T} \approx \dfrac{Nk_{\text{B}}r_c^2}{4(\gamma-1)\kappa_{\text{T}}}$	$\sim 7 \times 10^{-4}\, N_0/N_{\text{amb}}$
Air heating[e]	$\tau_{\text{h}} \approx \dfrac{Nk_{\text{B}}\Delta T}{(\gamma-1)\eta_{\text{T}}\sigma_e E^2}$	$\sim 3.2 \times 10^{-7}\, N_0^2/N_{\text{amb}}^2$

[a]Adapted from *Raizer* [1991, Table 9.1].

[b]Quantitative estimates are made assuming $EN_0/N_{\text{amb}} = 23$ kV/cm and $T = T_0 = 300$ K.

[c]Estimated assuming $n_{O^-} \approx n_e$.

[d]Estimated assuming $n_O \approx 10^{-3}\, n_{O_2}$. Note that VT relaxation due to collision with molecules is very slow, $1/k_{N_2}^{\text{VT}}N \approx 4.8$ s.

[e]Simple analytical estimate assuming $\Delta T \approx T_0$ and $\eta_{\text{T}} \approx 10\%$. Assuming $\Delta T = 2000$ K, one would get $\tau_{\text{h}} \approx 2\ \mu$s, at ground level.

"electric field channel" (in Figure 7), while the latter mainly by the "temperature channel". This is why the streamer-to-leader transition time scale τ_{h} is restricted by the condition of air heating. The above discussion is better illustrated by Figure 13. Figure 13a shows the qualitative picture of a stable system around its equilibrium point, where an increase in electron density Δn_e leads to $S_e < 0$ and, consequently, drives the system back to equilibrium. Figure 13b depicts the behavior of an unstable system, as in the case of streamer-to-spark transition, for constant applied electric field, discussed in Section 3.1. An increase in electron density Δn_e that leads to $S_e > 0$ drives the system into an irreversible state, where electron density increases indefinitely. This is possible in the cases studied in Section 3.1 because the electric field E is kept constant (and it is reasonably high). Figure 13c best describes the behavior of the streamer-to-leader transition, where during the instability development the electric field decreases. After the development of the TI instability, $S_e(T)$ is independent of E. In the hot channel, electron production is due to associative ionizations between N and O atoms (reaction R5) and $S_e(T)$ is also independent of n_e.

[55] The streamer-to-leader transition time scale τ_{h} can be physically interpreted as the minimum time that a streamer corona, emanating from an electrode, has to persist to promote the ignition of a leader discharge. In the case of a developed leader, τ_{h} is the time scale on which the leader increases in length by an amount Δl_s. The size of Δl_s is dictated by the dynamics of the streamer zone [*Bazelyan and Raizer*, 2000, Section 2.3.4; *Bazelyan et al.*, 2007a]. Streamers are produced in the high electric field region around
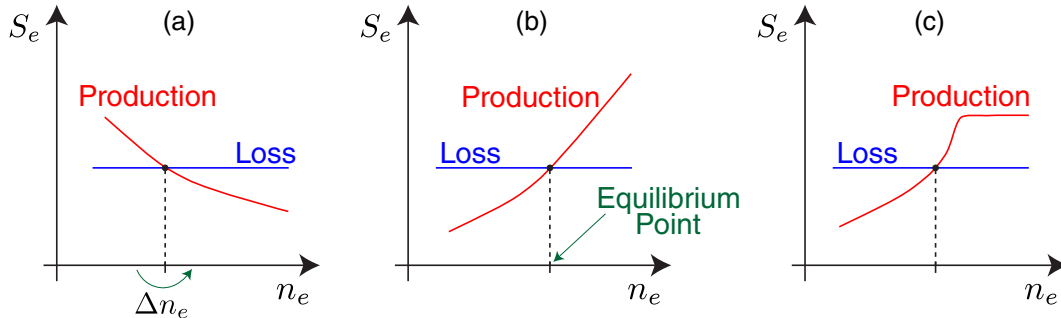

Figure 13. Qualitative behavior of (near-equilibrium) electron production and loss rates in (a) stable and (b) unstable systems. (c) Qualitative behavior of the streamer-to-leader transition development. The vertical axis represents the components of S_e, where production exceeding losses is equivalent to $S_e > 0$. Adapted from *Raizer* [1991, Figure 9.1].
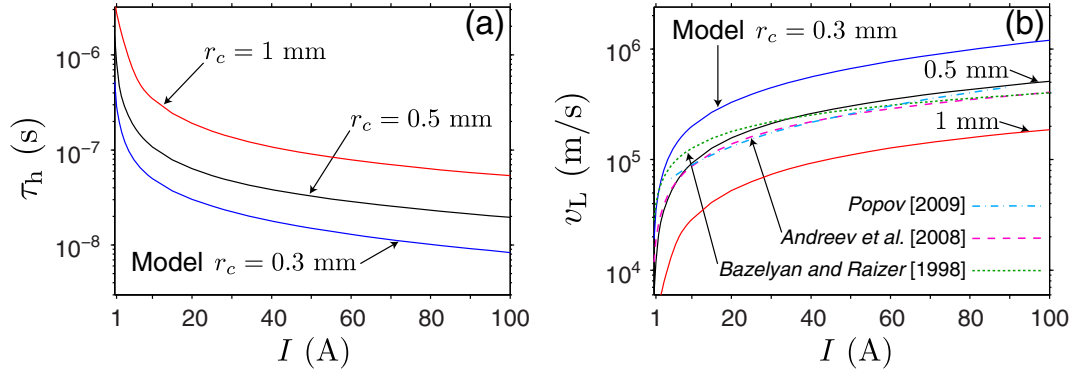
Figure 14. Dependence of (a) streamer-to-leader transition time scale τ_h and (b) leader speed v_L on electric current I at ambient ground pressure. Model results are shown for an initial radius $r_c = 0.3$, 0.5, and 1 mm. Figure 14b also shows leader speed calculations by *Popov* [2009, Figure 9] and empirical relationships provided by *Bazelyan and Raizer* [1998, p. 213] and *Andreev et al.* [2008].

the leader tip at a frequency of $\sim 10^9$ s^{-1}, for $I \sim 1$ A. The streamers follow the configuration of the electric field lines, and therefore, the macroscopical appearance of the streamer zone resembles the bottom part of a broom, as sketched in Figure 1a. Electron losses in the streamer zone are dictated by three-body attachment, and therefore, the length of the conducting section behind the streamer tips can be estimated as $\Delta l_s = v_s \tau_{a3}$, where v_s is the streamer velocity and τ_{a3} is the three-body attachment time scale. At ground pressure $\tau_{a3} \simeq 10^{-7}$ s and for a streamer speed $v_s \simeq 10^5$ m/s (typical of young weak streamers in the streamer zone), it gives $\Delta l_s \simeq$ 1 cm [*Bazelyan et al.*, 2007a]. This size of Δl_s is comparable with the measured radius of the leader head in laboratory discharges at ground pressure. Therefore, one can suppose that the leader head that is clearly visible on photographs is a collection of initial, still conducting, closely located streamer segments [*Bazelyan et al.*, 2007a]. Thus, the leader propagation speed can be estimated as [*Bazelyan and Raizer*, 2000, equation (2.38)]:

$$v_L = \frac{\Delta l_s}{\tau_h}. \quad (19)$$

The above definition of leader speed has straightforward interpretation in the case of positive leaders (Figure 1a) because they propagate continuously, with the streamer-to-leader transition process occurring in the leader head. On the other hand, the dynamics of a negative leader is more complex. Negative leaders present a characteristic stepped propagation [see, e.g., *Gallimberti et al.*, 2002, Figure 4]. Despite the different dynamical features, we assume that the streamer-to-leader transition (i.e., air heating) is the fundamental process that defines leader propagation in both cases. In case of negative leader, this process occurs during the growth of a space leader ahead of the main leader channel. The growth of the space leader is the slowest process in the sequence of relatively fast events accompanying development of a stepped leader [e.g., *Bazelyan and Raizer*, 2000, Section 4.6], and we assume that in time average sense, the heating of the space leader is the main process defining speed with which negative leader advances in space [*da Silva and Pasko*, 2012, 2013]. In the present work we do not discuss details of polarity-dependent features of leaders, and we focus on the leader speed estimated from formula (19). For instance, Figure 14 presents the calculated dependence of (a)
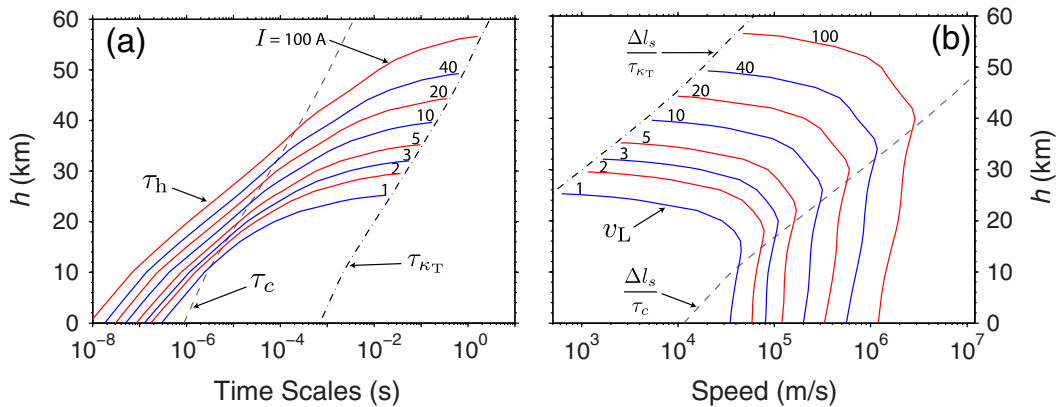

Figure 15. Scaling of (a) streamer-to-leader transition time and (b) leader speed with altitude, for several different currents. Figure 15a displays τ_h, as well as, the ambient values of τ_c and τ_{κ_T} to illustrate the discussion. Figure 15b displays the calculated leader speed with formula (19) and τ_c and τ_{κ_T} plotted in units of speed (i.e., $\Delta l_s/\tau_c$ and $\Delta l_s/\tau_{\kappa_T}$).
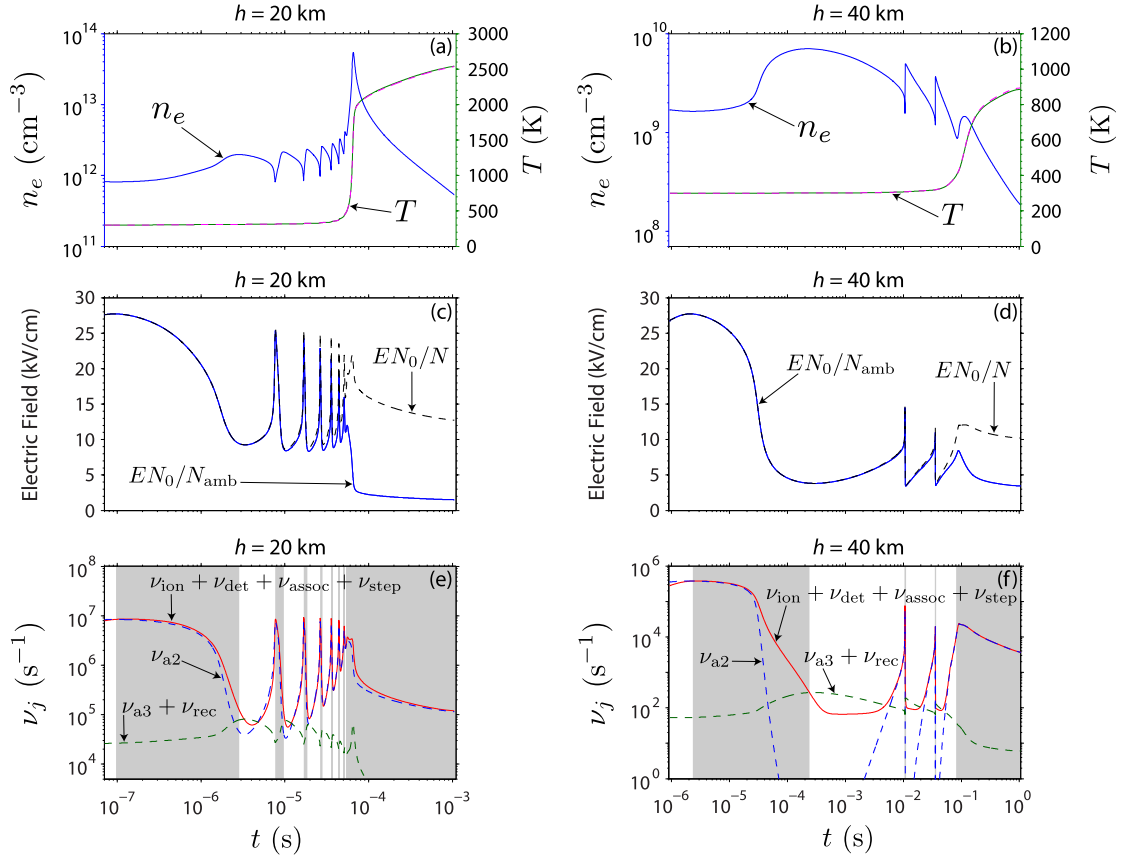
Figure 16. Temporal dynamics of (a,b) electron density and temperature, (c,d) electric field, and (e,f) rates of electron production, for $I = 1$ A, at two different altitudes (a,c,e) 20 km and (b,d,f) 40 km. Figures 16c and 16d show the electric field in equivalent value at ground pressure EN_0/N_{amb} and the reduced electric field accounting for the lowering of neutral density EN_0/N. Shaded areas in Figures 16e and 16f mark the time range at which electron production is higher than losses (i.e., $S_e > 0$).

τ_{h} and (b) v_{L} on electric current, for range of values $I = 1$–100 A, at ambient ground pressure. The figure shows calculations for our reference case with $r_c = 0.3$ mm, as well as, for two additional cases with $r_c = 0.5$ and 1 mm. The lower range of displayed speeds $v_{\mathrm{L}} = 10^4$–10^5 m/s is characteristic of laboratory discharges [e.g., *Bazelyan et al.*, 2007a], while the upper range $v_{\mathrm{L}} = 10^5$–10^6 m/s is characteristic of lightning [e.g., *Saba et al.*, 2008].

[56] Figure 14b also shows calculations by *Popov* [2009, Figure 9] and empirical relationships provided by *Bazelyan and Raizer* [1998, p. 213] and *Andreev et al.* [2008]. Initial conditions used by *Popov* [2009] are similar to our reference case. Empirical relationships have the power law form $v_{\mathrm{L}} = \alpha_v I^{\beta}$, where *Bazelyan and Raizer* [1998, p. 213] give $\alpha_v = 4 \times 10^4$ m/s·A$^{\beta}$ and $\beta = 0.5$, and *Andreev et al.* [2008] give $\alpha_v = 1.88 \times 10^4$ m/s·A$^{\beta}$ and $\beta = 0.67$. Note that both empirical formulas were obtained by fitting experimental data in a narrower range of currents than the ones displayed in Figure 14b. Nonetheless, we have extrapolated the empirical results for the whole range $I = 1$–100 A to show that calculations and measurements follow the same trend for $v_{\mathrm{L}}(I)$ [see also *Popov*, 2009, and references therein]. Figure 14b shows that our model best approaches previous works when the initial radius for the leader stem, at ground pressure, is approximated by $r_c = 0.5$ mm.

4.2. Scaling of Streamer-to-Leader Transition Time and Leader Speed With Altitude

[57] In this section, we discuss the scaling of streamer-to-leader transition, under conditions of constant leader current, with ambient air density N_{amb} or altitude h in Earth's atmosphere. Figure 15 presents the calculated values of (a) the streamer-to-leader transition time scale τ_{h}, defined in Section 4.1 as the time to heat channel up to 2000 K, and (b) the calculated leader speed, using equation (19). To estimate leader speeds at reduced air densities, we assume that $\Delta l_s = \Delta l_{s,0} N_0^2 / N_{\mathrm{amb}}^2$, where $\Delta l_{s,0} = 1$ cm. We assume the scaling $\Delta l_s \propto 1/N_{\mathrm{amb}}^2$ because Δl_s is governed by the three-body attachment time scale, which has a $\propto 1/N^2$ dependence on air density (see Table 4) [*da Silva and Pasko*, 2012, 2013]. We note that three-body attachment is a very inefficient plasma decay process at mesospheric altitudes (where $N_{\mathrm{amb}} \ll N_0$). Hence, the assumption that the streamer channel lifetime is dictated by τ_{a3} (reaction R9) is not correct in the context of sprite discharges. At sprite altitudes, two-body dissociative attachment (reaction R8) can be a more efficient mechanism of electron loss in streamer channels. In this case, Δl_s would be restricted by τ_{a2}, rather than τ_{a3}. However, the concept of $\Delta l_s \propto \tau_{a3}$ is only used in this work to estimate leader speeds below $\sim$60 km altitude, as shown in Figure 15. Comparing the rates of reactions R8 and R9, one can see that in the alti-
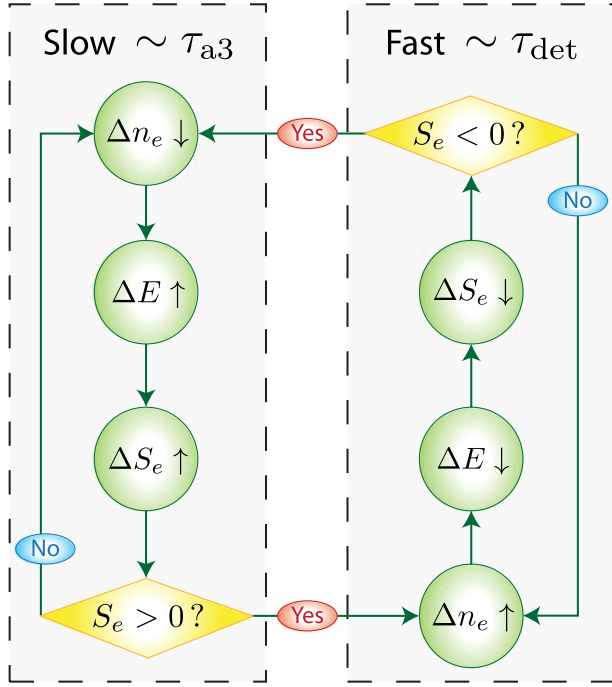
Figure 17. Schematic representation of the closed chain of events occurring during the passage of a low electric current through air in conditions of low air density N_{amb}, such as shown in Figure 16. Similarly to Figure 7, upward/downward directed arrows represent an increase/decrease in a quantity.

tude range shown in Figure 15, $\tau_{a3} < \tau_{a2}$ for electric fields below $\sim 6\, N_{amb}/N_0$ kV/cm. Since the average electric field in the streamer zone of a positive leader is $\sim 5\, N_{amb}/N_0$ kV/cm [*Bazelyan and Raizer*, 2000, p. 69], the assumption that $\Delta l_s \propto \tau_{a3}$ is justified. More accurately, the length scale of the leader tip is determined by the simultaneous action of several processes and its evaluation is more complex than the one presented here. In the present work, the value of Δl_s is taken as an external parameter [*Bazelyan et al.*, 2007a] and the analysis is focused on the influence of τ_h on the leader speed.

[58] Besides the streamer-to-leader transition time scale τ_h, for illustrative purposes, Figure 15a also shows the gas dynamics time scale τ_c and the heat conduction time scale τ_{κ_T}. Additionally, Figure 15b also presents both time scales plotted in units of speed (i.e., $\Delta l_s/\tau_c$ and $\Delta l_s/\tau_{\kappa_T}$). Note that both time scales increase with altitude inversely proportionally to the decrease in ambient neutral density, as shown in Table 4. We can see from Figure 15 that at near-ground pressures (lower altitudes), air heating time τ_h scales very close to $\propto 1/N_{amb}^2$. This assertion is more evident in Figure 15b where, since both Δl_s and τ_h scale with altitude as $\propto 1/N_{amb}^2$, estimated velocities are almost independent of altitude, in the regime $\tau_h < \tau_c$ (a perfect scaling $\tau_h \propto 1/N_{amb}^2$ would result in vertical lines in Figure 15b). Note, in Figure 15b, the strong deviation of the velocity behavior for $v_L < \Delta l_s/\tau_c$. Moreover, we found that transition cannot occur for $\tau_h > \tau_{\kappa_T}$. The reason for such constraint is discussed below.

[59] As demonstrated in previous section, an increase in air temperature ΔT is the required condition to drive the system to the TI instability (Figure 7). Neglecting effects of radial dynamics, equation (3) can be written as $N k_B \Delta T/\tau_h \sim (\gamma - 1)\eta_T \sigma_e E^2$. If we assume that all quantities scale with ambient air density following similarity laws for streamer discharges, i.e., σ_e and E scale proportionally to N [*Pasko*, 2006, pp. 265–267], we can predict the air heating time at different altitudes to be $\tau_h = \tau_{h,0} N_0^2/N_{amb}^2$, as shown in Table 4 [see also *Bazelyan and Raizer*, 2000, equation (2.37); *Riousset et al.*, 2010b, equations (1) and (2)]. Although this analysis is approximate, it can explain the scaling of the streamer-to-leader transition time at near-ground pressures, shown in Figure 15a. The scaling $\tau_h \propto 1/N_{amb}^2$ is very strong, it introduces a multiplying factor of $N_0^2/N_{amb}^2 \sim 200$ at 20 km altitude and of $\sim 10^5$ at 40 km (see Figure 1b). At low pressures where the required heating time is very long, the Joule heating term in equation (3) is balanced by radial spreading of energy due to advection and heat conduction, and therefore, air heating can be expected to be slower than the above prediction (i.e., $\tau_h > \tau_{h,0} N_0^2/N_{amb}^2$). Thus, when $\tau_h > \tau_c$ transition is delayed because the energy introduced in the system (Joule heating) is radially distributed by advection on a shorter time scale. Similarly, when $\tau_h > \tau_{\kappa_T}$ the channel cannot experience contraction, and therefore, streamer-to-leader transition cannot occur.

[60] The strong lengthening of the streamer-to-leader transition time at upper altitudes in the Earth's atmosphere introduces some peculiarities, when compared to its behavior at ambient ground pressure. In fact, the instability factor (air heating) is very slow. The system stays in an equilibrium state (Figure 13a) for a long time. Figure 16 shows the temporal dynamics of (a,b) electron density and temperature, (c,d) electric field, and (e,f) rates of electron production, at two different altitudes (a,c,e) 20 km and (b,d,f) 40 km. Simulations in Figure 16 were performed for $I = 1$ A, an electric current value that leads to streamer-to-leader transition at $h \leq 25$ km. Comparing Figures 16a and 16b, we can see a sharp increase in both temperature and electron density (characteristic of the TI instability) occurring only for $h = 20$ km. A pronounced feature of the results shown in Figure 16 is the presence of oscillations in electron density, electric field, and kinetic rates of electron production. The reasons are very similar to those presented in previous section. The oscillations are consequence of the relationship $E \propto 1/n_e$, introduced by equation (10). Figure 17 qualitatively describes the behavior of a near-equilibrium system under the restriction of a constant electric current not producing significant air heating, such as shown in Figure 16. For the initial value of electric field ($E_{amb} < E_k$), electron density decreases because of field induced attachment. The decrease of n_e leads to an increase in E (equation (10)), and, eventually, production overcomes loss. When $S_e > 0$, electron density increases, electric field decreases, and losses become dominant again. This sequence of events introduces the oscillations seen in Figure 16. The electric field is "trapped" between two equilibrium points (such as in Figure 13a): an upper value of electric field, where $v_{det} + v_{ion} > v_{a2}$, and a lower value of electric field, where $v_{a3} > v_{det}$ (Figures 16e and 16f). The system crosses the higher equilibrium point because of detachment and the lower equilibrium point because of three-body attachment. Detachment
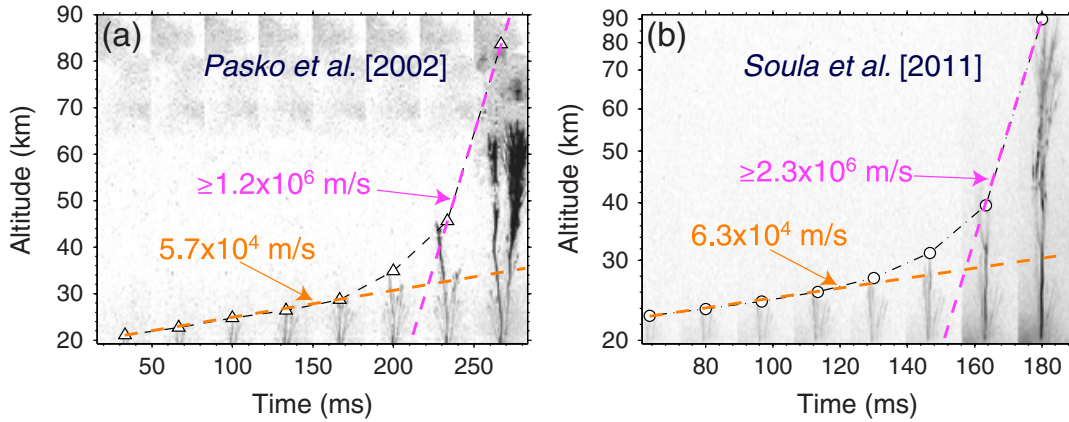
Figure 18. Gigantic Jets observed by (a) *Pasko et al.* [2002] and (b) *Soula et al.* [2011] (images in Figure 18b are courtesy of Serge Soula). Symbols show estimated top altitudes. Time reference is arbitrary, and it is the same as used in subsequent figures. The sequence of images for *Pasko et al.*'s [2002] jet is spaced in time by 33 ms, while for *Soula et al.*'s [2011] jet by 16.7 ms. Figures also show estimated speeds during initial and final stages of the upward propagation of both GJs. Reprinted by permission from Nature Publishing Group and American Geophysical Union [*da Silva and Pasko*, 2012, Figure 1].

is much faster than three-body attachment (see Table 4). Owing the fact that $\tau_{a3} \gg \tau_{det}$, we can see from Figures 16c and 16d that the valleys are longer than the peaks (except for the last peak that occurs at reasonably high T and low N). The lower bound for the electric field is approximately set by the condition $\nu_{a2} = \nu_{a3}$. Since $\nu_{a2} \propto N$ and $\nu_{a3} \propto N^2$, the average value of the reduced electric field E/N is lower and lower at reduced air densities, hindering even more the air heating process.

[61] The point that we would like to emphasize in this section is that the disequilibration factor, the air heating, which drives the system from the near-equilibrium state, sketched in Figure 17, to the unstable state, sketched in Figure 7, is slower and slower at reduced air densities. The quantitative model results presented in this paper can be interpreted from a qualitative standpoint, by a simple analysis of the air density scaling of the key processes involved. In other words, a simple look to the different scalings of the air heating and heat conduction time (i.e., $\tau_h \propto 1/N_{amb}^2$ and $\tau_{\kappa_T} \propto 1/N_{amb}$) indicates that there is an altitude on Earth's atmosphere where τ_h is longer than τ_{κ_T}, and therefore, streamer-to-leader transition cannot occur. The quantitative values for the maximum altitude where a leader can be formed are marked by the end of solid lines in Figure 15 and they depend on I and r_c.

[62] Figures 16a and 16b show the simulated evolution of temperature using the different values for the thermal conductivity, as defined in Section 2.1, κ_T^* (solid line) and κ_T^{**} (dashed line). Calculations using the latter lead to a final temperature which is a few degrees higher than when using the former, and therefore, the difference is practically imperceptible from the figures. We have performed several tests, varying I and h in the range shown in Figure 15. The results show that the only difference obtained when using κ_T^{**} instead of κ_T^* is that the stationary temperature is from tens up to hundreds of degrees higher when using κ_T^{**}. Moreover, the calculated values of τ_h are not affected by the choice of the thermal conductivity description because $\kappa_T^{**} \simeq \kappa_T^*$ for $T < 2000$ K. In the analysis presented in Figure 15, τ_h is com-

pared to τ_{κ_T}, which is obtained from the ambient value of the thermal conductivity and, therefore, is also independent of the choice between κ_T^* and κ_T^{**}.

[63] Although further investigation is necessary, one can speculate that the oscillations in electric field shown in Figure 16 can be mapped into optical emissions. Thus, the mechanism sketched in Figure 17 may be in part responsible for the flickering of small structures observed in gigantic jets [see, e.g., *Soula et al.*, 2011].

[64] Despite the fact that air heating is slower at reduced air densities, a current as low as 1 A can promote significant air heating to enhance the NO production. This possibility was not considered by *Mishin* [1997] when evaluating the effects of blue jets in the ozone layer. Note that lightning is known to be the main source of nonanthropogenic NO_x production [e.g., *Brasseur et al.*, 1996, Table 2] in the atmosphere. Nitrogen oxide participates in catalytic cycles of ozone destruction, and therefore, the effects of gigantic jet leaders on the ozone layer are an important topic requiring further investigation.

5. On the Upward Propagation of Gigantic Jet Leaders

[65] Gigantic jets (GJs) are upward directed large-scale electrical discharges that are observed to leave thundercloud tops and propagate up to ~90 km altitude, connecting to the lower ionosphere [*Pasko et al.*, 2002; *Su et al.*, 2003]. Figure 18 shows two examples of GJs observed by *Pasko et al.* [2002] and *Soula et al.* [2011]. As suggested by *van der Velde et al.* [2010], we have reestimated the distance between the observation site and the most probable location of *Pasko et al.*'s [2002] jet to be 235±20 km, which implies a correction of ~18% in the estimated altitudes, positioning the jet's top at 83.7±7 km altitude [*da Silva and Pasko*, 2012]. The corrected altitudes are shown in Figures 18a. The altitude range of *Soula et al.* [2011] jet was estimated from their Figure 7a. *Soula et al.*'s [2011] jet was observed at 53 km range. The fact that the jet's top is seen at larger dis-
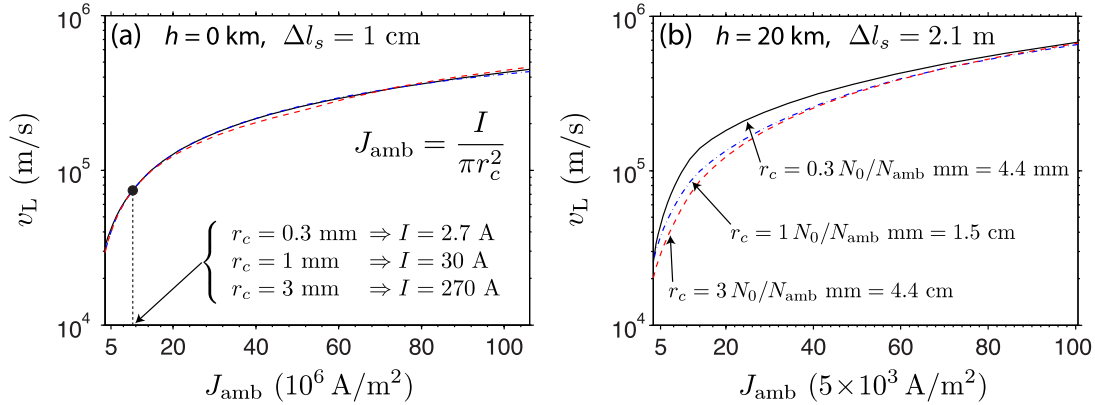
Figure 19. Simulated leader speed as a function of initial current density in the leader stem at (a) ground and (b) 20 km altitude, for different values of stem radius [*da Silva and Pasko*, 2013, Figures 2a and 2b].

tances than the bottom introduces the nonuniform altitude scale seen in Figure 18b. This correction is not necessary for *Pasko et al.*'s [2002] jet because it was observed at a much greater distance. The term "gigantic jet" was introduced by *Su et al.* [2003]. These authors have observed five GJs emerging from an oceanic thunderstorm near the Philippines and reaching altitudes ∼86–91 km. *Su et al.* [2003] pointed out the existence of three phenomenologically distinct stages in the observed GJs: the *leading jet* stage corresponding to the upward propagation, the *fully developed jet* stage with persistent luminosity after the connection with the ionosphere, and the *trailing jet* corresponding to the lower part of the GJ that decays slower than other portions.

[66] In recent years, the number of ground-based [*van der Velde et al.*, 2007, 2010; *Cummer et al.*, 2009; *Soula et al.*, 2011; *Lu et al.*, 2011; *Chou et al.*, 2011] and satellite-based [*Kuo et al.*, 2009; *Chou et al.*, 2010] observations of GJs has increased considerably. The current theoretical understanding of the GJ process describes it as an upward directed discharge, analogous to cloud-to-ground lightning [*Krehbiel et al.*, 2008]. GJs are initiated between adjacent charge regions (similarly to intracloud lightning discharges) by a bidirectional leader discharge. *Krehbiel et al.* [2008] demonstrated that when charge regions in the thunderstorm were not balanced (meaning the upper positive charge center contains less net charge than the midlevel negative charge center), the leader potential could be significantly shifted in the direction defined by the charge with dominant magnitude. In this situation the propagation of the leader becomes essentially independent from the weaker charge center, allowing it to penetrate through the weaker upper charge center and to escape from the thundercloud upward and serve as the initiation of a GJ [*Krehbiel et al.*, 2008]. Complementarily, *Raizer et al.* [2006, 2007, 2010] point out that as the leader propagates upward, the streamer zone ahead of it becomes longer because of the dynamics of streamer growth in a medium with exponentially decreasing air density. Therefore, there is an altitude where the streamer corona in the leader head can "escape" to the ionosphere. Below, we apply the leader speeds calculated in this paper to the analysis of the GJ development (the leading jet phase). We present a simple time dynamic model for the description of GJ propagation, and finally, we explain the vertical structuring of GJs by combining results of our time dynamic

model with the ideas introduced by *Raizer et al.* [2006] and *Krehbiel et al.* [2008].

5.1. Effective Dependence of Leader Speed on Current Density

[67] In previous sections, we have assumed that the initial radial distribution of the electron density $n_e = n_{e,a} \exp(-r^2/r_c^2)$ in the leader stem resembles a single streamer channel, with $n_{e,a} = 2 \times 10^{14} N_{amb}^2/N_0^2$ cm^{-3} and $r_c = 0.3 N_0/N_{amb}$ mm. Using the above mentioned value for r_c, we obtained a dependence $v_L(I)$, at ambient ground pressure, as shown in Figure 14b. We also extended this approach for calculation of leader speeds at reduced air densities, as shown in Figure 15b. The parameterization of leader speed with respect to the electrical current I flowing through the channel is a common approach used in the literature [e.g., *Popov*, 2009] because channel base current is a parameter easily obtainable from experiments [e.g., *Andreev et al.*, 2008]. However, from a physical standpoint, the leader speed should be more generally defined as a function of the current density J rather than the total current I (because $\partial T/\partial t \propto \vec{J} \cdot \vec{E}$). Figures 19a and 19b present simulated leader speed as a function of the initial current density in the leader stem J_{amb}, at ground and 20 km altitude, respectively. We note that current density scales with air density as $\propto N^2$ and the range of current values shown in Figure 19a and 19b is different by a factor of 200, approximately reflecting this scaling. We can see a similar dependence on $J_{amb} = I/\pi r_c^2$ for both altitudes and for a 1 order of magnitude range of change in r_c. We can also see that the same leader speed can be obtained with 2 orders of magnitude difference in I. The value $r_c = 0.3$ mm has been proven to reproduce well laboratory leaders, which are generated in meter long gaps, under potential differences of hundreds of kilovolts to a few megavolts [e.g., *Popov*, 2009]. Under these conditions, the leader has $I \sim 1$ A and $v_L \sim 10^4$ m/s [*Bazelyan and Raizer*, 2000, p. 67]. However, in the formation of a leader in open air with available thundercloud potential the initial radius for the stem might be significantly larger due to various reasons, as for example, streamer expansion and overlapping.

[68] The main implication of a larger r_c on the scaling of leader speed with ambient air density comes from the fact that $\tau_c \propto r_c$ and $\tau_{\kappa_T} \propto r_c^2$. Because the energy dissipa-
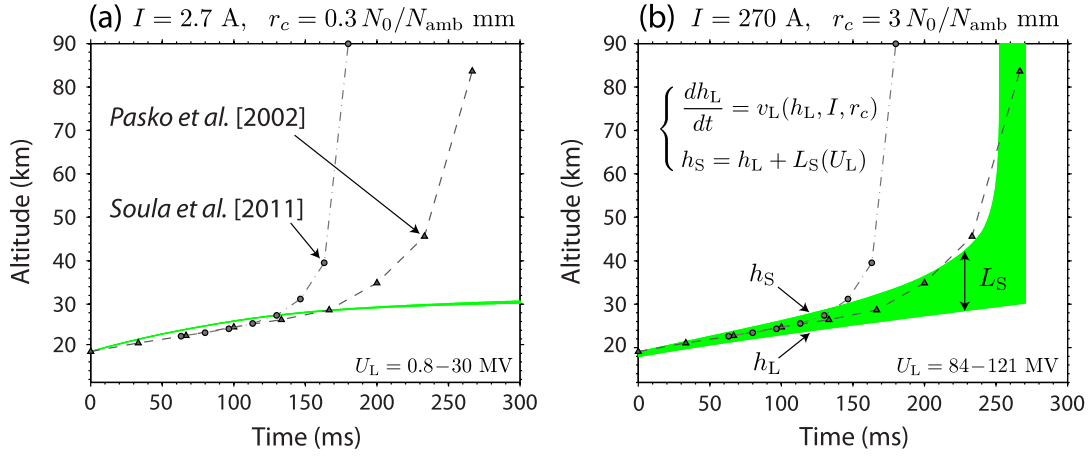
Figure 20. Comparison of observed GJ propagation with modeled upward leader propagation for $J_{amb} = 9.6 \times 10^6 \, N^2/N_0^2$ A/m^2, including expansion of streamer zone, for two different values of stem radius (a) 0.3 mm and (b) 3 mm [*da Silva and Pasko*, 2013, Figures 2c and 2d].

tion time scales τ_c and τ_{κ_T} increase with increasing r_c, the regimes $\tau_h > \tau_c$ and $\tau_h > \tau_{\kappa_T}$ (discussed in Section 4.2) occur at higher altitudes in Earth's atmosphere, for a fixed value of current density $J_{amb} N_0^2/N_{amb}^2$. As a consequence, the scalings $\tau_h \propto 1/N_{amb}^2$ and $v_L \approx$ const are valid for a wider range of pressures. In contrast to streamer radius that can change by more than 1 order of magnitude at a given ambient pressure [e.g., *Briels et al.*, 2006, 2008], the electron density in the streamer body has an approximately constant value $\sim 10^{14} N_{amb}^2/N_0^2$ cm^{-3}, and therefore, it does not affect the obtained values for leader speeds [see also *Popov*, 2009].

5.2. Gigantic Jet Acceleration as Evidence of Its Vertical Structuring

[69] As proposed by *Krehbiel et al.* [2008], gigantic jets (GJs) are initiated inside the thundercloud as intracloud lightning discharges and owing to a charge imbalance (meaning the upper charge center is depleted with respect to the midlevel center), one or more leaders can escape upward to form a GJ. One observational feature that supports the aforementioned mechanism is that GJs emerge from thundercloud tops with speeds on the order of or less than the lower limit of streamer speeds, which is $\sim 10^5$ m/s [*Bazelyan and Raizer*, 2000, p. 39] but consistent with speeds of laboratory and lightning leaders [*Bazelyan and Raizer*, 1998, Section 6.2]. For instance, *Briels et al.* [2008] have measured laboratory streamer speeds in the range $1-40 \times 10^5$ m/s, while *Andreev et al.* [2008] and *Saba et al.* [2008] have measured speeds in the range $1-5 \times 10^4$ m/s and $3-60 \times 10^4$ m/s, for laboratory and lightning leaders, respectively. Modeling results of leader speeds at reduced air densities reiterate this assertion [*da Silva and Pasko*, 2012, 2013]. As can be seen from Figure 19, the initial speeds of GJs $\lesssim 10^5$ m/s [*da Silva and Pasko*, 2012, Figure 3a] are compatible to a current density of $\lesssim 10^7 N_{amb}^2/N_0^2$ A/m^2 in the leader stem [*da Silva and Pasko*, 2013].

[70] Complementarily, *Raizer et al.* [2006, 2007] point out that as the GJ leader propagates upward, the streamer zone ahead of it becomes longer and longer because of the dynamics of streamer growth in a medium with exponentially decreasing air density. Theory of leader discharges predicts the existence of an average constant electric field in the streamer zone equal to the critical electric field value for stable streamer propagation E_{cr} [*Bazelyan and Raizer*, 2000, pp. 67–69]. For positive leader, for example, at ambient ground pressure this value is $E_{cr,0} \simeq 5$ kV/cm [*Bazelyan and Raizer*, 2000, p. 69]. The average electric field in a leader streamer zone is expected to reduce exponentially with altitude proportionally to air density, i.e., $E_{cr} = E_{cr,0} N_{amb}/N_0$ [e.g., *Pasko*, 2006, p. 266] (N_{amb} can be approximately defined by the analytical expression $N_{amb}(h) = N_0 e^{-h/h_N}$, with $h_N = 7.2$ km and $N_0 = 2.5 \times 10^{19}$ cm^{-3}). As first noticed by *Raizer et al.* [2006], this fact has important consequences for an upward propagating leader, such as in the case of GJs escaping from thundercloud tops. A simple estimate for the streamer zone length L_S of an upward propagating leader can be obtained analytically for a simple geometry [*da Silva and Pasko*, 2013, Figure 1]. The length L_S is related to the potential drop in the streamer zone U_S and the altitude position of the leader head h_L as:

$$L_S = h_N \ln \left[\left(1 - \frac{U_S}{h_N E_{cr,L}} \right)^{-1} \right], \qquad (20)$$

where $E_{cr,L} = E_{cr,0} \exp(-h_L/h_N)$ [*da Silva and Pasko*, 2013, Section 3]. Equation (20) is obtained by solving the equation for the potential drop across the streamer zone, $U_S = \int_{h_L}^{h_L + L_S} E_{cr}(h) \, dh$, for L_S. If the leader is close to ground ($h_L \ll h_N$), such as in leaders initiated from tall buildings [e.g., *Lalande et al.*, 2002, Figures 1 and 2], half of leader voltage drop U_L occurs in the streamer zone, i.e., $U_S = U_L/2$, and formula (20) reduces to $L_S = U_L/2E_{cr,L}$ [*Bazelyan and Raizer*, 2000, p. 69]. The length of the streamer zone increases exponentially with altitude, i.e., $L_S \propto \exp(h_L/h_N)$ [*da Silva and Pasko*, 2013, Figure 3a]. For an upward directed leader at mesospheric altitudes, such as in GJs (Figure 18), the potential drop in the streamer zone shifts from $U_L/2$ to U_L [*da Silva and Pasko*, 2013, Figure 3c]. It can be seen from equation (20) that $L_S \to \infty$ when $U_L = h_N E_{cr,L}$. Consequently, there is an altitude $h_{jump} = h_N \ln(h_N E_{cr,0}/U_L)$ at which the streamer zone "jumps" to the ionosphere [*da Silva and Pasko*, 2013, Figure 3d].

[71] Despite the fact that air heating is slower and slower at higher altitudes in Earth's atmosphere (Figure 15), GJs

are observed to accelerate as they propagate upward (see, for example, Figure 18). Figure 20 presents the upward propagation as a function of time of the two GJs shown in Figure 18. In view of the discussion in Section 5.1, experimental data are compared to simulations performed for the same initial current density in the leader stem but for two different values of the initial stem radius: (a) $r_c = 0.3\,N_0/N_{amb}$ mm and (b) $3\,N_0/N_{amb}$ mm. Shaded areas in Figure 20 show the simulated propagation of an upward leader $h_L(t)$ with an expanding streamer zone $h_S(t) = h_L(t) + L_S(U_L)$ [da Silva and Pasko, 2013]. Leader speed $v_L = dh_L/dt$ is approximately the same in both cases, however, in Figure 20b, I, U_L, and consequently, L_S are larger (see discussion by da Silva and Pasko [2013] for details). The figure demonstrates that the combined effects of a leader propagating with a steady speed of $\lesssim 10^5$ m/s and the expansion of its streamer zone according to equation (20) are capable of explaining the observed acceleration in GJs. Thus, the jump altitude can be used as a simple estimate for the transition between leader and streamer portions of GJs during the leading jet phase [Su et al., 2003]. After the connection to the ionosphere, GJs exhibit a return stroke-like process [Kuo et al., 2009, Figure 5]. Owing the high electrical current, ~ 1 kA, flowing through the channel [Cummer et al., 2009, Figure 3], the leader portion may reach higher altitudes. However, a leader cannot bridge the gap between the cloud and the ionosphere because streamer-to-leader transition is prevented at very low air densities (Figure 15). The longer persistency of the GJ trunk (referred as trailing jet [Su et al., 2003]) with respect of other portions is the evidence of air heating within this part of channel (see discussion by Neubert et al. [2011]). In heated air, electron losses due to attachment to oxygen molecules are strongly reduced (see, e.g., Figures 11d, 16e, and 16f).

6. Summary and Conclusions

[72] In this paper we have presented an air heating model capable of capturing the effects of a sustained electrical current flowing through the body of a streamer in a wide range of ambient pressures. Some of the key features of the model are the detailed description of the fast heating mechanism and the rigorous treatment of the vibration-dissociation-vibration coupling. The model was validated through calculation of breakdown times of short air gaps and comparison to available experimental data. The streamer-to-spark transition time, for the case of constant electric field across the gap, scales with ambient air density very close to $\propto 1/N_{amb}$, as evidenced from experiments and numerical simulations. This dependence is a consequence of the decisive role of electron detachment in the streamer-to-spark transition; time scale for electron detachment from oxygen atoms increases with reduced air density as $\propto 1/N_{amb}$. Detachment compensates the rate of electron loss in the streamer body and, eventually, is responsible for a change in sign in the electron balance equation, triggering the development of a thermal-ionizational (TI) instability. The constant electric field simulations were also used to study the fast heating mechanism (responsible for air heating on short time scales $\lesssim 100$ ns at ambient ground pressure). We pointed out that the main channels for rapid heating are quenching of $O(^1D)$ and $N_2(B)$ states and electron-impact dissociation of air com-

ponents. We also have quantified the dependence of these channels on ambient air density, showing the considerable reduction of the fast heating efficiency above the quenching altitude of the $N_2(C)$ state, which is ~ 30 km.

[73] We have applied the model to study the sequence of physical processes leading to streamer-to-leader transition, under a constant electrical current in the leader stem. The aspects of the change in air ionization mechanism from electron-impact to associative ionization was discussed in detail, as well as, the role of the channel contraction in the TI instability responsible for leader formation and propagation.

[74] We have presented a methodology to calculate leader speeds in a broad range of currents and pressures based on the fact that the leader propagation is determined by the air heating of every newly formed leader section. The study of air heating in the leader stem revealed that the streamer-to-leader transition time scales very close to $\propto 1/N_{amb}^2$ at near-ground pressures, and hence, leader speeds have weak dependence on air density. This scaling follows the similarity law for Joule heating in a streamer channel, which increases with reducing air density as $\propto 1/N_{amb}^2$. However, this scaling does not hold for very low air densities, where the rate of energy deposition is balanced by the channel expansion (and heating from quenching of excited electronic states is very inefficient), placing a limit on the maximum altitude in Earth's atmosphere where streamer-to-leader transition can occur. This altitude is a function of the leader stem characteristics, such as current and radius. We also point out that leader speed can be more generally defined as a function of the current density in the leader stem rather than total current. We would like to remark that the time scale for development of the TI instability in constant-field and constant-current setups has intrinsically different dependence on ambient air density. The former is dictated by electron detachment and scales with air density as $\propto 1/N_{amb}$, while the latter is dictated by Joule heating and scales approximately as $\propto 1/N_{amb}^2$.

[75] The calculated leader speeds were employed to discuss the dynamics of an upward propagating leader, such as in the case of gigantic jets (GJs) escaping from thundercloud tops. We have pointed out that the initial speeds of two observed GJs are compatible to simulated leader speeds with a current density $\lesssim 10^7$ A/m² (scaled to ground pressure) in the leader stem. This current density may correspond to a total current ranging from amperes to hundreds of amperes, depending on the actual leader stem radius. We pointed out that most likely the stem is initially a few millimeters wide (scaled to ground pressure). Thus, the leader would transport a current of tens to hundreds of amperes, in agreement with GJ and lightning observations. GJs are observed to accelerate as they propagate through the stratosphere and mesosphere. We have demonstrated that this acceleration is not related to the dynamics of streamer-to-leader transition at reduced air densities. The acceleration, in fact, can be associated to the lengthening of the streamer zone in an atmosphere of exponentially decreasing air density. The dynamics of streamer growth in the nonuniform atmosphere defines an altitude at which the streamer zone of an upward directed leader becomes so long that it dynamically extends (jump) to the ionosphere. This altitude may serve as a first-order reference for the transition between leader and streamer portions in GJs.

Table A1. List of Chemical Reactions

	Reactions	Rate Constant (1/s, cm³/s or cm⁶/s)	Reference
		Generation of electrons by direct ionization (ν_{ion})	
R1	$O_2 + e \rightarrow O_2^+ + e + e$	$4.9\times10^{-9}\exp(-657/(E/N))F$	*Benilov and Naidis* [2003, (2)]
R2	$N_2 + e \rightarrow N_2^+ + e + e$	$8.1\times10^{-9}\exp(-925/(E/N))F$	*Benilov and Naidis* [2003, (1)]
		Generation of electrons by stepwise ionization (ν_{step})	
R3	$NO + e \rightarrow NO^+ + e + e$	$5.0\times10^{-9}\exp(-460/(E/N))F$	*Benilov and Naidis* [2003, (3)]
R4	$O + e \rightarrow O^+ + e + e$	$4.0\times10^{-9}\exp(-713/(E/N))F$	*Benilov and Naidis* [2003, (4)]
		Generation of electrons by associative ionization (ν_{assoc})	
R5	$N + O \rightarrow NO^+ + e$	$2.5\times10^{-15}T\exp(-32000/T)$	*Aleksandrov et al.* [1997, (R7)]
R6	$N_2(A) + N_2(a') \rightarrow N_4^+ + e$	5×10^{-11}	*Kossyi et al.* [1992, (25)]
R7	$N_2(a') + N_2(a') \rightarrow N_4^+ + e$	2×10^{-10}	*Kossyi et al.* [1992, (26)]
		Loss of electrons by two-body dissociative attachment (ν_{a2})	
R8	$O_2 + e \rightarrow O^- + O$	$6.7\times10^{-13}\frac{(E/N)^{0.8}}{\exp(1.05\|5.3-\ln(E/N)\|^3)}F$	*Benilov and Naidis* [2003, (20)]
		Loss of electrons by three-body attachment (ν_{a3})	
R9	$O_2 + e + M \rightarrow O_2^- + M$	$1.4\times10^{-29}\frac{\exp[700(T_e-T)/(T_eT)]}{(T_e/300)\exp(600/T)}X_{O_2}$ $+ 1.07\times10^{-31}\frac{\exp\left[1500(T_e-T)/(T_eT)\right]}{(T_e/300)^2\exp(70/T)}X_{N_2}$ $+ 10^{-31}X_O$	*Kossyi et al.* [1992, (45), (46), (48)]
		Loss of electrons by electron-ion recombination (ν_{rec})	
R10	$O_2^+ + e \rightarrow O + O(^1D)$	$2\times10^{-7}(300/T_e)$	*Kossyi et al.* [1992, (40)]
R11	$NO^+ + e \rightarrow O + N(^2D)$	$4\times10^{-7}(300/T_e)^{1.5}$	*Kossyi et al.* [1992, (41)]
R12	$O_4^+ + e \rightarrow O_2 + O_2$	$1.4\times10^{-6}(300/T_e)^{0.5}$	*Kossyi et al.* [1992, (30)]
R13	$O_2^+N_2 + e \rightarrow O_2 + N_2$	$1.3\times10^{-6}(300/T_e)^{0.5}$	*Kossyi et al.* [1992, (34)]
R14	$O_2^+ + e + M \rightarrow O_2 + M$	$6\times10^{-27}(300/T_e)^{1.5}$	*Kossyi et al.* [1992, (44)]
		Generation of electrons by detachment (ν_{det})	
R15	$O^- + N_2 \rightarrow N_2O + e$	$1.16\times10^{-12}\frac{(E/N)^2}{(43.5)^2+(E/N)^2}$	*Luque and Gordillo-Vázquez* [2012]
R16	$O^- + O \rightarrow O_2 + e$	5×10^{-10}	*Benilov and Naidis* [2003, (23)]
R17	$O^- + N_2(A) \rightarrow O + N_2 + e$	2.2×10^{-9}	*Kossyi et al.* [1992, (64)]
R18	$O^- + O_2(a) \rightarrow O_3 + e$	3×10^{-10}	*Kossyi et al.* [1992, (62)]
R19	$O^- + NO \rightarrow NO_2 + e$	2.6×10^{-10}	*Benilov and Naidis* [2003, (24)]
R20	$O_2^- + O \rightarrow O_3 + e$	1.5×10^{-10}	*Benilov and Naidis* [2003, (25)]
R21	$O_2^- + N_2(A) \rightarrow O_2 + N_2 + e$	2.1×10^{-9}	*Kossyi et al.* [1992, (60)]
R22	$O_2^- + O_2(a) \rightarrow O_2 + O_2 + e$	2×10^{-10}	*Kossyi et al.* [1992, (58)]
R23	$O_2^- + O_2 \rightarrow O_2 + O_2 + e$	$2\times10^{-10}\exp(-6034/T_{R23}^{\text{eff}})$ $\times\frac{1-\exp[-6034(1/T-1/T_{R23}^{\text{eff}})]}{1-\exp[-1509(1/T-1/T_{R23}^{\text{eff}})]}$	*Benilov and Naidis* [2003, (21)]
R24	$O_3^- + O \rightarrow O_2 + O_2 + e$	3×10^{-10}	*Benilov and Naidis* [2003, (26)]
		Electron-impact excitation of metastable states	
R25	$N_2 + e \rightarrow N_2(A) + e$	$k(E/N)F$	*Aleksandrov et al.* [1995, (4)]
R26	$N_2 + e \rightarrow N_2(B) + e$	$k(E/N)F$	*Aleksandrov et al.* [1995, (5)]
R27	$N_2 + e \rightarrow N_2(a') + e$	$k(E/N)F$	*Aleksandrov et al.* [1995, (6)]
R28	$N_2 + e \rightarrow N_2(C) + e$	$k(E/N)F$	*Aleksandrov et al.* [1995, (7)]
R29	$O_2 + e \rightarrow O_2(a) + e$	$k(E/N)F$	*Aleksandrov et al.* [1995, (8)]
		Electron-impact dissociation	
R30	$N_2 + e \rightarrow N + N(^2D) + e$	$5.0\times10^{-9}\exp(-646/(E/N))F$	*Benilov and Naidis* [2003, (5)]
R31	$O_2 + e \rightarrow O + O + e$	$k(E/N)F$	*Aleksandrov et al.* [1995, (10)]
R32	$O_2 + e \rightarrow O + O(^1D) + e$	$k(E/N)F$	*Aleksandrov et al.* [1995, (11)]
		Radiative deactivation of metastables	
R33	$N_2(B) \rightarrow N_2(A) + h\nu\,(1PN_2)$	1.7×10^5	*Liu and Pasko* [2004]
R34	$N_2(C) \rightarrow N_2(B) + h\nu\,(2PN_2)$	2.0×10^7	*Liu and Pasko* [2004]
		Collisional quenching of metastables	
R35	$N_2(A) + O_2 \rightarrow N_2 + O + O$	2.54×10^{-12}	*Kossyi et al.* [1992, (100)]
R36	$N_2(A) + O_2 \rightarrow N_2 + O_2(b,v)$	7.5×10^{-13}	*Popov* [2011, (R2)]
R37	$N_2(A) + O \rightarrow N_2 + O(^1S)$	3×10^{-11}	*Popov* [2011, (R5)]
R38	$N_2(A) + O \rightarrow NO + N(^2D)$	7×10^{-12}	*Kossyi et al.* [1992, (102)]
R39	$N_2(A) + N_2(A) \rightarrow N_2(B) + N_2$	7.7×10^{-11}	*Popov* [2001, (3)]
R40	$N_2(A) + N_2(A) \rightarrow N_2(C) + N_2$	1.6×10^{-10}	*Popov* [2001, (4)]
R41	$N_2(B) + O_2 \rightarrow N_2 + O + O$	3×10^{-10}	*Kossyi et al.* [1992, (113)]
R42	$N_2(B) + N_2 \rightarrow N_2(A) + N_2$	10^{-11}	*Popov* [2001, (8)]
R43	$N_2(a') + O_2 \rightarrow N_2 + O + O(^1D)$	2.8×10^{-11}	*Popov* [2001, (9)]
R44	$N_2(a') + N_2 \rightarrow N_2(B) + N_2$	2×10^{-13}	*Popov* [2001, (10)]
R45	$N_2(C) + O_2 \rightarrow N_2 + O + O(^1D)$	2.5×10^{-10}	*Popov* [2011, (R10)]
R46	$N_2(C) + N_2 \rightarrow N_2(B) + N_2$	10^{-11}	*Popov* [2011, (R11)]
R47	$N_2(C) + N_2 \rightarrow N_2(a') + N_2$	10^{-11}	*Kossyi et al.* [1992, (118)]
R48	$O(^1D) + N_2 \rightarrow O + N_2$	$1.8\times10^{-11}\exp(107/T)$	*Kossyi et al.* [1992, (144)]
R49	$O(^1D) + O_2 \rightarrow O + O_2(b,v)$	$2.56\times10^{-11}\exp(67/T)$	*Kossyi et al.* [1992, (145)]
R50	$O(^1D) + O_2 \rightarrow O + O_2$	$0.64\times10^{-11}\exp(67/T)$	*Kossyi et al.* [1992, (146)]
R51	$O(^1S) + O \rightarrow O(^1D) + O(^1D)$	$5\times10^{-11}\exp(-301/T)$	*Kossyi et al.* [1992, (164)]
R52	$O(^1S) + O_2 \rightarrow O(^1D) + O_2$	$1.3\times10^{-12}\exp(-850/T)$	*Kossyi et al.* [1992, (154)]
R53	$N(^2D) + O_2 \rightarrow NO + O$	$1.5\times10^{-12}(T/300)^{0.5}$	*Kossyi et al.* [1992, (135)]
R54	$N(^2D) + O_2 \rightarrow NO + O(^1D)$	$6\times10^{-12}(T/300)^{0.5}$	*Kossyi et al.* [1992, (136)]

Table A1. (continued)

	Reactions	Rate Constant (1/s, cm^3/s or cm^6/s)	Reference
R55	$N(^2D) + N_2 \rightarrow N + N_2$	6×10^{-15}	*Kossyi et al.* [1992, (139)]
R56	$O_2(a) + O_2 \rightarrow O_2 + O_2$	$2.2 \times 10^{-18} (T/300)^{0.8}$	*Kossyi et al.* [1992, (123)]
R57	$O_2(b,v) + O_2 \rightarrow O_2(b) + O_2(v)$	1.7×10^{-12}	*Kalogerakis et al.* [2002]
	Thermal dissociation and recombination		
R58	$N_2 + M \rightarrow N + N + M$	$Z(T, T_V)[1.1 \times 10^{-7}(X_O + X_N)$ $+ 5 \times 10^{-8}(X_{NO} + X_{O_2} + X_{N_2})]$ $\times \exp(-113200/T)[1 - \exp(-3354/T)]$	*Aleksandrov et al.* [1997, (R40)]
R59	$O_2 + M \rightarrow O + O + M$	$[1.3 \times 10^{-7}X_O + 3.7 \times 10^{-8}X_{O_2}$ $+ 9.3 \times 10^{-9}(X_N + X_{NO} + X_{N_2})]$ $\times \exp(-59380/T)[1 - \exp(-2240/T)]$	*Aleksandrov et al.* [1997, (R41)]
R60	$NO + M \rightarrow N + O + M$	$[1.7 \times 10^{-7}(X_O + X_N + X_{NO})$ $+ 8.7 \times 10^{-9}(X_{O_2} + X_{N_2})]$ $\times \exp(-76000/T)$	*Aleksandrov et al.* [1997, (R42)]
R61	$N + N + M \rightarrow N_2 + M$	$8.27 \times 10^{-34} \exp(500/T)$	*Aleksandrov et al.* [1997, (R43)]
R62	$O + O + M \rightarrow O_2 + M$	$2.76 \times 10^{-34}(X_N + X_{NO} + X_{N_2})\exp(720/T)$ $+ (8.8 \times 10^{-31}X_O + 2.45 \times 10^{-31}X_{O_2})T^{-0.63}$	*Aleksandrov et al.* [1997, (R44)]
R63	$N + O + M \rightarrow NO + M$	$1.76 \times 10^{-31} T^{-0.5}$	*Aleksandrov et al.* [1997, (R45)]
	Exchange of chemical bonds		
R64	$O + N_2 \rightarrow N + NO$	$1.3 \times 10^{-10} \exp(-38000/T)$	*Aleksandrov et al.* [1997, (R47)]
R65	$N + O_2 \rightarrow O + NO$	$10^{-14} T \exp(-3150/T)$	*Aleksandrov et al.* [1997, (R48)]
R66	$N + NO \rightarrow O + N_2$	$10^{-12} T^{0.5}$	*Aleksandrov et al.* [1997, (R46)]
R67	$O + NO \rightarrow N + O_2$	$2.5 \times 10^{-15} T \exp(-19500/T)$	*Aleksandrov et al.* [1997, (R49)]
	Positive ion conversion		
R68	$O_4^+ + O_2(a) \rightarrow O_2^+ + O_2 + O_2$	10^{-10}	*Kossyi et al.* [1992, (228)]
R69	$O_4^+ + O \rightarrow O_2^+ + O_3$	3×10^{-10}	*Kossyi et al.* [1992, (229)]
R70	$O_2^+ + O_2 + O_2 \rightarrow O_4^+ + O_2$	$2.4 \times 10^{-30}(300/T_{R70}^{\text{eff}})^{3.2}$	*Kossyi et al.* [1992, (167)]
R71	$O_2^+N_2 + O_2 \rightarrow O_4^+ + N_2$	10^{-9}	*Kossyi et al.* [1992, (232)]
R72	$O_2^+ + N_2 + N_2 \rightarrow O_2^+N_2 + N_2$	$0.9 \times 10^{-30}(300/T_{R72}^{\text{eff}})^2$	*Kossyi et al.* [1992, (168)]
R73	$O_4^+ + N_2 \rightarrow O_2^+N_2 + O_2$	$4.61 \times 10^{-12}(300/T_{R73}^{\text{eff}})^{2.5} \exp(-2650/T_{R73}^{\text{eff}})$	*Kossyi et al.* [1992, (226)]
R74	$O_2^+N_2 + N_2 \rightarrow O_2^+ + N_2 + N_2$	$1.1 \times 10^{-6}(300/T_{R74}^{\text{eff}})^{5.3} \exp(-2357/T_{R74}^{\text{eff}})$	*Kossyi et al.* [1992, (231)]
R75	$O_4^+ + O_2 \rightarrow O_2^+ + O_2 + O_2$	$3.3 \times 10^{-6}(300/T_{R75}^{\text{eff}})^4 \exp(-5030/T_{R75}^{\text{eff}})$	*Kossyi et al.* [1992, (227)]
R76	$O_2^+ + N_2 \rightarrow NO^+ + NO$	10^{-17}	*Kossyi et al.* [1992, (206)]
R77	$O_2^+ + N \rightarrow NO^+ + O$	1.2×10^{-10}	*Kossyi et al.* [1992, (207)]
R78	$O_2^+ + NO \rightarrow NO^+ + O_2$	4.4×10^{-10}	*Kossyi et al.* [1992, (208)]
R79	$O_4^+ + NO \rightarrow NO^+ + O_2 + O_2$	10^{-10}	*Kossyi et al.* [1992, (230)]
	Negative ion conversion		
R80	$O^- + O_2(a) \rightarrow O_2^- + O$	10^{-10}	*Kossyi et al.* [1992, (242)]
R81	$O_2^- + O \rightarrow O_2 + O^-$	3.3×10^{-10}	*Kossyi et al.* [1992, (237)]
R82	$O_3^- + O \rightarrow O_2^- + O_2$	3.2×10^{-10}	*Kossyi et al.* [1992, (247)]
R83	$O^- + O_2 + M \rightarrow O_3^- + M$	$1.08 \times 10^{-30}(300/T_{R83}^{\text{eff}})$	*Benilov and Naidis* [2003, (27)]
	Two-body ion-ion recombination $(A^- + B^+ \rightarrow A + B)$		
R84	$O^- + O_2^+ \rightarrow O + O_2$		
R85	$O_2^- + O_2^+ \rightarrow O_2 + O_2$		
R86	$O_3^- + O_2^+ \rightarrow O_3 + O_2$	$2 \times 10^{-7}(300/T_i)^{0.5}$	1992 [1992, (I)]
R87	$O^- + NO^+ \rightarrow O + NO$		
R88	$O_2^- + NO^+ \rightarrow O_2 + NO$		
R89	$O_3^- + NO^+ \rightarrow O_3 + NO$		
	Two-body ion-ion recombination $(A^- + BC^+ \rightarrow A + B + C)$		
R90	$O^- + O_2^+ \rightarrow O + O + O$		
R91	$O^- + NO^+ \rightarrow O + N + O$		
R92	$O^- + O_4^+ \rightarrow O + O_2 + O_2$		
R93	$O^- + O_2^+N_2 \rightarrow O + O_2 + N_2$		
R94	$O_2^- + O_2^+ \rightarrow O_2 + O + O$		
R95	$O_2^- + NO^+ \rightarrow O_2 + N + O$	10^{-7}	*Kossyi et al.* [1992, (II)]
R96	$O_2^- + O_4^+ \rightarrow O_2 + O_2 + O_2$		
R97	$O_2^- + O_2^+N_2 \rightarrow O_2 + O_2 + N_2$		
R98	$O_3^- + O_2^+ \rightarrow O_3 + O + O$		
R99	$O_3^- + NO^+ \rightarrow O_3 + N + O$		
R100	$O_3^- + O_4^+ \rightarrow O_3 + O_2 + O_2$		
R101	$O_3^- + O_2^+N_2 \rightarrow O_3 + O_2 + N_2$		
	Three-body ion-ion recombination		
R102	$O^- + O_2^+ + M \rightarrow O + O_2 + M$		
R103	$O_2^- + O_2^+ + M \rightarrow O_2 + O_2 + M$		
R104	$O^- + NO^+ + M \rightarrow O + NO + M$	$2 \times 10^{-25}(X_{N_2} + X_{O_2})(300/T_i)^{2.5}$	*Kossyi et al.* [1992, (V)]
R105	$O_2^- + NO^+ + M \rightarrow O_2 + NO + M$		
R106	$O_2^- + O_4^+ + M \rightarrow O_2 + O_2 + O_2 + M$		*Pancheshnyi et al.* [2005, (18)]

Appendix A: List of Chemical Reactions

[76] Table A1 contains a list of the chemical reactions used in this work. Rate coefficients are functions of E, N, T, and T_V. The F factor depends on T_V according to equation (11). The effective electron temperature is written as a function of E/N [*Vidal et al.*, 2002, equation (4)]:

$$T_e = T + a_e(E/N)^{0.46}, \tag{A1}$$

where $a_e = 3648.6$ K/Td$^{0.46}$. The simple analytical expression above deviates from the Einstein relation $T_e = q_e D_e / k_B \mu_e$ by less than 40% in the range of electric fields between 1 and 35 kV/cm (at ground level pressure and room temperature), where q_e is the electronic charge, k_B the Boltzmann constant, and D_e and μ_e are the electron diffusion coefficient and mobility, respectively, calculated using BOLSIG+ [*Hagelaar and Pitchford*, 2005] for the same conditions as in Figure 3. The ion temperature is calculated as [*Benilov and Naidis*, 2003, reaction (28)]:

$$T_i = T + a_i(E/N)^2, \tag{A2}$$

where $a_i = 0.13$ K/Td^2. The effective temperature of ions colliding with neutrals is defined as [*Mnatsakanyan and Naidis*, 1991, equation (28)]:

$$T_{Rj}^{\text{eff}} = \frac{m_i T + m_j T_i}{m_i + m_j}, \tag{A3}$$

where m_i and m_j are the masses of the ion and neutral components involved in the reaction, respectively. In reactions containing a generic component "M", the rate coefficient depends on the number fraction of M, i.e., $X_M = n_M/N$ (where $0 < X_M \leq 1$). Rate coefficients are presented in units of 1/s, cm^3/s, and cm^6/s for one-, two-, and three-body reactions, respectively. Reduced electric field E/N is expressed in Townsend and temperatures in Kelvin. Reference for each rate coefficient is provided in Table A1, including the reaction/equation number in the corresponding original work.

References

Aleksandrov, N. L., E. M. Bazelyan, I. V. Kochetov, and N. A. Dyatko (1997), The ionization kinetics and electric field in the leader channel in long air gaps, *J. Phys. D Appl. Phys.*, *30*, 1616–1624, doi:10.1088/0022-3727/30/11/011.

Aleksandrov, N. L., E. M. Bazelyan, N. A. Dyatko, and I. V. Kochetov (1998), Streamer breakdown of long air gaps, *Plasma Phys. Rep.*, *24*, 541–555.

Aleksandrov, N. L., E. M. Bazelyan, and A. M. Konchakov (2001a), Plasma parameters in the channel of a long leader in air, *Plasma Phys. Rep.*, *27*, 875–885, doi:10.1134/1.1409721.

Aleksandrov, N. L., E. M. Bazelyan, R. B. Carpenter, M. M. Drabkin, and Y. P. Raizer (2001b), The effect of coronae on leader initiation and development under thunderstorm conditions and in long air gaps, *J. Phys. D Appl. Phys.*, *34*(22), 3256–3266, doi:10.1088/0022-3727/34/22/309.

Aleksandrov, N. L., A. E. Bazelyan, and I. V. Kochetov (1995), Modeling of long streamers in atmospheric-pressure air, *Plasma Phys. Rep.*, *21*(1), 57–75.

Aleksandrov, N. L., S. V. Kindysheva, M. N. Nudnova, and A. Y. Starikovskiy (2010), Mechanism of ultra-fast heating in a non-equilibrium weakly ionized air discharge plasma in high electric fields, *J. Phys. D Appl. Phys.*, *43*, 255201, 1–19, doi:10.1088/0022-3727/43/25/255201.

Andreev, A. G., E. M. Bazelyan, M. U. Bulatov, I. P. Kuzhekin, L. M. Makalsky, D. I. Sukharevskij, and V. S. Syssoev (2008), Experimental study of the positive leader velocity as a function of the current in the initial and final-jump phases of a spark discharge, *Plasma Phys. Rep.*, *34*(7), 609–615, doi:10.1134/S1063780X0807009X.

Bastien, F., and E. Marode (1985), Breakdown simulation of electronegative gases in non-uniform field, *J. Phys. D Appl. Phys.*, *18*, 377–393, doi:10.1088/0022-3727/18/3/007.

Bazelyan, E. M., and Y. P. Raizer (1998), *Spark Discharge*, CRC Press, Boca Raton, Fla.

Bazelyan, E. M., and Y. P. Raizer (2000), *Lightning Physics and Lightning Protection*, Institute of Physics Publishing, Bristol, Philadelphia.

Bazelyan, E. M., Y. P. Raizer, and N. L. Aleksandrov (2007a), The effect of reduced air density on streamer-to-leader transition and on properties of long positive leader, *J. Phys. D Appl. Phys.*, *40*(14), 4133–4144, doi:10.1088/0022-3727/40/14/007.

Bazelyan, E. M., N. L. Aleksandrov, Y. P. Raizer, and A. M. Konchakov (2007b), The effect of air density on atmospheric electric fields required for lightning initiation from a long airborne object, *Atmos. Res.*, *86*(2), 126–138, doi:10.1016/j.atmosres.2007.04.001.

Bazelyan, E. M., Y. P. Raizer, and N. L. Aleksandrov (2008), Corona initiated from grounded objects under thunderstorm conditions and its influence on lightning attachment, *Plasma Sources Sci. Technol.*, *17*, 024015, 1–17, doi:10.1088/0963-0252/17/2/024015.

Becerra, M., and V. Cooray (2006), A simplified physical model to determine the lightning upward connecting leader inception, *IEEE Trans. Power Deliv.*, *21*(2), 897–908, doi:10.1109/TPWRD.2005.859290.

Becerra, M., V. Cooray, S. Soula, and S. Chauzy (2007), Effect of the space charge layer created by corona at ground level on the inception of upward lightning leaders from tall towers, *J. Geophys. Res.*, *112*, D12205, doi:10.1029/2006JD008308.

Benilov, M. S., and G. V. Naidis (2003), Modelling of low-current discharges in atmospheric-pressure air taking account of non-equilibrium effects, *J. Phys. D Appl. Phys.*, *36*, 1834–1841, doi:10.1088/0022-3727/36/15/314.

Biagi, C. J., D. M. Jordan, M. A. Uman, J. D. Hill, W. H. Beasley, and J. Howard (2009), High-speed video observations of rocket-and-wire initiated lightning, *Geophys. Res. Lett.*, *36*, L15801, doi:10.1029/2009GL038525.

Biagi, C. J., M. A. Uman, J. D. Hill, D. M. Jordan, V. A. Rakov, and J. Dwyer (2010), Observations of stepping mechanisms in a rocket-and-wire triggered lightning flash, *J. Geophys. Res.*, *115*, D23215, doi:10.1029/2010JD014616.

Biberman, L. M., V. S. Vorob'ev, and I. T. Yakubov (1987), *Kinetics of Nonequilibrium Low-Temperature Plasmas*, Plenum, New York.

Bondiou, A., and I. Gallimberti (1994), Theoretical modelling of the development of the positive spark in long air gaps, *J. Phys. D Appl. Phys.*, *27*(6), 1252–1266, doi:10.1088/0022-3727/27/6/024.

Boris, J. P., and D. L. Book (1973), Flux-corrected transport. 1. SHASTA, a fluid transport algorithm that works, *J. Comput. Phys.*, *11*(1), 38–69, doi:10.1016/0021-9991(73)90147-2.

Boulos, M. I., P. Fauchais, and E. Pfender (1994), *Thermal Plasmas, Fundamentals and Applications*, vol. 1, Plenum, New York.

Brasseur, G. P., J. F. Muller, and C. Granier (1996), Atmospheric impact of NO$_x$ emissions by subsonic aircraft: A three-dimensional model study, *J. Geophys. Res.*, *101*(D1), 1423–1428, doi:10.1029/95JD02363.

Briels, T. M. P., J. Kos, E. M. van Veldhuizen, and U. Ebert (2006), Circuit dependence of the diameter of pulsed positive streamers in air, *J. Phys. D Appl. Phys.*, *39*(24), 5201–5210, doi:10.1088/0022-3727/39/24/016.

Briels, T. M. P., J. Kos, G. J. J. Winands, E. M. van Veldhuizen, and U. Ebert (2008), Positive and negative streamers in ambient air: Measuring diameter, velocity and dissipated energy, *J. Phys. D Appl. Phys.*, *41*, 234004, 1–11, doi:10.1088/0022-3727/41/23/234004.

Capitelli, M., C. M. Ferreira, B. F. Gordiets, and A. I. Osipov (2000), *Plasma Kinetics in Atmospheric Gases*, Springer, New York.

Černák, M., E. M. van Veldhuizen, I. Morva, and W. R. Rutgers (1995), Effect of cathode surface properties on glow-to-arc transition in a short positive corona gap in ambient air, *J. Phys. D Appl. Phys.*, *28*, 1126–1132, doi:10.1088/0022-3727/28/6/015.

Chen, A. B., et al. (2008), Global distributions and occurrence rates of transient luminous events, *J. Geophys. Res.*, *113*, A08306, doi:10.1029/2008JA013101.

Chen, X., and H. P. Li (2003), The reactive thermal conductivity for a two-temperature plasma, *Int. J. Heat Mass Transfer*, *46*(8), 1443–1454, doi:10.1016/S0017-9310(02)00414-3.

Chernyi, G. G., S. A. Losev, S. O. Macheret, and B. V. Potapkin (2004), *Physical and Chemical Processes in Gas Dynamics: Physical and Chemical Kinetics and Thermodynamics of Gases and Plasmas,* vol. 197, 328 pp., American Institute of Aeronautics and Astronautics, Reston, Va.

Chou, J. K., et al. (2010), Gigantic jets with negative and positive polarity streamers, *J. Geophys. Res.*, *115*, A00E45, doi:10.1029/2009JA014831.

Chou, J. K., L. Y. Tsai, C. L. Kuo, Y. J. Lee, C. M. Chen, A. B. Chen, H. T. Su, R. R. Hsu, P. L. Chang, and L. C. Lee (2011), Optical emissions and behaviors of the blue starters, blue jets, and gigantic jets observed in the Taiwan transient luminous event ground campaign, *J. Geophys. Res.*, *116*, A07301, doi:10.1029/2010JA016162.

Cummer, S. A., J. Li, F. Han, G. Lu, N. Jaugey, W. A. Lyons, and T. E. Nelson (2009), Quantification of the troposphere-to-ionosphere charge transfer in a gigantic jet, *Nat. Geosci.*, *2*(9), 617–620, doi:10.1038/ngeo607.

da Silva, C. L., and V. P. Pasko (2012), Simulation of leader speeds at gigantic jet altitudes, *Geophys. Res. Lett.*, *39*, L13805, doi:10.1029/2012GL052251.

da Silva, C. L., and V. P. Pasko (2013), Vertical structuring of gigantic jets, *Geophys. Res. Lett.*, *40*, 3315–3319, doi:10.1002/grl.50596.

D'Angola, A., G. Colonna, C. Gorse, and M. Capitelli (2008), Thermodynamic and transport properties in equilibrium air plasmas in a wide pressure and temperature range, *Eur. Phys. J. D*, *46*(1), 129–150, doi:10.1140/epjd/e2007-00305-4.

Flitti, A., and S. Pancheshnyi (2009), Gas heating in fast pulsed discharges in N_2–O_2 mixtures, *Eur. Phys. J. Appl. Phys.*, *45*(2), 21001, 1–7, doi:10.1051/epjap/2009011.

Fridman, A., and L. A. Kennedy (2004), *Plasma Physics and Engineering*, 853 pp., Taylor and Francis, New York.

Gallimberti, I. (1979), The mechanism of the long spark formation, *J. Phys. Coll.*, *40*(C7), 193–250.

Gallimberti, I., G. Bacchiega, A. Bondiou-Clergerie, and P. Lalande (2002), Fundamental processes in long air gap discharges, *C. R. Phys.*, *3*, 1335–1359, doi:10.1016/S1631-0705(02)01414-7.

Goelian, N., P. Lalande, A. Bondiou-Clergerie, G. L. Bacchiega, A. Gazzani, and I. Gallimberti (1997), A simplified model for the simulation of positive-spark development in long air gaps, *J. Phys. D Appl. Phys.*, *30*(17), 2441–2452, doi:10.1088/0022-3727/30/17/010.

Gorin, B. N., V. I. Levitov, and A. V. Shkilev (1976), Some principles of leader discharge of air gaps with strong non-uniform field, *IEE Conf. Publ.*, *143*, 274–278.

Hagelaar, G. J. M., and L. C. Pitchford (2005), Solving the Boltzmann equation to obtain electron transport coefficients and rate coefficients for fluid models, *Plasma Sources Sci. Technol.*, *14*(4), 722–733, doi:10.1088/0963-0252/14/4/011.

Hill, J. D., M. A. Uman, and D. M. Jordan (2011), High-speed video observations of a lightning stepped leader, *J. Geophys. Res.*, *116*, D16117, doi:10.1029/2011JD015818.

Hirschfelder, J. O., C. F. Curtiss, and R. B. Bird (1964), *Molecular Theory of Gases and Liquids*, John Wiley & Sons, Inc., New York.

Hoffman, J. D. (2001), *Numerical Methods for Engineers and Scientists*, 2nd ed., McGraw-Hill, Inc., New York.

Jaeger, E. F., L. Oster, and A. V. Phelps (1976), Growth of thermal constrictions in a weakly ionized gas discharge in helium, *Phys. Fluids*, *19*(6), 819–830, doi:10.1063/1.861548.

Kalogerakis, K. S., R. A. Copeland, and T. G. Slanger (2002), Collisional removal of $O_2(b^1\Sigma_g^+, v = 2, 3)$, *J. Chem. Phys.*, *116*(12), 4877–4885, doi:10.1063/1.1456026.

Kasemir, H. W. (1960), A contribution to the electrostatic theory of a lightning discharge, *J. Geophys. Res.*, *65*(7), 1873–1878.

Kossyi, I. A., A. Y. Kostinsky, A. A. Matveyev, and V. P. Silakov (1992), Kinetic scheme of the non-equilibrium discharge in nitrogen-oxygen mixtures, *Plasma Sources Sci. Technol.*, *1*, 207–220, doi:10.1088/0963-0252/1/3/011.

Krehbiel, P. R., J. A. Riousset, V. P. Pasko, R. J. Thomas, W. Rison, M. A. Stanley, and H. E. Edens (2008), Upward electrical discharges from thunderstorms, *Nat. Geosci.*, *1*, 233–237, doi:10.1038/ngeo162.

Krivonosova, O. E., S. A. Losev, V. P. Nalivaiko, Y. K. Mukoseev, and O. P. Shatalov (1991), Recommended data on the rate constants of chemical reactions among molecules consisting of N and O atoms, in *Reviews of Plasma Chemistry,* vol. 1, edited by B. M. Smirnov, Consult. Bur., New York.

Kuo, C.-L., et al. (2009), Discharge processes, electric field, and electron energy in ISUAL-recorded gigantic jets, *J. Geophys. Res.*, *114*, A04314, doi:10.1029/2008JA013791.

Lalande, P., A. Bondiou-Clergerie, G. Bacchiega, and I. Gallimberti (2002), Observations and modeling of lightning leaders, *C. R. Phys.*, *3*, 1375–1392, doi:10.1016/S1631-0705(02)01413-5.

Larsson, A. (1998), The effect of a large series resistance on the streamer-to-spark transition in dry air, *J. Phys. D Appl. Phys.*, *31*, 1100–1108, doi:10.1088/0022-3727/31/9/011.

Laurendeau, N. M. (2005), *Statistical Thermodynamics: Fundamentals and Applications*, Cambridge Univ. Press, Cambridge, U. K.

Lawton, S. A., and A. V. Phelps (1978), Excitation of the $b^1\Sigma_g^+$ state of O_2 by low energy electrons, *J. Chem. Phys.*, *69*(3), 1055–1068, doi:10.1063/1.436700.

Lee, L.-J., S.-M. Huang, J.-K. Chou, C.-L. Kuo, A. B. Chen, H.-T. Su, R.-R. Hsu, H. Frey, Y. Takahashi, and L.-C. Lee (2012), Characteristics and generation of secondary jets and secondary gigantic jets, *J. Geophys. Res.*, *117*, A06317, doi:10.1029/2011JA017443.

Liu, N. (2012), Multiple ion species fluid modeling of sprite halos and the role of electron detachment of O^- in their dynamics, *J. Geophys. Res.*, *117*, A03308, doi:10.1029/2011JA017062.

Liu, N. Y., and V. P. Pasko (2004), Effects of photoionization on propagation and branching of positive and negative streamers in sprites, *J. Geophys. Res.*, *109*, A04301, doi:10.1029/2003JA010064.

Losev, S. A. (1981), *Gasdynamic Laser*, Springer-Verlag, Berlin.

Lu, G., et al. (2011), Lightning development associated with two negative gigantic jets, *Geophys. Res. Lett.*, *38*, L12801, doi:10.1029/2011GL047662.

Luque, A., and F. J. Gordillo-Vázquez (2012), Mesospheric electric breakdown and delayed sprite ignition caused by electron detachment, *Nat. Geosci.*, *5*(1), 22–25, doi:10.1038/ngeo1314.

Marode, E. (1983), The glow-to-arc transition, in *Electrical Breakdown and Discharges in Gases: Macroscopic Discharges,* vol. B, edited by E. E. Kunhardt and L. H. Luessen, pp. 119–166, Plenum Press, New York.

Marode, E., F. Bastien, and M. Bakker (1979), A model of the streamer-induced spark formation based on neutral dynamics, *J. Appl. Phys.*, *50*, 140–146, doi:10.1063/1.325697.

Marrone, P. V., and C. E. Treanor (1963), Chemical relaxation with preferential dissociation from excited vibrational levels, *Phys. Fluids*, *6*(9), 1215–1221, doi:10.1063/1.1706888.

Mazur, V. (2002), Physical processes during development of lightning flashes, *C. R. Phys.*, *3*, 1393–1409.

Mishin, E. (1997), Ozone layer perturbation by a single blue jet, *Geophys. Res. Lett.*, *24*(15), 1919–1922, doi:10.1029/97GL01890.

Mnatsakanyan, A. K., and G. V. Naidis (1985), The vibrational-energy balance in a discharge in air, *High Temp.*, *23*(4), 506–513.

Mnatsakanyan, A. K., and G. V. Naidis (1991), Charged particle production and loss processes in nitrogen–oxygen plasmas, in *Reviews of Plasma Chemistry,* vol. 1, edited by B. M. Smirnov, Consult. Bur., New York.

Morrow, R., and J. J. Lowke (1997), Streamer propagation in air, *J. Phys. D Appl. Phys.*, *30*, 614–627, doi:10.1088/0022-3727/30/4/017.

Naidis, G. V. (1999), Simulation of streamer-to-spark transition in short non-uniform air gaps, *J. Phys. D Appl. Phys.*, *32*(20), 2649–2654, doi:10.1088/0022-3727/32/20/311.

Naidis, G. V. (2005), Dynamics of streamer breakdown of short non-uniform air gaps, *J. Phys. D Appl. Phys.*, *38*(21), 3889–3893, doi:10.1088/0022-3727/38/21/009.

Naidis, G. V. (2007), Simulation of convection-stabilized low-current glow and arc discharges in atmospheric-pressure air, *Plasma Sources Sci. Technol.*, *16*(2), 297–303, doi:10.1088/0963-0252/16/2/012.

Nemchinsky, V. (2005), Dissociation reactive thermal conductivity in a two-temperature plasma, *J. Phys. D Appl. Phys.*, *38*(20), 3825–3831, doi:10.1088/0022-3727/38/20/008.

Neubert, T., and O. Chanrion (2013), On the electric breakdown field of the mesosphere and the influence of electron detachment, *Geophys. Res. Lett.*, *40*, 2373–2377, doi:10.1002/grl.50433.

Neubert, T., O. Chanrion, E. Arnone, F. Zanotti, S. Cummer, J. Li, M. Füllekrug, S. Soula, and O. van der Velde (2011), The properties of a gigantic jet reflected in a simultaneous sprite: Observations interpreted by a model, *J. Geophys. Res.*, *116*, A12329, doi:10.1029/2011JA016928.

Ortega, P., P. Domens, A. Gibert, B. Hutzler, and G. Riquel (1994), Performance of a 16.7 m air rod-plane gap under a negative switching impulse, *J. Phys. D Appl. Phys.*, *27*(11), 2379–2387, doi:10.1088/0022-3727/27/11/019.

Pancheshnyi, S., M. Nudnova, and A. Starikovskii (2005), Development of a cathode-directed streamer discharge in air at different pressures: Experiment and comparison with direct numerical simulation, *Phys. Rev. E*, *71*, 016407, 1–12, doi:10.1103/PhysRevE.71.016407.

Pasko, V. P. (2006), Theoretical modeling of sprites and jets, in *Sprites, Elves and Intense Lightning Discharges (NATO Sci. Series II: Math.,*

Phys. and Chem.), edited by M. Fullekrug, E. A. Mareev, and M. J. Rycroft, pp. 253–311, Springer, Heidelberg.

Pasko, V. P. (2007), Red sprite discharges in the atmosphere at high altitude: The molecular physics and the similarity with laboratory discharges, *Plasma Sources Sci. Technol.*, *16*, S13–S29, doi:10.1088/0963-0252/16/1/S02.

Pasko, V. P., M. A. Stanley, J. D. Mathews, U. S. Inan, and T. G. Wood (2002), Electrical discharge from a thundercloud top to the lower ionosphere, *Nature*, *416*(6877), 152–154, doi:10.1038/416152a.

Petersen, D., M. Bailey, W. H. Beasley, and J. Hallett (2008), A brief review of the problem of lightning initiation and a hypothesis of initial lightning leader formation, *J. Geophys. Res.*, *113*, D17205, doi:10.1029/2007JD009036.

Petrov, N. I., and G. N. Petrova (1999), Physical mechanisms for the development of lightning discharges between a thundercloud and the ionosphere, *Tech. Phys. Lett.*, *44*, 472–475.

Phelps, A. V., and L. C. Pitchford (1985), Anisotropic scattering of electrons by N_2 and its effect on electron transport, *Phys. Rev. A*, *31*(5), 2932–2949, doi:10.1103/PhysRevA.31.2932.

Popov, N. A. (2001), Investigation of the mechanism for rapid heating of nitrogen and air in gas discharges, *Plasma Phys. Rep.*, *27*(10), 886–896, doi:10.1134/1.1409722.

Popov, N. A. (2003), Formation and development of a leader channel in air, *Plasma Phys. Rep.*, *29*(8), 695–708, doi:10.1134/1.1601648.

Popov, N. A. (2009), Study of the formation and propagation of a leader channel in air, *Plasma Phys. Rep.*, *35*, 785–793, doi:10.1134/S1063780X09090074.

Popov, N. A. (2011), Fast gas heating in a nitrogen-oxygen discharge plasma: I. Kinetic mechanism, *J. Phys. D Appl. Phys.*, *44*, 285201, 1–16, doi:10.1088/0022-3727/44/28/285201.

Potter, D. (1973), *Computational Physics*, 304 pp., John Wiley & Sons, Inc., New York.

Qin, J., S. Celestin, and V. P. Pasko (2012), Minimum charge moment change in positive and negative cloud to ground lightning discharges producing sprites, *Geophys. Res. Lett.*, *39*, L22801, doi:10.1029/2012GL053951.

Raizer, Y. P. (1991), *Gas Discharge Physics*, Springer-Verlag, New York.

Raizer, Y. P., M. N. Shneider, and N. A. Yatsenko (1995), *Radio-Frequency Capacitive Discharges*, CRC Press, Boca Raton, Fla.

Raizer, Y. P., G. M. Milikh, and M. N. Shneider (2006), On the mechanism of blue jet formation and propagation, *Geophys. Res. Lett.*, *33*, L23801, doi:10.1029/2006GL027697.

Raizer, Y. P., G. M. Milikh, and M. N. Shneider (2007), Leader-streamers nature of blue jets, *J. Atmos. Sol. Terr. Phys.*, *69*(8), 925–938, doi:10.1016/j.jastp.2007.02.007.

Raizer, Y. P., G. M. Milikh, and M. N. Shneider (2010), Streamer- and leader-like processes in the upper atmosphere: Models of red sprites and blue jets, *J. Geophys. Res.*, *115*, A00E42, doi:10.1029/2009JA014645.

Rakov, V. A., and M. A. Uman (2003), *Lightning: Physics and Effects*, 687 pp., Cambridge Univ. Press, Cambridge, U. K.

Rayment, S. W., and J. L. Moruzzi (1978), Electron detachment studies between O^- ions and nitrogen, *Int. J. Mass Spectrom. Ion Phys.*, *26*(3), 321–326, doi:10.1016/0020-7381(78)80033-3.

Reess, T., P. Ortega, A. Gibert, P. Domens, and P. Pignolet (1995), An experimental study of negative discharge in a 1.3 m point-plane air gap: The function of the space stem in the propagation mechanism, *J. Phys. D Appl. Phys.*, *28*(11), 2306–2313, doi:10.1088/0022-3727/28/11/011.

Riousset, J. A., V. P. Pasko, P. R. Krehbiel, R. J. Thomas, and W. Rison (2007), Three-dimensional fractal modeling of intracloud lightning discharge in a New Mexico thunderstorm and comparison with lightning mapping observations, *J. Geophys. Res.*, *112*, D15203, doi:10.1029/2006JD007621.

Riousset, J. A., V. P. Pasko, P. R. Krehbiel, W. Rison, and M. A. Stanley (2010a), Modeling of thundercloud screening charges: Implications for blue and gigantic jets, *J. Geophys. Res.*, *115*, A00E10, doi:10.1029/2009JA014286.

Riousset, J. A., V. P. Pasko, and A. Bourdon (2010b), Air-density-dependent model for analysis of air heating associated with streamers, leaders, and transient luminous events, *J. Geophys. Res.*, *115*, A12321, doi:10.1029/2010JA015918.

Rogoff, G. L. (1972), Gas heating effects in the constriction of a high-pressure glow discharge column, *Phys. Fluids*, *15*, 1931–1940, doi:10.1063/1.1693805.

Saba, M. M. F., K. L. Cummins, T. A. Warner, E. P. Krider, L. Z. S. Campos, M. G. Ballarotti, O. Pinto Jr., and S. A. Fleenor (2008), Positive leader characteristics from high-speed video observations, *Geophys. Res. Lett.*, *35*, L07802, doi:10.1029/2007GL033000.

Shneider, M. N., M. S. Mokrov, and G. M. Milikh (2012), Dynamic contraction of the positive column of a self-sustained glow discharge in molecular gas, *Phys. Plasmas*, *19*, 033512, 1–4, doi:10.1063/1.3694913.

Smirnov, B. M. (1982), *Negative Ions*, McGraw-Hill Inc., New York.

Soula, S., O. A. van der Velde, J. Montanya, P. Huet, C. Barthe, and J. Bór (2011), Gigantic jets produced by an isolated tropical thunderstorm near Réunion Island, *J. Geophys. Res.*, *116*, D19103, doi:10.1029/2010JD015581.

Sparrow, V. W., and R. Raspet (1991), A numerical method for general finite amplitude wave propagation in two dimensions and its application to spark pulses, *J. Acoust. Soc. Am.*, *90*(5), 2683–2691, doi:10.1121/1.401863.

Su, H. T., R. R. Hsu, A. B. Chen, Y. C. Wang, W. S. Hsiao, W. C. Lai, L. C. Lee, M. Sato, and H. Fukunishi (2003), Gigantic jets between a thundercloud and the ionosphere, *Nature*, *423*, 974–976, doi:10.1038/nature01759.

Treanor, C. E., and P. V. Marrone (1962), Effect of dissociation on the rate of vibrational relaxation, *Phys. Fluids*, *5*(9), 1022–1026, doi:10.1063/1.1724467.

Treanor, C. E., J. W. Rich, and R. G. Rehm (1968), Vibrational relaxation of anharmonic oscillators with exchange-dominated collisions, *J. Chem. Phys.*, *48*(4), 1798–1807, doi:10.1063/1.1668914.

Vallance Jones, A. V. (1974), *Aurora*, D. Reidel, Norwell, Mass.

van der Velde, O., J. Bór, J. Li, S. A. Cummer, E. Arnone, F. Zanotti, M. Fullekrug, C. Haldoupis, S. NaitAmor, and T. Farges (2010), Multi-instrumental observations of a positive gigantic jet produced by a winter thunderstorm in Europe, *J. Geophys. Res.*, *115*, D24301, doi:10.1029/2010JD014442.

van der Velde, O. A., W. A. Lyons, T. E. Nelson, S. A. Cummer, J. Li, and J. Bunnell (2007), Analysis of the first gigantic jet recorded over continental North America, *J. Geophys. Res.*, *112*, D20104, doi:10.1029/2007JD008575.

Vidal, F., I. Gallimberti, F. A. M. Rizk, T. W. Johnston, A. Bondiou-Clergerie, D. Comtois, J.-C. Kieffer, B. L. Fontaine, H. P. Mercure, and H. Pépin (2002), Modeling of the air plasma near the tip of the positive leader, *IEEE Trans. Plasma Sci.*, *30*(3), 1339–1349, doi:10.1009/TPS.2002.801538.

Wescott, E. M., D. D. Sentman, D. L. Osborne, D. L. Hampton, and M. J. Heavner (1995), Preliminary results from the Sprites94 aircraft campaign: 2. Blue jets, *Geophys. Res. Lett.*, *22*(10), 1209–1212, doi:10.1029/95GL00582.

Wescott, E. M., D. D. Sentman, M. J. Heavner, D. L. Hampton, D. L. Osborne, and O. H. Vaughan (1996), Blue starters: Brief upward discharges from an intense Arkansas thunderstorm, *Geophys. Res. Lett.*, *23*(16), 2153–2156, doi:10.1029/96GL01969.

Zalesak, S. T. (1979), Fully multidimensional flux-corrected transport algorithms for fluids, *J. Comput. Phys.*, *31*(3), 335–362, doi:10.1016/0021-9991(79)90051-2.